NTNU
Norwegian University of
Science and Technology

The Effect of Deformation on Intergranular Corrosion of AlMgSi Alloys

Julie Grønvold

Chemical Engineering and Biotechnology
Submission date: June 2017
Supervisor: Trond Furu, IMA
Co-supervisor: Otto Lunder, IMA

Norwegian University of Science and Technology
Department of Materials Science and Engineering

Preface

The present master thesis entitled ”The Effect of Deformation on Intergranular Corrosion of AlMgSi Alloys” is written during spring 2017 at Department of Materials Science and Engineering, Norwegian University of Science and Technology (NTNU). The work finalizes the 5-year Master's degree program Chemical Engineering and Biotechnology, and is a continuation of the specialization project on the same topic, conducted by the author at the department during fall 2016. Furthermore, the master thesis is a collaboration project between NTNU and Hydro. All work has been carried out by the author, except TEM studies which were conducted with assistance from Sigurd Wenner from SINTEF.

Trondheim, June 2017
Julie Grønvold

Acknowledgement

Acknowledgements are directed towards my supervisor Trond Furu[1] and co-supervisor Otto Lunder[2] for greatly appreciated guidance and expertise throughout this and previous semester, and for being available whenever I have needed advice.

Special thanks go to Trygve Lindahl Schanche[3] and Birgitte Karlsen[2] for instructions on sample preparation for examinations in light microscope and electron microscope. My greatest gratitude is also directed towards Pål Christian Skaret[3] for helping me with rolling and stretching of samples on short notice. Your guidance and help have been very important for this work.

Finally, I would like to thank Yingda Yu[3] for his good help and advice on studies in SEM and TEM, and Sigurd Wenner[2] for highly valuable assistance on TEM, HAADF-STEM imaging and EDS mapping. Thanks to all of you for making it possible for me to work on this exciting project.

[1] Hydro Aluminium, Sunndalsøra
[2] SINTEF, Materials and Chemistry, Trondheim
[3] Department of Materials Science and Engineering, NTNU, Trondheim

Abstract

The heat treatable AlMgSi alloys are regarded as medium strength materials with excellent corrosion properties. To achieve enhanced mechanical properties with the aim to expand the application areas, Cu may be added since this causes a refinement in precipitate dispersion and thereby increases strength, hardness and ductility. However, AlMgSi(Cu) alloys become sensitized to intergranular corrosion (IGC) during thermomechanical treatment, presumably due to precipitation of a continuous, Cu rich film along the grain boundaries which has been detected in several studies. Microgalvanic effects arise between the cathodic film and an adjacent, anodic, precipitate free zone. Cold deformation has been suggested as a measure to improve the IGC resistance of AlMgSi alloys, considering that deformation introduces dislocations, alters the microstructure in favorable ways and may change the precipitation process during ageing. The latter is of highly importance as the precipitates give rise to IGC. The objective of this work was to assess the effect of cold deformation on IGC susceptibility of AlMgSi alloys and obtain a better understanding of the corrosion mechanism in deformed materials.

Four different AlMgSi alloys, 6005.40, C28, 6016 A and 6016 B, were subjected to deformation by rolling or stretching either before or after final ageing treatment, that is either pre- or post-deformation. All alloys were aged to T6 temper, and a set of 6016 samples was also aged to simulate the paint bake cycle in the automotive industry. Vickers hardness measurements were conducted to evaluate the effect of deformation on hardness. Moreover, accelerated IGC testing according to ISO 11846 (method B) was performed on differently deformed and aged samples. Subsequently, the corroded microstructure of all samples was examined in light microscope to evaluate IGC resistance, and additionally, the uncorroded microstructure of 6005.40 was studied in scanning and transmission electron microscope to assess the effect of deformation on alloy microstructure and precipitate structure.

Results revealed that pre-deformation subsequent to solution heat treatment significantly improved IGC resistance, especially in Cu containing alloys, while maintaining good mechanical properties. It was shown by detailed precipitate examinations in transmission electron microscope that more Cu is incorporated into precipitates in pre-deformed materials compared to in undeformed materials. It is believed that this reduces the amount of Cu available for formation of the Cu rich film on the grain boundaries, thereby reducing IGC susceptibility. A transition to pitting-like corrosion was observed in the pre-deformed alloys. Pre-deformation after pre-baking of alloys for automotive applications proved to be detrimental for corrosion properties. However, it is believed that pre-deformation prior to pre-baking may be advantageous for achieving optimum paint bake response combined with good corrosion properties. The effect of post-deformation on mechanical and corrosion properties was ambiguous. Post-rolling somewhat improved the IGC resistance but did not increase the hardness, whereas post-stretching did not improve the IGC resistance but increased the hardness of the alloys. Further examinations are required to obtain knowledge of the corrosion mechanism in post-deformed materials.

Sammendrag

Utherdbare AlMgSi-legeringer regnes for å ha moderat styrke og eksepsjonelt gode korrosjonsegenskaper. Cu kan tilsettes for å forbedre de mekaniske egenskapene til legeringene med mål om å utvide bruksområdene, da Cu fører til en forfining av presipitatfordelingen og dermed bidrar til økt styrke, hardhet og duktilitet. AlMgSi(Cu)-legeringer kan imidlertid bli sensitive for intergranulær korrosjon (IGC) under varmebehandling, noe som antagelig skyldes presipitering av en kontinuerlig, Cu-holdig film langs korngrensene, hvilket har blitt påvist i flere studier. Mikrogalvaniske effekter oppstår mellom den katodiske filmen på korngrensene og den nærliggende, anodiske, presipitatfrie sonen. Kald deformasjon har blitt foreslått som et tiltak for å forbedre IGC-motstanden til AlMgSi-legeringer, tatt i betraktning at deformasjon introduserer dislokasjoner, fordelaktig endrer mikrostrukturen og kan endre presipiteringsprosessen under utherding. Sistnevnte er spesielt viktig da det er presipitatene som gir opphav til IGC. Hensikten med dette arbeidet var å vurdere effekten av deformasjon på AlMgSi-legeringers følsomheten for IGC og oppnå en bedre forståelse av korrosjonsmekanismen i deformerte materialer.

Fire ulike AlMgSi-legeringer, 6005.40, C28, 6016 A og 6016 B, ble deformert ved valsing eller strekking enten før eller etter utherding, det vil si enten pre- eller post-deformasjon. Alle legeringer ble utherdet til T6 tilstand, og ett sett av 6016-prøver ble også utherdet for å simulere utherdingsprosessen i bilindustrien. Vickers hardhetsmålinger ble gjennomført for å evaluere effekten av deformasjon på hardhet. Videre ble de ulikt deformerte og varmebehandlede legeringene IGC-testet etter standard ISO 11846 (metode B), og deretter ble mikrostrukturen til de korroderte materialene undersøkt i lysmikroskop for å vurdere IGC-motstanden. I tillegg ble mikrostrukturen til ukorrodert 6005.40 undersøkt i sveipeelektronmikroskop og transmisjonselektronmikroskop for å vurdere effekten av deformasjon på mikrostrukturen.

Resultatene avdekket at pre-deformasjon etter innherding forbedret IGC-motstanden signifikant, spesielt for Cu-holdige legeringer, mens gode mekaniske egenskaper ble opprettholdt. Ved undersøkelser i transmisjonselektronmikroskop ble det vist at presipitatene i pre-deformerte materialer inneholder mer Cu enn i udeformerte materialer. Det antas at dette reduserer mengden Cu som er tilgjengelig for dannelse av en Cu-rik film på korngrensene, og dermed reduserer følsomheten for IGC. En overgang til grop-liknende korrosjon ble observert i pre-deformerte materialer. Pre-deformasjon etter pre-herding av materialer til bruk i bilindustrien viste seg å være uheldig for korrosjonsegenskapene. Det antas imidlertid at pre-deformasjon før pre-herding vil være fordelaktig for å oppnå optimal utherdingsrespons kombinert med gode korrosjonsegenskaper. Effekten av post-deformasjon på mekaniske egenskaper og korrosjonsegenskaper var tvetydig. Post-valsing forbedret IGC motstanden noe, men økte ikke hardheten. Post-strekking forbedret ikke IGC-motstanden, men økte hardheten til legeringene. Videre undersøkelser kreves for å oppnå kunnskap om korrosjonsmekanismen i post-deformerte materialer.

Contents

List of abbreviations

AA	Aluminum association
AC	Air cooling
β	Equilibrium phase in AlMgSi alloys (Mg_2Si)
β′	Metastable precursor to β
β″	Metastable precursor to β′
CW	Cold work
DC casting	Direct chill casting
EBSD	Electron backscatter diffraction
$\mathbf{E_c}$	Critical pitting potential
EDS	Energy dispersive X-ray spectroscopy
GP zones	Guinier-Preston zones
HAADF-STEM	High angle annular dark field scanning transmission electron microscope
HAGB	High angle grain boundary
IGC	Intergranular corrosion
L	Metastable precursor to Q′
LAGB	Low angle grain boundary
LM	Light microscope
Paint baked	Artificially aged at 185°C for 20 min
PFZ	Precipitate free zone
Post-deformation	Cold deformation after the final ageing treatment
Pre-baking	Pre-ageing procedure at 90°C for 24 h used in the automotive industry
Pre-deformation	Cold deformation before the final ageing treatment
Q-phase	Equilibrium phase in AlMgSi(Cu) alloys
Q′	Metastable precursor to Q
$\mathbf{R_{p0.2}}$	Yield strength, 0.2% offset

RT	Room temperature
SEM	Scanning electron microscope
SHT	Solution heat treatment/treated
SSSS	Supersaturated solid solution
TEM	Transmission electron microscope
T6	Solution heat treated and artificially aged to peak hardness at 185°C for 5 h
WQ	Water quenching

Chapter 1

Introduction

1.1 Background

The emissions of greenhouse gases are ever-increasing and great attention is directed towards reducing the emissions and ensure more sustainability in the transport sector and manufacturing industry among others. CO_2 emissions have increased globally by approximately 90% since 1970 [1] and the transport sector is responsible for nearly 25% of greenhouse gas emissions in Europe, according to the European Commission [2]. This elucidates the importance of exploring new solutions within the automotive industry. Reduction of vehicle weight may significantly reduce fuel consumptions, and annually savings of 220 metric tons CO_2 have been reported by replacing the current car fleet with lighter vehicles [3]. Aluminum has a density of only 2.7 g/cm^3 compared to 7.9 g/cm^3 for steel [4] and has therefore for years been considered as an alternative to steel in car bodies. There has been a doubling of the average amount of aluminum in passenger cars during the last decade, and it is predicted that this trend will continue in the following years [5]. Very recently, Hydro opened a new, state-of-the-art production line for aluminum parts to the automotive industry in Germany [6]. The valued properties of aluminum are high strength to weight ratio, good formability, good corrosion resistance and great recycling potential [7].

The primary choice of aluminum alloys in automobiles worldwide is the 6xxx series, with only a few exceptions [8]. The heat treatable 6xxx series contains Mg and Si, and is also referred to as AlMgSi alloys. These alloys are commonly used as rolled sheets or extruded profiles in automobiles in terms of bumper beams and crash elements among others [9]. The alloys possess an attractive combination of properties, including good corrosion resistance, good formability, low cost and medium strength [10]. However, efforts are made to manufacture AlMgSi alloys with improved strength due to a demand in the automotive industry for materials with increasingly superior mechanical properties. By alloying AlMgSi alloys with Cu, an optimal combination of mechanical properties is achieved, that is increased hardness, ductility and strength [10–12]. Nevertheless, addition of Cu is frequently reported in the literature to cause increased susceptibility to corrosion, and particularly intergranular corrosion (IGC) [12–15].

IGC is localized corrosion of material along the grain boundaries [16]. The IGC front propagates in the interior of the metal causing almost no visible damage on the surface, and hence the corrosion is extremely difficult to detect without the aid of microscope. Moreover, the sharp corrosion attacks produced by IGC could lead to fatigue cracking, which may have severe consequences [17]. Thus, there has been enormous research on the effect of Cu on the IGC susceptibility of AlMgSi alloys and how the Cu induced corrosion mechanism proceeds

[12, 13, 15, 16, 18, 19]. AlMgSi alloys become sensitized to IGC during thermomechanical processing, as Cu precipitates and forms a continuous, Cu rich, nanoscale film along the grain boundaries. A zone depleted of alloying elements appears adjacent to the grain boundaries. This could result in a microgalvanic cell and accordingly danger of IGC [13, 15, 16, 18, 19]. The corrosion properties of AlMgSi alloys are highly dependent on chemical composition, such as Cu content and Mg/Si ratio, and thermomechanical processing [12, 13, 15, 20].

As of today, a lot of research is done on the corrosion mechanism of AlMgSi alloys and great work is put down to map the factors affecting IGC in these materials [13–15, 21–23]. However, to expand the application areas of AlMgSi alloys in the automotive industry and other sectors, it is important to keep seek new solutions and work on improving the material properties. Cold deformation has been suggested as a measure to improve the IGC resistance of AlMgSi alloys. During deformation, the microstructure of the material is changed as dislocations are introduced in the material and the grains may become elongated and turn in the direction of deformation [24]. Moreover, pre-deformation, that is deformation prior to the final ageing treatment, affects the precipitation sequence and kinetics during ageing [25, 26]. It is believed that deformation may reduce the number of high angle grain boundaries and lead to a higher number of low angle grain boundaries in the material, which has been found to reduce the susceptibility to IGC [11, 27]. Moreover, the changes in precipitation during ageing as a consequence of pre-deformation may also be advantageous, considering that it is the precipitates that give rise to IGC [13, 16]. Results obtained by the author in previous work [28] imply that pre-deformation by rolling or stretching has beneficial effect on the IGC resistance of several AlMgSi alloys. Slightly pre-deformation is a common procedure today in manufacturing of many AlMgSi alloys [26, 29].

1.2 Objective

Still, limited documented work exists on the effect of deformation on the corrosion mechanism of AlMgSi alloys. The objective of this master thesis is to further investigate the effect of cold deformation on the IGC susceptibility of AlMgSi alloys and obtain a better understanding of the corrosion mechanism in these materials. In order to achieve this, alloys deformed by rolling or stretching, subjected to different ageing treatments, are IGC tested according to ISO 11846 (method B) and studied in light microscope. Both deformation before and after ageing, pre- and post-deformation respectively, are assessed. Hardness measurements are performed to document any changes in mechanical properties due to deformation. Moreover, to obtain a better understanding of the corrosion mechanism in deformed materials, studies in scanning and transmission electron microscope are conducted.

Chapter 2

Theoretical background - earlier work

2.1 AlMgSi alloys

Aluminum has a very attractive combination of properties and is accordingly the most utilized non-ferrous metal in the world [30]. Nevertheless, pure aluminum is soft and has low strength, hence other elements are usually added to improve the material properties [24]. Aluminum is divided into different series with particular features, depending on the alloying elements. Aluminum alloyed with Mg and Si is referred to as AlMgSi alloys or the 6xxx series, and is an important class of aluminum alloys suitable for use in structural, automotive and marine applications among others [10, 11, 13, 24, 31].

AlMgSi alloys are characterized as heat treatable or age hardenable alloys, which means they achieve strength through an ageing treatment where finely dispersed, strengthening precipitates are formed [32]. The equilibrium precipitate is Mg_2Si, and the stoichiometric Mg/Si ratio in Mg_2Si is 1.73 [24, 33]. Furthermore, AlMgSi alloys are wrought alloys, and the forming procedure for these materials is therefore plastic deformation like extrusion or rolling [24, 32]. Other characteristics of AlMgSi alloys are high corrosion resistance, moderate strength and excellent extrudability. Their excellent extrudability is of particular importance, as it enables design of complex, structural shapes [24, 34].

Other alloying elements than Mg and Si are frequently required in AlMgSi alloys to improve the material properties. Mn or Cr may be added to inhibit recrystallization and grain growth during heat treatment [24, 35]. Cu or Si in excess of the Mg_2Si stoichiometry is added to improve mechanical properties [36], although addition of Cu may have detrimental effect on the corrosion resistance as elaborated in later sections. An overview of typical chemical composition of some relevant AlMgSi alloys is presented in Table 2.1 and a short introduction to each alloy is given in the following sections.

Table 2.1: Typical chemical composition of relevant AlMgSi alloys in wt%. The balance is Al [33, 37, 38].

	Si	**Fe**	**Cu**	**Mn**	**Mg**	**Zn**	**Ti**	**Cr**
6005	0.6-0.9	0.35	0.10	0.10	0.40-0.6	0.10	0.10	0.10
6082	0.7-1.3	0.50	0.10	0.40-1.0	0.6-1.2	0.20	0.10	0.25
6016	1.0-1.5	0.50	0.20	0.20	0.25-0.6	0.20	0.15	0.10

AA6005

AA6005 is a usually extruded, medium strength alloy that consists of a relatively large excess Si content compared to similar alloys in the 6xxx series. Moreover, AA6005 is less quench sensitive and easier to extrude than comparable alloys. Hence, this alloy can be used for applications requiring complex shapes, for example handrail tubing, automotive parts and structural members. Good surface finish is also a quality of this alloy [37].

C28

C28 is an extruded alloy developed for use in the automotive industry. Its microstructure and properties are carefully designed to respond to the requirements for use in vehicles, for instance in front structures [39]. The alloy chemistry is similar to that in AA6082 and typical chemical composition of AA6082 is shown in Table 2.1. The name "C28" implies a requirement to $\mathrm{R_{p0.2}}$ of being minimum 280 MPa. Other properties of C28 are good corrosion resistance, $\mathrm{R_{p0.2}}$ above 265 MPa after 1000 hours at 150°C and good crashing performance [40].

AA6016

Unlike the former described alloys, AA6016 is normally used as rolled product in for instance outer body panels in cars, and the alloy is the primary choice of aluminum sheets among automotive manufacturers in Europe [41]. This requires properties like good surface finish, good formability, high dent resistance and good hemming performance. Furthermore, the alloy must develop sufficient strength upon a special ageing treatment termed paint baking, used in automotive manufacturing [41, 42]. Typical chemical composition of AA6016 is presented in Table 2.1.

2.2 Processing route for AlMgSi alloys

Wrought aluminum alloys are usually processed by plastic deformation at high temperatures, for example hot rolling or hot extrusion [24]. During these processes, semi-fabricated products are produced from cast billets by an applied force [35, 43]. Figure 2.1 presents an overview of the processing chain of wrought aluminum alloys from liquid metal to final product formed by extrusion or rolling. The quality and properties of the final product depend on the performance in all processing steps, considering that each step alters the microstructure [44].

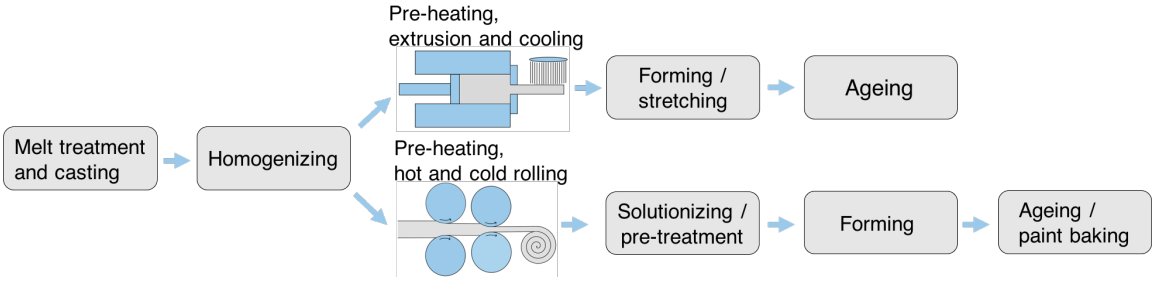

Figure 2.1: Schematic illustration of processing chain of wrought aluminum alloys. Constructed with information provided by [45, 46].

2.2.1 Melt treatment and casting

The first step in processing of AlMgSi alloys is melt treatment, where aluminum is melted and thoroughly mixed with alloying elements [47]. To obtain good billet quality, impurities like oxides and inclusions are removed by fluxing, degassing and filtering [35]. The molten metal is poured into water-cooled molds and cast by direct chill (DC) casting to form cylindrical or rectangular billets for extrusion and rolling, respectively [35, 47]. The billet quality, and in turn the quality of the final product, is also determined by casting temperature, casting speed, water flow and other parameters [47]. The typical casting temperature for AlMgSi alloys is around 680-700°C [45].

2.2.2 Homogenization

Alloying elements tend to segregate to the grain boundaries during casting and a non-homogeneous alloy chemistry arises. To remove this microsegregation and eliminate casting stresses, homogenization is performed subsequent to casting [33, 45, 47, 48]. Homogenization is conducted by heating the billet to a certain temperature, about 580°C for AlMgSi alloys, hold the billet at this temperature and thereafter cool the billet [45]. The heating rate, time required at the homogenization temperature and cooling rate are dependent on the diffusion rates of the alloying elements, as homogenization is a diffusion process [47, 48]. It is important that these parameters are selected carefully to achieve the desired result.

Other important processes occur during homogenization of AlMgSi alloys. Precipitation of dispersoids which impede recrystallization, such as Mn and Cr, is promoted [48]. Moreover, insoluble AlFeSi particles are transformed from β to α phase. Plate-like β-AlFeSi has an adverse interface with the aluminum matrix and is for that reason surrounded by stress fields. By transforming this phase to the more rounded α-AlFeSi particles, the stress fields are reduced, which induces increased ductility and workability in the alloy [48, 49].

2.2.3 Fabrication of DC-cast billets

The homogenized billet is formed into the requested shape by hot extrusion or hot rolling, as illustrated in Figure 2.1. Complex geometries can be produced relatively inexpensive by extrusion, whereas simpler shapes like plates and sheets are formed by rolling [50].

Hot extrusion

In Figure 2.2 a time-temperature relationship during processing of extruded AlMgSi alloys is illustrated. Prior to extrusion the homogenized billet is heated to a temperature between 440-500°C to ease plastic deformation [45]. Subsequently, the billet is placed in the extrusion chamber and subjected to compressive forces, which press the billet through the extrusion die and cause a reduction in the billet cross section [45, 47].

The microstructure of the resulting extrudate is highly affected by the chemical composition of the alloy, as well as extrusion parameters, such as temperature, extrusion speed and frictional effects [47]. Aluminum alloys have high stacking fault energy and hence dynamic recovery occurs in the deformation zone during extrusion. Due to formation of dislocations during deformation and high dislocation mobility at high temperatures, dynamic recovery proceeds by formation of subgrains. The extrudate leaves the press with a fibrous, unrecrystallized subgrain structure. However, since the surface of the extrudate is heavier deformed than the bulk, static recrystallization occurs on the surface and partially throughout the thickness of the material, depending on alloy chemistry and cooling rate [51].

Svenningsen et al. [21] studied the microstructure of extruded AlMgSi alloys and found that the degree of recrystallization was dependent on the Cu content. The samples with lower Cu content possessed a fibrous texture in the center region and a recrystallized surface layer, whereas the samples with higher Cu content were fully recrystallized.

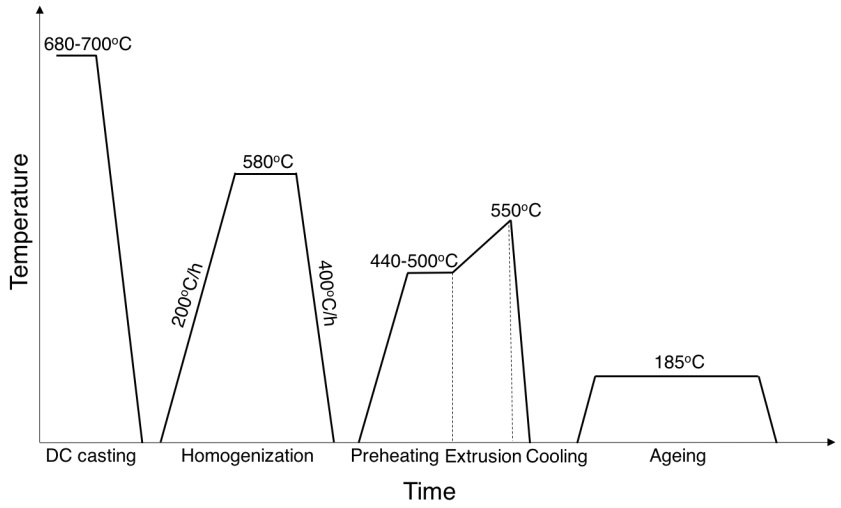

Figure 2.2: Schematic illustration of potential time-temperature relationship during extrusion of AlMgSi alloys. Constructed with information provided by [45].

Hot rolling

Hot rolling is conducted by passing the homogenized billet, heated to about 525°C, through opposite rotating rolls. This process is repeated until the desired plate thickness is achieved or the metal is thin enough to be coiled [50]. The thickness is usually reduced from a billet thickness of 200-600 mm to 2.5-8 mm prior to coiling. Cold rolling may successively be performed to obtain even further reduction in thickness [35].

As during extrusion, the microstructure is changed during rolling. The grains become elongated in the rolling direction, and recovery and partial recrystallization take place depending on rolling temperature and alloy composition among others [35]. Lee et al. [52] studied the effect of hot rolling on the microstructure of AlMgSi alloys and found that for otherwise constant rolling conditions, increasing the rolling temperature from 300°C to 350°C resulted in a fully recrystallized grain structure throughout the thickness, compared to only recrystallization at the surface and fibrous texture in the center region for rolling at the lower temperature.

2.3 Age hardening of AlMgSi alloys

Age hardening is a strengthening mechanism applicable to all heat treatable alloys [24]. To achieve age hardening in a material it is required that the solid solubility of the solute in matrix rapidly decreases with decreasing temperature [53], and this requirement is met by all heat treatable alloys, including AlMgSi alloys. The mechanism of age hardening is based on that particles or precipitates of secondary phases act as obstacles for movement of dislocations through the matrix, and hence prevent deformation [24]. These precipitates are produced as a result of an ageing treatment, which is a three-step process [33, 53, 54];

1. Solution heat treatment
2. Quenching
3. Ageing

Solution heat treatment

First step in the ageing procedure is solution heat treatment (SHT) where the material is heated to a high temperature below the solidus line [53]. This is illustrated in Figure 2.3 by label one. The microstructure development during the ageing treatment is also shown. All solute atoms are dissolved to form a homogeneous solid solution, α, and a high concentration of vacancies is generated [24, 33, 53]. SHT often occurs concurrently with extrusion in processing of AlMgSi alloys, since the extrusion temperature is sufficiently high to dissolve all solute atoms [55].

Quenching

After adequate time at high temperature to dissolve all solute atoms, the material is quenched to room temperature, as indicated by label two in Figure 2.3. Diffusion rates are low at room temperature, hence formation of Mg-Si secondary phases by diffusion is impeded and a non-equilibrium supersaturated solid solution (SSSS) of Mg_2Si in the α phase is formed [53, 55]. Moreover, the high concentration of vacancies is preserved [24, 55].

The required cooling rate from high temperature is primarily depending on chemical composition of the alloy [33]. Water quenching is usually necessary to obtain satisfying properties in AlMgSi alloys, because these alloys commonly contain Cr and Mn. Cr and Mn form dispersoids, which serve as nucleation sites for non-hardening Mg-Si precipitates if the cooling rate is not sufficiently high. This reduces the age hardening capability and deteriorates mechanical properties [56]. For the AlMgSi alloys in which SHT is conducted concurrently with extrusion, water quenching at the die exit is performed [55].

Ageing

The precipitates which impede dislocation movement are formed during ageing. This can occur at room temperature, so-called natural ageing, where the material obtains appreciable strength after adequate time due to clustering of Mg and Si atoms [57]. Nevertheless, commercial, heat treatable aluminum products are commonly artificially aged by heating the alloys to elevated temperature within the α + Mg_2Si two phase region, as illustrated by label three in Figure 2.3 [33, 53]. At higher temperature diffusion rates of solute atoms become higher and the alloying elements precipitate out of solid solution to form metastable Mg-Si precipitates [24]. The high concentration of vacancies frozen in the material during SHT and quenching eases the movement of Mg and Si through the crystal lattice, giving finely dispersed precipitates [33].

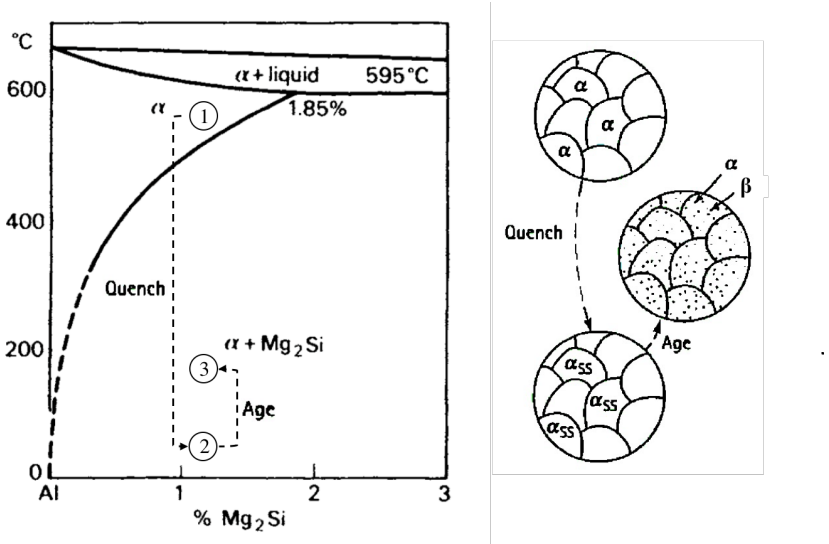

Figure 2.3: Pseudo binary phase diagram for Al-Mg_2Si [35, 58, 59]. Schematic illustration of microstructure development during ageing treatment is adapted from [43].

The temper conditions of solution heat treated (SHT) and subsequently artificially aged aluminum alloys are divided into underaged, peak aged and overaged condition, depending on ageing time [24]. Peak aged temper is related to maximum hardness, whereas both underaged and overaged materials have lower hardness than the hardness capability of the alloys [24, 32]. In Table 2.2 some relevant tempering groupings for heat treatable aluminum alloys are displayed.

Table 2.2: Temper designations for heat treatable aluminum alloys [60].

Designation	Alloy condition
T4	Solution heat treated and naturally aged.
T5	Cooled from fabrication temperature and artificially aged.
T6x	Solution heat treated and artificially aged to underaged temper.
T6	Solution heat treated and artificially aged to peak aged temper.
T7	Solution heat treated and artificially aged to overaged temper.
T8	Solution heat treated, cold worked, and artificially aged.
T9	Solution heat treated, artificially aged, and cold worked.

2.3.1 The paint bake cycle in the automotive industry

Sheets and profiles for automotive applications are subjected to a special ageing procedure since the conventional ageing treatment involves too long ageing times to be applicable to processes in the automotive industry. The alloys are aged in the so-called paint bake cycle, in which the strength increases while the paint is cured. However, this procedure involves too low temperatures and too short times to utterly utilize the age hardening capability of the alloys. Moreover, natural ageing will occur as the materials are stored for some time before they are aged at the automobile plant, and this may have adversely impact on the mechanical properties. Thus, a pre-baking procedure is performed prior to paint baking to improve ageing capability during the paint bake cycle and to avoid natural ageing. Pre-baking involves heating the materials to a certain temperature shortly after SHT and quenching. Formation of clusters which transform into hardening precipitates upon paint baking is facilitated and the aim is to accelerate the following ageing [61]. However, pre-baked and subsequently paint baked alloys are still in somewhat underaged temper [62–64].

2.3.2 The precipitation sequence during ageing

The precipitates formed during ageing and their microstructure are of greatly importance for material properties [65]. Alloy composition and thermomechanical history determine how the precipitation occurs and which precipitates are formed [26, 55]. The precipitation sequence in AlMgSi alloys is therefore complex and numerous studies on the subject have been performed. The generally accepted and well documented precipitation sequence in AlMgSi alloys is presented in equation 2.1 [35, 45, 55, 65–69]. Prior to formation of the

equilibrium phase, Mg_2Si, metastable secondary phases with lower interfacial energy form [31, 69, 70].

$$\text{SSSS} \rightarrow \text{Atomic clusters} \rightarrow \text{GP zones} \rightarrow \beta'' \rightarrow \beta' \rightarrow \beta\ (Mg_2Si) \tag{2.1}$$

In Si rich alloys with Mg/Si ratio smaller than the stoichiometric amount in Mg_2Si, the precipitation sequence is found to differ slightly from equation 2.1. Other precipitates termed U1, U2 and B′ are found in combination with the β′ phase [55, 71]. Moreover, Si plates are formed in addition to β at longer ageing times [65].

Figure 2.4 displays a schematic illustration of hardness of an AlMgSi alloy as a function of artificial ageing time. In addition, related ageing tempers and precipitates are shown. It is important to emphasis that the predominating precipitate at a given ageing temper is dependent on alloy composition and ageing temperature [55]. Thus, for some alloys this schematic illustration might not be completely correct.

Initially during ageing, Mg and Si tend to diffuse to vacancies preserved in the crystal lattice by vacancy diffusion, and small clusters of Mg and Si are formed. The degree of supersaturation in solid solution affects the formation of clusters; higher degree of supersaturation generates more vacancies in the lattice and hence higher number of fine clusters [24]. The Mg-Si clusters serve as nucleation sites for Guinier-Preston zones (GP zones), which are formed by continued clustering of solutes with vacancies [24, 66]. The shape of the GP zones is discussed in the literature and described as either spheres [24, 69] or needles [55] coherent with the matrix and oriented along the $(100)_{Al}$ planes. As Figure 2.4 is illustrating, these GP zones only give a small contribution to hardness [24].

The needle shaped, semi-coherent β″ aligned along the $(100)_{Al}$ planes, nucleates on the GP zones [55, 65, 66, 68, 69]. The chemical composition of this precipitate is found to be Mg_5Si_6 [55], although some uncertainty about the chemical composition exists [24]. Marioara et al. [55] found that the highest hardness during ageing was reached for AlMgSi alloys with Mg/Si ratio optimized for Mg_5Si_6, that is Si in excess regarding the Mg_2Si stoichiometry. A finer precipitate microstructure, but lower volume fraction of precipitates was observed in Si rich alloys, resulting in increased hardness [55]. As shown in Figure 2.4, β″ is the predominating precipitate in underaged temper. With increasing ageing time, the needle shaped precipitate increases in length, providing higher hardness. Thus, β″ is responsible for maximum hardness in AlMgSi alloys [66]. It is found that the needle length in Si rich alloys increases more slowly than in Mg rich alloys. This results in broader peak at maximum hardness and finer precipitates in Si rich alloys, whereas faster overageing and coarser precipitates are observed in Mg rich alloys [55]. On the other hand, Murayama et al. [64] observed faster ageing kinetics in excess Si alloys.

In overaged temper and accompanying state of reduced hardness, β′ is the predominating precipitate. This precipitate is rod [66, 68] or needle shaped [55] and semi-coherent with matrix. The equilibrium phase, β, does not form below 200°C [55] and contributes little to the strength and hardness. This phase is shaped as platelets and is incoherent with matrix [66].

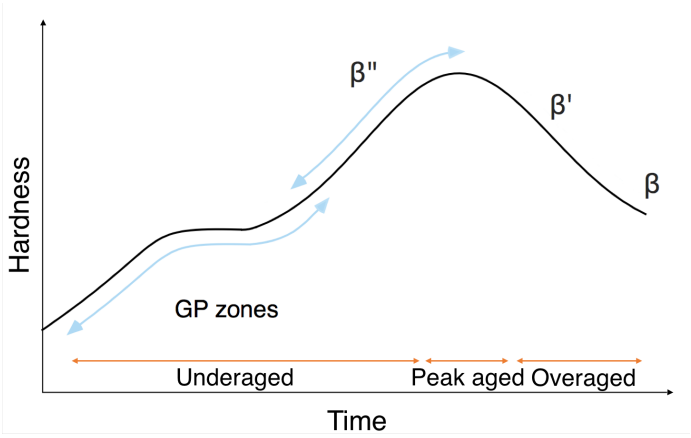

Figure 2.4: Schematic diagram showing hardness as a function of ageing time at constant temperature (> 100°C) during artificial age hardening of an AlMgSi alloy. Reproduced from [53, 70].

Effect of Cu addition on the precipitation sequence

AlMgSi alloys achieve increased strength, hardness and ductility upon addition of Cu. The advantageous effect of Cu on these properties is mainly due to a refinement in the precipitate dispersion [65, 68, 69]. Moreover, Murayama et al. [64] claim that the kinetics of precipitation during artificial ageing and precipitate volume fractions increase as a consequence of Cu addition. Holmestad et al. [72], on the other hand, found that the precipitation kinetics remained unchanged upon addition of Cu. Nevertheless, occurrence of Cu alters the precipitation sequence since Cu is incorporated into the metastable phases. The exact microstructure of these secondary phases has yet to be established [72–74]. However, the presence of a quaternary Q phase containing Al, Mg, Si and Cu is documented and suggested compositions are $Al_5Cu_2Mg_8Si_6$ or $Al_4CuMg_5Si_4$ among others [74].

The altered precipitation sequence is presented somewhat simplified in equation 2.2 [65, 68]. It is found a significantly lower contribution of β'' to peak hardness in Cu containing AlMgSi alloys due to lower number density [65]. However, the needle shaped Q′ precursor, L, is believed to have considerable hardening capability and may be the main hardening phase in AlMgSi(Cu) alloys [65, 68]. The needle [65] or lath shaped [74] Q′ precipitate is coherent and aligned along the $(100)_{Al}$ planes. This phase is related to overaged temper [68].

$$\text{SSSS} \rightarrow \text{Atomic clusters} \rightarrow \text{GP zones} \rightarrow \beta'', \text{L} \rightarrow \beta', \text{Q}' \rightarrow \text{Q} \tag{2.2}$$

Precipitation on grain boundaries

Grain boundaries, which are separating different grains in a material, are related to an interfacial energy due to the more irregular bonding of atoms along the boundary. This energy increases with increasing degree of misorientation between adjacent grains. Low

angle grain boundaries (LAGBs), which have lower energy, are defined as grain boundaries between grains with misorientation angle less than 15°, whereas high angle grain boundaries (HAGBs) have larger energy and misorientation angle larger than 15°. Due to the interfacial energy, grain boundaries are more chemically active than the grains themselves [53]. This results in heterogeneous precipitation of secondary phases on grain boundaries rather than homogeneously in the matrix [24].

Minoda et al. [11] studied the effect of grain boundary characteristics on precipitation in an AlMgSi alloy and found that grain boundary precipitates were rare on LAGBs, but occurred on HAGBs. Yang et al. [27] found that Cu containing Q′/Q phases precipitated on HAGBs, whereas Cu free pre-β″/β″ existed on LAGBs in an AlMgSi alloy with 0.13 wt% Cu. Accordingly, the energy of the grain boundaries affects the precipitation process.

2.3.3 Strengthening mechanisms during ageing

The mechanical properties of age hardened AlMgSi alloys depend on precipitate properties like chemical composition, size, distribution and coherency. Generally, it is the precipitates' ability to prevent dislocation movement that determines the strength and hardness of heat treatable aluminum alloys [24, 53, 70]. Different strengthening mechanisms act during ageing, giving rise to varying extent of hardness and strength. These strengthening mechanisms are coherency strain hardening, chemical hardening and dispersion hardening [70]. Their active period and contribution to hardness are illustrated in Figure 2.5a. Schematic illustrations of the different strengthening mechanisms are shown in Figure 2.5b.

Coherency strain hardening

Small, coherent GP zones and precipitates which are finely dispersed predominate initially during ageing [66]. Due to a size difference between the precipitates and the aluminum atoms, stress fields surround the precipitates, as shown in Figure 2.5b. Dislocations interacting with these stress fields give rise to strength and hardness in the material, as the stress fields act as obstacles for dislocation movement [24]. At longer ageing times, the precipitates coarsen and they become more widely spaced, causing increased hardness. If the precipitates become too widely spaced, the hardness will decrease. This strengthening mechanism causes maximum hardness when the distance between the precipitates is of the same order as the radius of curvature of the dislocations [35, 70].

Chemical hardening

As the precipitates predominating early in the ageing process are small and coherent, they become sheared by dislocations, as illustrated in Figure 2.5b. An additional stress is required to shear through the precipitates among others because a new particle-matrix interface is formed, and this increases the mechanical response of the material. Hardness resulting from this mechanism is referred to as chemical hardening [70].

Dispersion hardening

The third strengthening mechanism acts in peak and overaged temper. When the particles have become semi-coherent or incoherent with matrix, the misfit stresses due to size differences disappear and the particles are no longer sheared. The dislocations are now able to pass the particles and form Orowan loops around them. Hardening results from the increased stress required to bow the dislocation line between the particles and form loops around them [70].

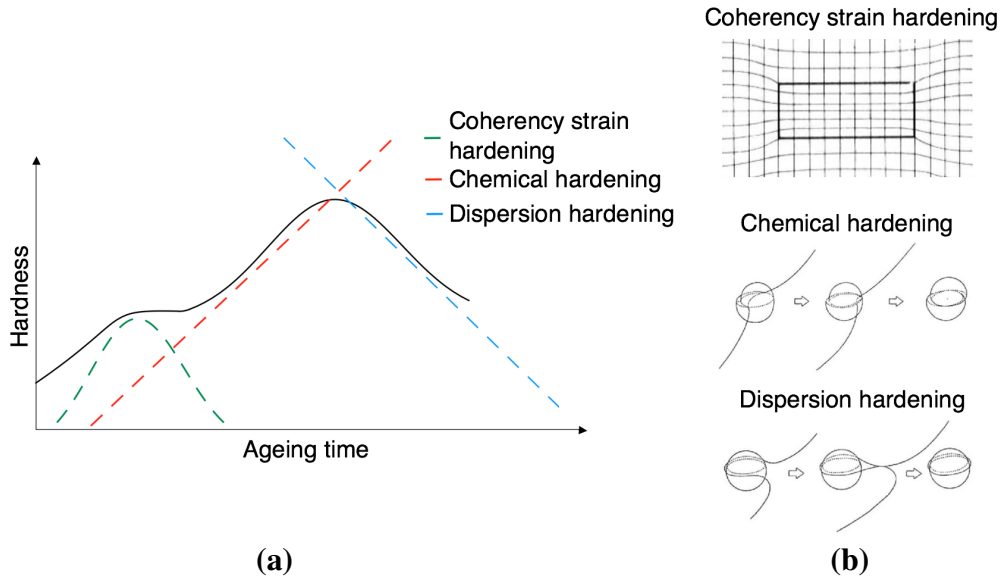

Figure 2.5: Schematic diagram showing the hardness contribution of different age hardening mechanisms as a function of ageing time, and the accompanying hardness during ageing of an AlMgSi alloy, reproduced from [75]. In addition, illustrations of the different hardening mechanisms are included [24, 76].

2.4 Pre-deformation of AlMgSi alloys

Many products made of AlMgSi alloys are additionally formed by for instance rolling or stretching after hot forming and prior to ageing [26]. This process is generally referred to as pre-deformation. The aim is to relieve quench-related internal stress which may affect the alloy during later machining [29], but pre-deformation may also affect the microstructure, precipitation sequence and mechanical properties [24, 26, 77]. The typical industrial practice is to stretch the materials, considering that extruded products often have complex shapes.

Pre-deformation is commonly conducted at a temperature below the material's recrystallization temperature and is accordingly termed cold working. The material may be deformed to various levels and the degree of plastic deformation is sometimes expressed as percent cold work (%CW). Percent cold work may for instance be expressed as given in equation 2.3, where A_0 is the original area of the cross section that experiences deformation and A_d is the area after deformation [53].

$$\%\mathrm{CW} = \left(\frac{\mathrm{A_0} - \mathrm{A_d}}{\mathrm{A_0}}\right) \cdot 100 \tag{2.3}$$

2.4.1 Strengthening mechanism during deformation

Deformation causes increased hardness and strength in a material for the same reason as age hardening; hindrance of dislocation movement. Strengthening by deformation is termed strain hardening and results as a consequence of increased dislocation density. Dislocations are generated in the material during deformation and the dislocation density is therefore increased. Due to repulsive strain interactions between dislocations, the large number of dislocations will prevent each others movement, hence improving the mechanical response [53].

Strain hardening is illustrated in Figure 2.6. If dislocation line A is about to move to the right due to an applied stress, it interacts with the disordered lattice adjacent to dislocation line B, and hence its movement is hindered and a larger imposed stress is required for dislocation movement [43]. The strength and hardness of the material increase with increasing %CW [53].

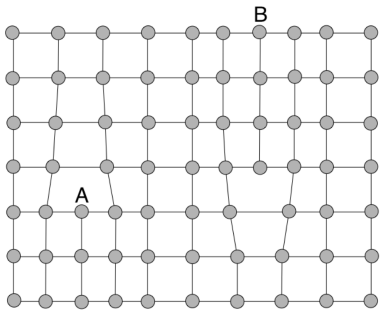

Figure 2.6: Illustration of strain hardening. Dislocation movement is hindered by presence of other dislocations. Reproduced from [43].

2.4.2 Effect of pre-deformation on microstructure

An important aspect during pre-deformation is that the microstructure of the material changes. There may be a change in grain shape to a more elongated form and an accompanying rise in total grain boundary area due to accumulation of dislocations. Moreover, the orientation of the grains can be altered relative to the direction of deformation [78].

Changes in microstructure are illustrated in Figure 2.7 for a material subjected to rolling. If a recrystallized material is rolled or stretched to sufficient extent, it may obtain a texture as shown in Figure 2.7, and the number of LAGBs may be increased. However, these changes in microstructure are highly dependent on %CW [24]. Modest rolling results in a more heavily deformed surface and gradually reduction of %CW towards the center. Stretching, on the other hand, causes uniform deformation throughout the material thickness. The

mentioned changes in microstructure may also occur for a material that is deformed after ageing, so-called post-deformation.

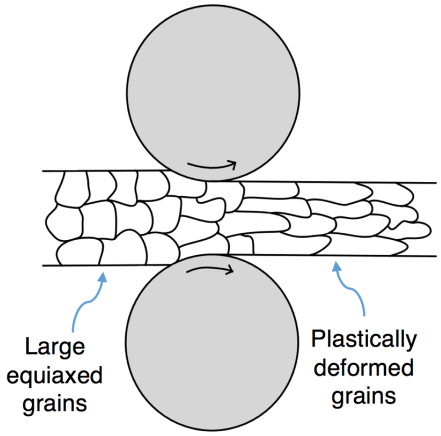

Figure 2.7: Illustration of changes in microstructure during rolling of a material with initially equiaxed grains. Reproduced from [24].

Large amounts of energy are stored in a material subsequent to deformation due to the high dislocation density [78]. In a successive heat treatment such as ageing, the stored energy is released by dislocation movement. This process is termed static recovery and occurs by annihilation of dislocations or rearrangement of dislocations into lower energy configurations. Material properties are partly restored to their values before deformation, causing impaired strain hardening [53, 78]. Moreover, formation of dislocation free subgrains with LAGBs may occur, in which the dislocations arrange in the form of a three-dimensional cell structure and eventually form subgrains [78]. This is illustrated in Figure 2.8.

Several parameters are affecting the recovery process. More complete recovery occurs for materials with high stacking fault energy, such as AlMgSi alloys, and at higher ageing temperatures. If the temperature during heat treatment is sufficiently high, recrystallization occurs rather than recovery as these are competing processes. Furthermore, degree of deformation and deformation temperature affect recovery [78].

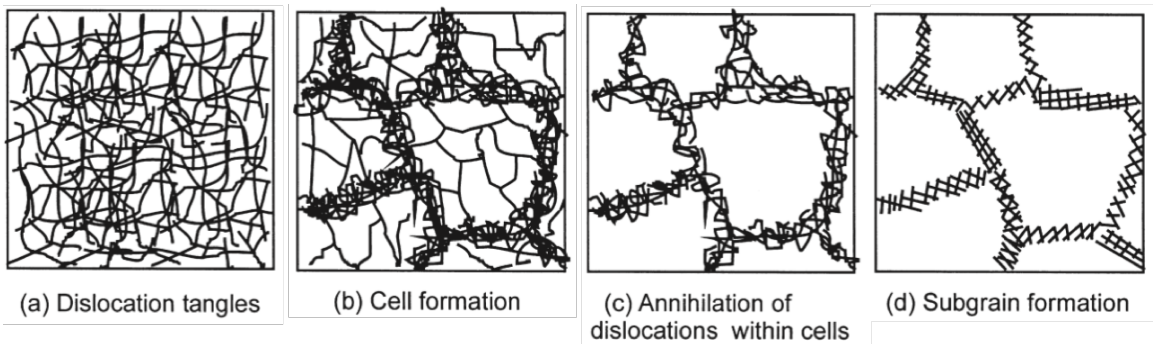

Figure 2.8: Illustration of the various stages during recovery of a plastically deformed material [78].

It is apparent that the high dislocation density in a pre-deformed material is considerably reduced during ageing. Furu et al. [79] found that the dislocation density was reduced due to recovery from $5 \cdot 10^{14}$ m^{-2} to $2 \cdot 10^{14}$ m^{-2} subsequent to peak ageing of AA6005, pre-deformed 10%. Nevertheless, the dislocation density after ageing is higher in sufficiently pre-deformed materials than undeformed materials, at least in underaged temper. Zhen et al. [25] studied the dislocation density in an AlMgSi alloy pre-deformed 0, 2, 5 or 10% and subsequently aged at 180°C for 30 min. The dislocation density in the 2% pre-deformed specimen was higher than in the undeformed specimen after ageing, but the difference was not substantial. The dislocation density in the 5 and 10% pre-deformed specimens, on the other hand, was much higher than in the 2% pre-deformed specimen.

2.4.3 Effect of pre-deformation on precipitation during ageing

Dislocations that affect the clustering process and alter the precipitation sequence and kinetics during ageing, are introduced in a material during pre-deformation [25, 26]. Zhen et al. [25] studied the effect of pre-deformation on the microstructure of AlMgSi alloys, and found that β″ precipitated on dislocations in pre-deformed materials rather than homogeneously in the matrix. Moreover, the size of the β″ precipitates formed on dislocations was found to be much larger than in undeformed materials. The increase in precipitate size was owed to dislocation pipe diffusion, in which the activation energy for diffusion of solutes in dislocation rich materials is lowered [80]. In other words, pre-deformation results in accelerated precipitation kinetics [26, 77]. By alloying with Cu, the coarsening effect of precipitates related to pre-deformation is reduced, giving finer microstructure and higher hardness in materials containing Cu [81].

Zhen et al. [25] also discovered that the density of β″ increased with increasing pre-deformation up to 5%. However, at 10% pre-deformation, the β″ density was clearly reduced. They claimed that the increase in precipitate density was attributable to lower activation energy for nucleation of β″ in dislocation rich materials. However, at 10% pre-deformation, larger precipitates grew by consuming smaller ones, and hence the precipitate density decreased [25]. Quainoo et al. [82] attributed the lower activation energy for nucleation of β″ to the high energy state induced in the material as a consequence of deformation, which enabled formation of β″ with lower energy.

Teichmann et al. [26] found similar results for a 10% pre-deformed AlMgSi alloy; coarser β″ precipitates and considerably reduced percentage of β″ in favor of more stable post-β″ phases. They attributed these findings to dislocations acting as vacancy sinks, which led to depletion of vacancies in the matrix. Furthermore, this made it more difficult to form GP zones which subsequently affected the formation of β″. Hence, pre-deformation promoted formation of post-β″ phases [26, 29]. Yassar et al. [83] found that β′ and Q′ precipitates were formed instead of β″ during ageing of pre-deformed AA6022 with 0.06 wt% Cu.

2.4.4 Effect of pre-deformation on mechanical properties

Hardness in pre-deformed and subsequently artificially aged materials is a combined effect of strain hardening and age hardening, and since the precipitation process in pre-deformed materials is altered, the hardening mechanism is complex [60]. Kolar et al. [77] have studied the effect of pre-deformation on hardness of artificially aged AA6060. The extruded material was pre-deformed by stretching and artificially aged at different temperatures. It was found that independent of ageing temperature, the pre-deformed specimens reached considerably higher peak hardness than the undeformed specimens. Moreover, the pre-deformed specimens reached peak hardness after shorter ageing time due to accelerated precipitation kinetics, as in accordance to the theory elaborated in section 2.4.3. The effect of pre-deformation on hardness for specimens aged at 175°C is presented in Figure 2.9a. Quainoo et al. [82] found that both yield and tensile strength of Cu containing AlMgSi alloys increased with increasing pre-deformation up to 5% after ageing at 180°C. However, the degree of pre-deformation was found to not affect the time to reach peak strength.

Other findings were obtained by Furu et al. [79] who studied the yield strength of AA6005 with 0.15 wt% Cu, pre-deformed to various degree and aged at 185°C. The result, presented in Figure 2.9b, revealed that maximum yield strength was independent of whether the material was pre-deformed or not. Nevertheless, it was found that the time to reach peak strength became shorter with increasing pre-deformation, but the specimens were at their maximum strength for relatively long periods of time at the ageing temperature. Dutkiewicz et al. [84] found that 30% pre-deformation did not change the maximum hardness of a subsequently peak aged AlMgSi(Cu) alloy.

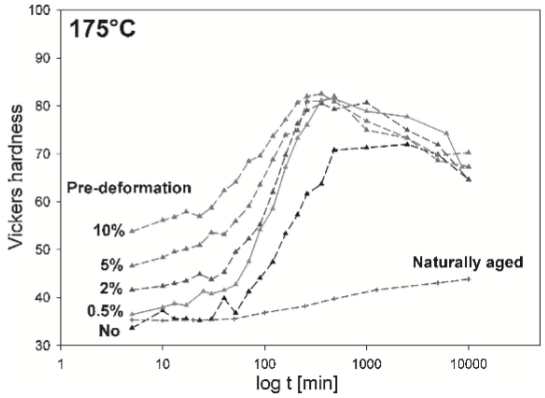

(a) Vickers hardness of AA6060 pre-deformed to various degree and artificially aged at 175°C [77].

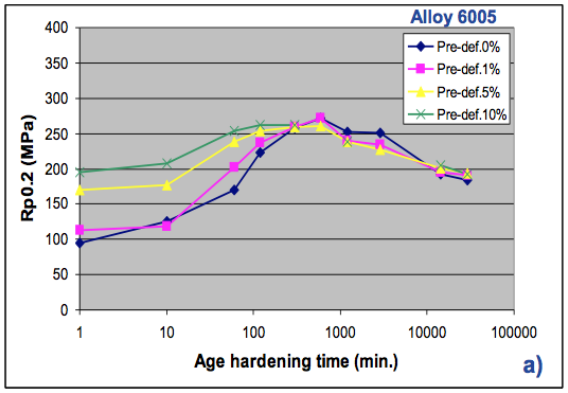

(b) Yield strength of AA6005 pre-deformed to various degree and artificially aged at 185°C [79].

Figure 2.9: Mechanical properties of AlMgSi alloys as a function of pre-deformation and ageing time.

2.5 Corrosion behavior of AlMgSi alloys

Aluminum is covered by an extremely stable, uniform oxide film which forms spontaneously and generally protects the underlying metal from corrosion attacks. Hence, aluminum is considered as having good corrosion properties in atmospheric conditions [33, 85]. The oxide film is crucial for aluminum's corrosion resistance and its stability is determined by environmental conditions and alloying elements [33]. The 6xxx series is known to be highly corrosion resistant as the alloying elements Si and Mg are incorporated into the oxide film, rendering it even more stable [24]. However, addition of Cu or improper thermomechanical treatment to achieve satisfying mechanical properties may introduce susceptibility to corrosion [11, 12, 14]. The detrimental factor leading to corrosion in these cases is microgalvanic coupling between the aluminum matrix and intermetallic secondary phases, which form electrochemical micro-cells if they are exposed to corrosive media [86]. The form of corrosion attack propagating from these micro-cells is determined by alloy microstructure, and consequently chemical composition and thermomechanical treatment [14, 86]. AlMgSi alloys are commonly susceptible to intergranular corrosion (IGC) and/or pitting corrosion [13]. The corrosion potential of different phases relevant to AlMgSi alloys is displayed in Table 2.3.

Table 2.3: Corrosion potential of different phases relevant to AlMgSi alloys [36, 87]. The potentials are measured with reference to a 0.1 M calomel electrode in a solution of 53 g/L NaCl and 3 g/L H_2O_2 at 25°C.

Phase	**Potential [V]**
Cu	-0.12
Si	-0.26
Mg_2Si	-0.83
Al (99.95 %)	-0.85
Mg	-1.65

2.5.1 Intergranular corrosion

IGC is localized corrosion where material along the grain boundaries is preferentially attacked [33]. The significance and appearance are depending on alloy composition and thermomechanical treatment [17, 88]. Considering that IGC impairs the mechanical integrity and is extremely difficult to observe by the naked eye, it may cause seriously damage. Moreover, the knife-line corrosion attacks produced by IGC are claimed to act as more severe stress raisers than pits do. Consequently, fatigue cracking occurs faster due to IGC than due to pitting [17].

It is commonly agreed that heat treatable aluminum alloys become sensitized to IGC during thermomechanical processing [13, 14, 20]. Alloying elements, such as Mg, Si and Cu, diffuse to the grain boundaries and precipitate during the ageing treatment. Grain boundaries act as vacancy sinks and fast diffusion paths for solutes due to their higher interfacial energy.

Precipitation of solute atoms adjacent to grain boundaries is therefore prevented as a result of the low vacancy concentration [24]. Accordingly, a zone depleted of alloying elements and precipitates forms along the grain boundaries. This zone is referred to as precipitate free zone (PFZ). The difference in chemical composition between the PFZ, the precipitates and the matrix leads to a difference in electrochemical potential [16]. Microgalvanic effects arise if a corrosive media is present and the difference in electrochemical potential exceeds 100 mV [85]. Commonly, IGC occurs in AlMgSi alloys due to electrochemical potential differences between noble precipitates on the grain boundaries and the PFZ, where the precipitates act cathodic and metal oxidation of the PFZ occurs [16, 85]. IGC usually initiates from a pit at the surface and propagates in the interior of the material [16].

Effect of Cu and Mg/Si ratio on IGC

Enormous research exists on the effect of Cu addition on the IGC susceptibility of AlMgSi alloys and it is well proven that increasing Cu content increases susceptibility to IGC [12, 14–16, 18, 89]. However, understanding the mechanism which is causing more severe IGC in Cu containing alloys has not been straight forward and different mechanisms have been proposed through the years. Precipitation and microgalvanic coupling of discrete AlCu, CuSi or AlMgSiCu (Q) phases with the PFZ were believed to cause IGC [14, 90]. However, precipitation of discrete particles at the grain boundaries is not sufficient to cause continuous, knife-line IGC attacks. Moreover, precipitation of an AlCu phase is not possible based on thermodynamic considerations [13]. Worsened IGC resistance due to Cu addition is rather found to be attributable to formation of a continuous, Cu rich, nanoscale film along the grain boundaries, as well as Cu containing Q or Q′ phases [13, 15, 18, 19, 72]. The Cu rich film is believed to be a precursor to the Q phase [13, 15].

During the ageing treatment, Cu and other alloying elements segregate to the grain boundaries and a Cu rich film, as well as a Si, Mg and Cu depleted zone, is formed along the grain boundaries [18, 72, 91]. The Cu rich film acts as an effective cathode, whereas the PFZ acts as an anode and will dissolve in the microgalvanic cell [13, 15]. Kairo et al. [18] investigated the microstructure of grain boundaries in an underaged, Cu rich AlMgSi sheet. They found a 2 nm thick Cu layer along the grain boundaries and an adjacent PFZ consisting of almost pure aluminum. The continuous, Cu rich film provides a continuous path for propagation of IGC along the grain boundaries. Recent research [19] has found that the presence of the Cu rich film is crucial for extensive IGC to occur. Moreover, the discrete Q particles on the grain boundaries were found to act as barriers to IGC and not as local cathodes, and in the absence of the continuous, Cu rich film the particles arrested the corrosion front [19]. It is claimed that AlMgSi alloys with Cu content exceeding 0.1 wt% are susceptible to IGC [18, 19]. Nevertheless, the critical Cu content required to cause IGC is governed by the Mg/Si ratio and thermomechanical treatment [13, 14].

In Cu free AlMgSi alloys with Si in excess of the Mg_2Si stoichiometry, elemental Si plates have been claimed to act as local cathodes which could cause IGC [90]. However, other researchers claim that Si plates are inert in contact with water due to formation of an insulating layer of SiO_2, and hence could not serve as cathodes [12, 13]. Cu free AlMgSi alloys with Mg/Si ratio down to 0.63 have been shown to be only slightly susceptible to

superficial localized IGC [23]. Nevertheless, external cathodes like oxygen in the bulk solution or Fe rich primary phases on the surface have been found to cause IGC in Cu free AlMgSi alloys. However, since the ohmic resistance increases as the corrosion attacks propagate further into the material, these external cathodes are not as effective as internal cathodes to cause deep-penetrating IGC [23].

Despite somewhat contradictory research on the effect of Mg/Si ratio on IGC in Cu free AlMgSi alloys, the Mg/Si ratio has been found to affect the corrosion properties of Cu containing AlMgSi alloys. Whether the alloys are rich in Si or Mg will have an impact on the severity of IGC. Liang et al. [12] have studied the influence of Mg/Si ratio on the corrosion properties of AlMgSi(Cu) alloys. The results demonstrated that artificially aged, Cu containing alloys rich in Mg were more corrosion resistant than those rich in Si. Holmestad et al. [92] studied the grain boundaries in AlMgSi(Cu) alloys with Mg/Si ratio exceeding 2, and found a continuous film along the grain boundaries consisting of both Cu and Mg. Considering that Mg is anodic with regard to the aluminum matrix, the presence of Mg may reduce the cathodic behavior of the film and in turn reduce the IGC susceptibility. No layer of Si was found in neither of the alloy compositions investigated [92].

Effect of cooling rate and ageing time on IGC

Whether AlMgSi alloys are susceptible to IGC and to what extent are highly dependent on the thermomechanical treatment of the alloys. The corrosion behavior of AlMgSi alloys changes with ageing time because the microstructure of the precipitates is altered during ageing [24]. Svenningsen et al. [13] have done a comprehensive study on the effect of artificial ageing on IGC of AlMgSi model alloys with 0.13 wt% Cu. They found that a continuous, Cu rich film was formed along the grain boundaries during air cooling after extrusion, which made air cooled specimens susceptible to IGC in T4 temper. However, the film coarsened and formed discontinuous patches of film during artificial ageing. This arrested the corrosion front and prevented it from further propagation. They also discovered a transition from uniform to localized IGC due to film coarsening. The process is illustrated in Figure 2.10. At longer ageing times to overaged temper, coarsening of matrix precipitates resulted in pitting corrosion [13].

The effect of water quenching after extrusion was also investigated by Svenningsen et al. [14]. Water quenching prevented precipitation of intermetallic phases during cooling, including the Cu rich film. Thus, the water quenched specimens were resistant to IGC in T4 temper. However, artificial ageing introduced slightly susceptibility to IGC due to diffusion of intermetallic phases at elevated temperature and formation of the Cu rich film. In conclusion, water quenched specimens became most susceptible to IGC upon ageing, whereas the IGC susceptibility of air cooled specimens was at a minimum at peak ageing, according to Svenningsen et al. [13, 14]. Several other researchers have concluded that AlMgSi alloys, water quenched after SHT, are most susceptible to IGC in peak aged temper [93–96]. On the contrary, Larsen et al. [15] found that water quenched AlMgSi alloys were less susceptible to IGC after ageing to peak hardness. Nevertheless, it is evident that caution must be taken during thermomechanical processing of a given AlMgSi alloy to ensure minimal susceptibility to IGC combined with optimal mechanical properties.

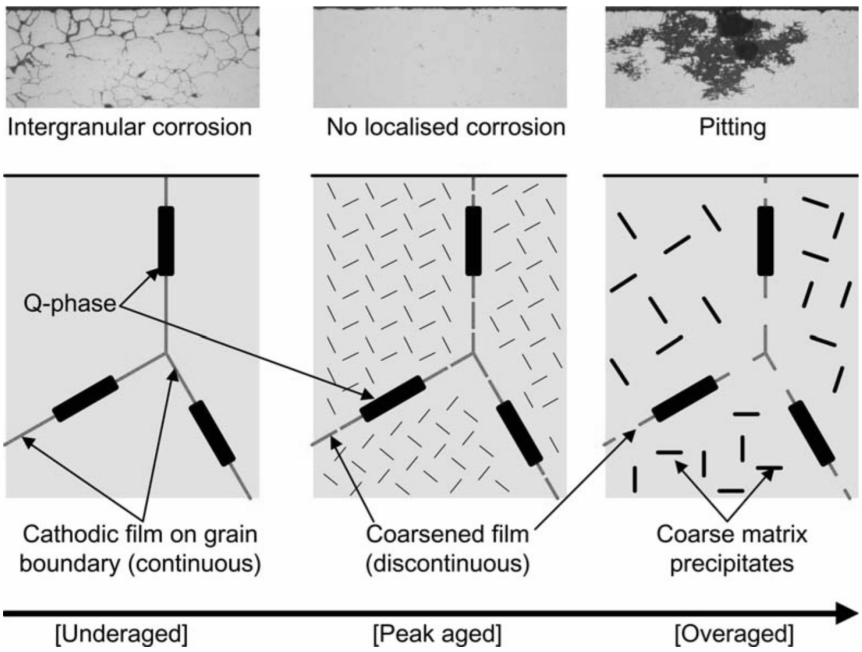

Figure 2.10: Illustration of the effect of ageing time on microstructure of precipitates and corrosion mode of an air cooled AlMgSi(Cu) model alloy [13].

Effect of deformation on IGC

Limited research exists on the effect of deformation on the IGC susceptibility of AlMgSi alloys. Nevertheless, it is documented that pre-deformation affects the precipitation process during subsequent ageing [25, 26, 77, 81, 82], as elaborated in section 2.4.3. Moreover, microstructural changes occur in a material that is deformed, due to the applied stress and formation of dislocations [24, 78]. Hence, it is likely that deformation also affects the corrosion properties of AlMgSi alloys.

Precipitation of solute atoms on dislocations during ageing of pre-deformed materials is believed to affect the corrosion properties, considering that the precipitates are highly decisive regarding the corrosion properties of AlMgSi alloys [13, 16]. Furthermore, research has been conducted on how low and high angle grain boundaries affect the corrosion properties of AA6061 [11], as mentioned in section 2.3.2. It was suggested that precipitates and PFZs easily formed along random HAGBs, but not along LAGBs. HAGBs are found in the recrystallized surface layer of AlMgSi extrusions and sheets. However, sufficiently large deformation is believed to increase the amount of LAGBs at the surface and reduce the amount of HAGBs, and thus reduce the susceptibility to IGC. The research of Yang et al. [27] which documented that Cu free pre-β''/β'' precipitated on LAGBs and Cu containing Q′/Q phases precipitated on HAGBs, making HAGBs more susceptible to corrosion, also argues for the favorable effect of attaining more LAGBs in the material.

Some modest studies have been performed on the influence of pre-deformation on IGC performance of AlMgSi alloys. Larsen et al. [20] found that the IGC resistance was increased in underaged temper as a consequence of 20% pre-deformation of both air cooled

and water quenched AlMgSi alloys containing 0.18 wt% Cu. In peak aged temper both undeformed and pre-deformed specimens were quite resistant to IGC. Davydov et al. [97] studied how SHT, stretching and subsequent long, low temperature ageing treatment affected the corrosion behavior of different AlMgSi alloys containing Cu. They claimed that the susceptibility to IGC was reduced with this treatment, compared to undeformed alloys aged to T6 temper. The width of the PFZ was found to be narrower in the stretched specimens [97].

2.5.2 Pitting corrosion

Above a certain potential, the critical pitting potential (E_c), and in the presence of aggressive anions such as chlorides, aluminum may corrode due to rupture of the protective oxide film at small areas that exposes unprotected metal to aggressive conditions. This localized form of corrosion is termed pitting and appears as small pits in the surface with varying depth and width depending on alloy composition and quality of the oxide film [17]. The value of E_c is among others determined by the alloying elements. For AlMgSi(Cu) alloys, Si and Cu lead to more positive E_c as these elements are more noble than aluminum. On the other hand, Mg lowers E_c [98].

The mechanism of pit initiation is not well established in the literature [98]. Nevertheless, it is generally accepted that pitting occurs in microscopic heterogeneities on the metal surface, for example precipitates, dislocations or scratches [99]. The aggressive ions break down the oxide film and attack the underlying metal [17, 85]. Aggressive conditions are produced inside the pit as a consequence of how the electrochemical reactions proceed, which successively increases the rate of pit propagation. To repassivate the metal, the potential must be lowered to a certain value [98].

Studies have shown that pitting occurs in AlMgSi alloys in overaged temper due to coarsening of matrix precipitates [13, 91, 93–95]. This results in a more uniform distribution of cathodes on the surface, not limiting the local cathodes to the grain boundaries. Moreover, coarsening of precipitates gives rise to depletion of alloying elements in solid solution in the aluminum matrix. Hence, the electrochemical potential difference between the precipitates and matrix increases, while the electrochemical potential difference between the PFZ and matrix decreases. As a consequence, the driving force for pitting is increased, while it is reduced for IGC [13, 15].

Fe and Cu have been found to adversely influence the pitting resistance of AlMgSi alloys, as intermetallic phases containing Fe or Cu on the metal surface behave as cathodes that promote high rates of reduction reactions, resulting in anodic dissolution of the surrounding aluminum matrix [17, 100].

Chapter 3

Experimental

3.1 Materials

Four different AlMgSi alloys were studied in this work. The alloys and their chemical composition are given in Table 3.1. 6005.40 and C28 are extruded profiles, whereas the 6016 alloys are rolled sheets. The corrosion properties of C28 were assessed in a specialization project conducted by the author during fall 2016 [28], but are further investigated in this work. The most essential results from the previous work are presented in Appendix A.

Table 3.1: Chemical composition of examined alloys in wt%. The balance is Al.

Alloy	Si	Fe	Cu	Mn	Mg	Zn	Ti	Cr
6005.40	0.62	0.19	0.15	0.16	0.56	0.00	0.00	0.00
C28	0.72	0.20	0.20	0.51	0.83	0.00	0.03	0.16
6016 A	1.49	0.19	0.0023	0.078	0.38	0.0042	0.019	0.0006
6016 B	1.33	0.20	0.010	0.064	0.30	0.0079	0.019	0.0036

6005.40 and C28 contain appreciable amounts of Cu. 6016 A and B are essentially Cu free alloys and they have very similar chemistry, although 6016 A has somewhat higher content of Si and Mg. The effective Mg/Si ratio in the examined alloys is given in Table 3.2. The ratio is calculated by subtracting the amount of Si which is incorporated into particles and dispersoids containing Fe, Mn and Cr. The formula used to calculate the amount of Si which is available for formation of Mg_2Si is shown in Appendix B. C28 contains Mg in excess of the Mg_2Si stoichiometry, in which the Mg/Si ratio equals 1.73. The other alloys contain Si in excess, and it should be noted that both the 6016 alloys contain significantly large excess of Si. Furthermore, the content of dispersoid forming Mn and Cr is low in 6016.

Table 3.2: Effective Mg/Si ratio in examined alloys.

Alloy	Effective Mg/Si-ratio
6005.40	1.11
C28	1.93
6016 A	0.271
6016 B	0.242

3.2 Thermomechanical processing

The alloys were subjected to different thermomechanical treatments. Cold deformation by rolling or stretching before final ageing (T8 temper) or cold deformation by rolling or stretching after final ageing (T9 temper) was performed. The former is hereafter referred to as pre-deformation, whereas the latter is referred to as post-deformation. It should be noted that post-deformation in this manner not is common in manufacturing of commercial aluminum alloys. Cold deformation was performed parallel to the metal working direction, that is in the extrusion or rolling direction. The degree of rolling was determined by measuring the reduction of the material thickness, while the degree of stretching was determined by measuring the increase of the material length. Samples were cut from material subjected to these treatments and used for hardness measurements, IGC testing and microstructure characterization in electron microscope. In the following sections the specific thermomechanical treatment of each alloy is detailed. Stress-strain curves recorded during pre- and post-stretching are displayed in Appendix C.

6005.40

The 6005.40 alloy melt was cast into billets of 272 mm in diameter and 575-580 mm in length at Hydro Karmøy. Homogenization was successively performed with a heating rate of 87°C/h up to 585°C, where the billet was held for 2 h and 30 min. The cooling rate was only measured at the fans. Subsequently, extrusion into a flat bar was performed in a 3500 tons extrusion press. The bar had a cross section of 150 x 3.9 mm and was cooled by water spraying at the die exit. After cooling the profile was stretched 0.4-0.5% and cut into 2 m lengths. Finally, the profile was stored at room temperature for 2 h after extrusion before it was aged at 185°C for 5 h to T5 temper. This procedure was conducted at Hydro Karmøy.

The received 6005.40 alloy was accordingly in T5 temper, and it was therefore SHT at 540°C for 30 min in Nabertherm N15/65HA air circulation furnace, prior to further thermomechanical processing. Schematic illustrations of the thermomechanical history are shown in Figure 3.1. Immediately after SHT the alloy was water quenched to room temperature and stored in freezer at about -18°C.

Either pre-deformation by rolling or stretching or post-deformation by rolling or stretching was performed on 6005.40. The alloy was pre- or post-deformed 1, 5 and 10% and aged at 185°C for 5 h to T6 temper in Nabertherm N15/65HA regardless of type of deformation, that is either before or after deformation. A heating rate of 200°C/h was used and the alloy was air cooled after ageing. The pre-deformed samples were held at room temperature for 45 min during deformation before ageing. Undeformed samples were included to have a basis of comparison.

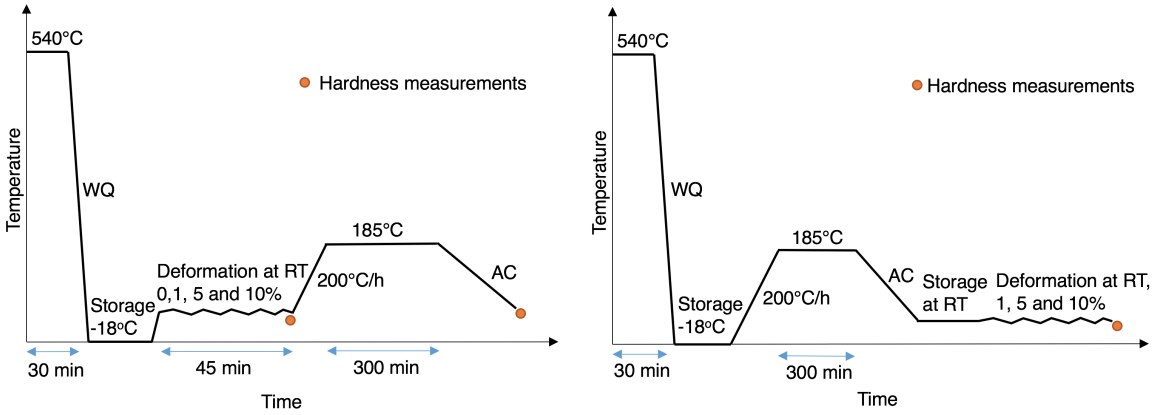

(a) Pre-deformation. **(b)** Post-deformation.

Figure 3.1: Thermomechanical history of 6005.40. The alloy was either pre- or post-deformed by rolling or stretching 0, 1, 5 and 10%. WQ = water quenching, AC = air cooling, RT = room temperature.

C28

The C28 alloy melt was cast into billets of 95 mm in diameter and length up to 1.75 m at Hydro Sunndalsøra, Research and Development center. Homogenization at 575°C for 2 h was subsequently performed with heating and cooling rate of 200°C/h and 400°C/h, respectively. In SINTEF's press laboratory at NTNU, the billet was heated to ease plastic deformation and successively extruded into a flat bar of 25 x 3.9 mm in a vertical extrusion press. The profile was water quenched at the die exit in a water filled pipe. The front piece of the profile was cut off due to non-stabilized extrusion parameters and the following section was used in this work.

The effect of pre-deformation on mechanical and corrosion properties of this alloy has been studied in previous work [28]. Thus, only post-deformation was conducted. The thermomechanical history of C28 is displayed in Figure 3.2. Since the alloy was stored at room temperature for some weeks after extrusion, SHT was carried out at 540°C for 30 min in Nabertherm N15/65HA air circulation furnace. The alloy was subsequently water quenched and stored at room temperature for 17 h before ageing to T6 temper at 185°C for 5 h in Nabertherm N15/65HA. After storage at room temperature, the alloy was post-deformed by rolling or stretching 1, 5 and 10%. The post-deformed samples were stored at room temperature between SHT and ageing for the same amount of time as the pre-deformed samples examined in the specialization project, to obtain an appropriate basis of comparison.

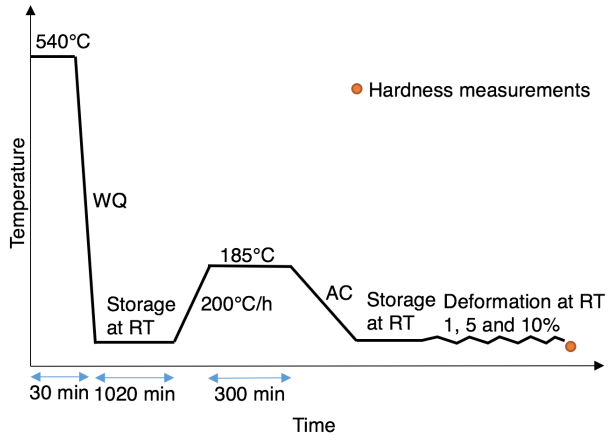

Figure 3.2: Thermomechanical history of C28, post-deformed by rolling or stretching 1, 5 and 10%. WQ = water quenching, AC = air cooling, RT = room temperature.

6016 A and B

The 1 mm thick 6016 sheets were produced in series production and hence follow industrial practice for production of automotive sheets. Therefore, they were surface treated by acid etch cleaning and Ti/Zr passivation. This surface layer was however removed during alkaline etching before IGC testing and should not affect corrosion properties.

The thermomechanical processing of the 6016 alloys is illustrated in Figure 3.3. These alloys were only subjected to pre-deformation by rolling or stretching as ageing occurs after the metal is formed and welded to a body-in-white in the automotive industry, and hence it is not possible to perform deformation by rolling or stretching after ageing. Nevertheless, two different ageing treatments were conducted on the alloys as illustrated in Figure 3.3a and 3.3b.

The ageing treatment in Figure 3.3a was performed to simulate ageing in the automotive industry, and parts of the treatment were carried out at Hydro Rolled Products in Bonn. The sheets were SHT at 560°C for approximately 5 min and subsequently quenched by forced air. Pre-baking, to facilitate precipitation of β'' and accelerate the following age hardening, was performed by heating and coiling the sheets at 90°C for 24 h. These processes were performed in Bonn. The received pre-baked alloys were pre-deformed by rolling or stretching 1, 5 and 10%, and subsequently aged to simulate the paint bake cycle, that is 20 min at 185°C in oil bath. This renders the material in somewhat underaged temper. Samples subjected to this treatment are referred to as paint baked 6016.

The ageing treatment illustrated in Figure 3.3b was equal to the one carried out on 6005.40 to obtain a comparative basis. SHT of pre-baked 6016 for 30 min at 540°C and water quenching were performed prior to pre-deformation by 10% rolling, and finally ageing at 185°C in Nabertherm N15/65HA for 5 h. Samples subjected to this treatment are referred to as T6 tempered 6016. Undeformed samples were included in both ageing treatments for comparison.

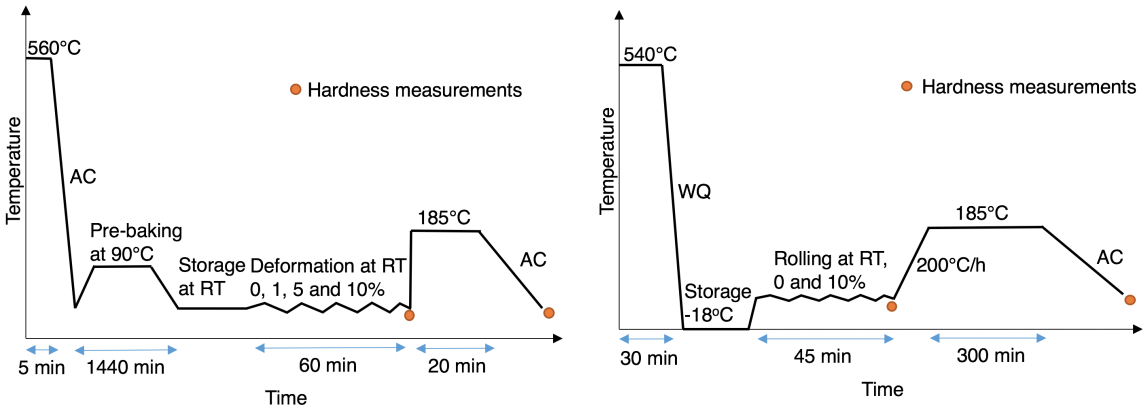

(a) Pre-deformed after pre-baking and aged according to the paint bake cycle.

(b) Pre-deformed after solution heat treatment and aged to T6 temper.

Figure 3.3: Thermomechanical history of the 6016 sheets, pre-deformed by rolling or stretching and subsequently aged by different ageing treatments. WC = water quenching, AC = air cooling, RT = room temperature.

3.3 Microstructure characterization in LM

Imaging in light microscope (LM) was conducted to characterize the microstructure of 6005.40, 6016 A and 6016 B. The aim was to assess the grain size and degree of recrystallization in the different alloys. The microstructure of 6005.40 was investigated in as-received condition, that is T5 temper, and in SHT condition. The 6016 alloys were investigated in pre-baked condition. The microstructure of C28 was examined in the specialization project during fall 2016 [28] and is redisplayed in Appendix A.

3.3.1 Preparation of samples

The samples were mounted in EpoFix Resin and ground for 1-3 min on SiC abrasive papers with increasing degree of fineness (P320, P500, P800 and P1200). Water and soap were used as lubricants. Afterwards, polishing for 3-4 min with diamond paste on MD Largo (9 µm), MD Mol (3 µm) and MD Nap (1 µm) polishing discs was conducted. The force was set to 10 N during polishing. Between each step, the samples were cleaned with water and soap, and then ultrasonically cleaned in ethanol.

When defect free surfaces were obtained, the samples were anodized in order to study them in polarized light. Anodizing was performed by dipping the surface of interest in an electrolyte consisting of 5% HBF_4 with an applied voltage of 20 V for 90 s. Finally, the samples were rinsed in tap water and then ethanol, and dried.

3.3.2 Investigation in LM

Leica MEF4M with Jenoptik Laser Optik System camera was used to study the samples. The cross section parallel to the extrusion or rolling direction was investigated, as illustrated in Figure 3.4. Each alloy was investigated in polarized light with a sub-parallel λ-plate. Micrographs were acquired using the software ProgRes Capture v2.8.8 and approximately grain size was measured.

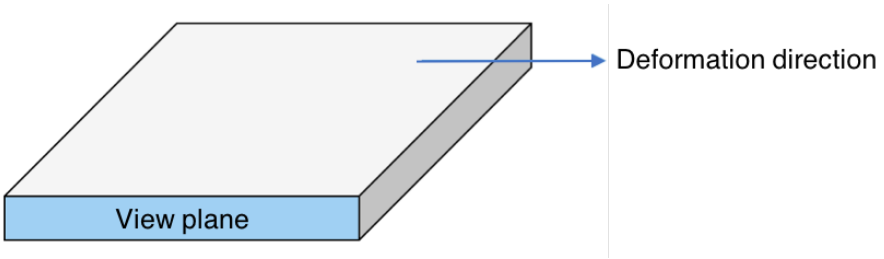

Figure 3.4: Illustration of view plane for microstructure characterization of alloys in light microscope.

3.4 Vickers hardness measurements

Vickers hardness measurements were performed on differently deformed 6005.40, C28, 6016 A and 6016 B during different stages of the thermomechanical treatment, that is before and after ageing for pre-deformed samples and after deformation for post-deformed samples. The measurements are indicated on the schematic illustrations of thermomechanical history of each alloy in Figure 3.1 to 3.3. The aim of the measurements was to examine the effect of deformation and ageing on hardness. Five indentations were made randomly on each sample on the surface indicated in Figure 3.5, in Zwick/Roell indentec with Zwick/Roell ZHμ HD Micro Hardness Software. The load and load time were 1 kg and 15 s for all samples. The surface was not ground before the measurements.

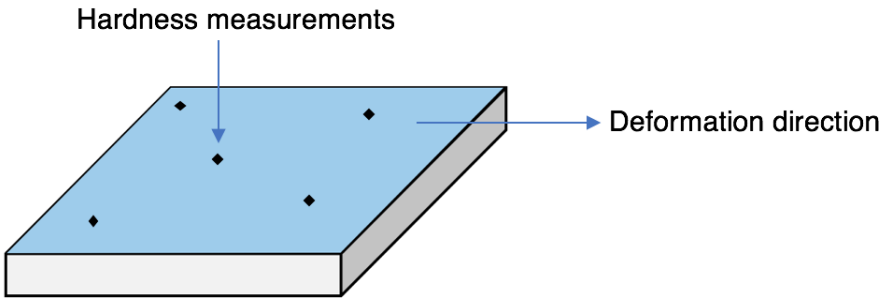

Figure 3.5: Hardness measurements were performed randomly on the surface indicated for each sample.

3.5 Accelerated IGC test

An accelerated IGC test was carried out according to ISO 11846 (method B). This standard states the testing procedure for determining IGC resistance of cast and wrought, solution heat treatable aluminum alloys. Method B is used to compare the resistance of various alloys [88].

The overall aim of performing IGC testing was to assess the effect of deformation on corrosion properties of different AlMgSi alloys. Samples of 6005.40, C28, 6016 A and 6016 B, subjected to the thermomechanical treatments described, were tested. An overview of the different parallels subjected to IGC testing is presented in Table 3.3. The primary varying parameters were whether the tested sample was pre- or post-deformed and whether it was rolled or stretched. 6005.40 and C28 were aged to T6 temper either before or after deformation, whereas the 6016 alloys were aged to either simulate the paint bake cycle (somewhat underaged temper) or aged to T6 temper after deformation. Consequently, all IGC tested samples were artificially aged before testing.

Table 3.3: Overview of samples subjected to intergranular corrosion testing.

	Pre-deformation	**Post-deformation**
Rolling	6005.40	6005.40
	6016 A (paint baked)	C28
	6016 A (T6 tempered)	
	6016 B (paint baked)	
	6016 B (T6 tempered)	
Stretching	6005.40	6005.40
	6016 A (paint baked)	C28
	6016 B (paint baked)	

3.5.1 Surface preparation

The samples subjected to IGC testing were cut into dimensions as specified in Figure 3.6. It should be noted that the standard specifies that the longer dimension of the sample should be parallel to the metal working direction. However, the dimensions given in Figure 3.6a were used during the specialization project due to convenience, and it was chosen to continue using this sample size.

To diminish the heterogeneity due to cutting, the edges of the samples were slightly ground on SiC abrasive paper P500. Prior to the actual testing, the samples were prepared as described in the standard. They were degreased with acetone, and thereafter alkaline etched for about 3 min in 7.5% sodium hydroxide (NaOH) solution, heated to 50-60°C. Roughly 14 μm of the metal surface was removed during etching. The samples were immediately rinsed in running water and then desmutted in 68% nitric acid (HNO_3) for 2 min. Finally, they were rinsed in running water, distilled water and dried, before they were weighted. Two equal samples of each alloy were prepared and IGC tested.

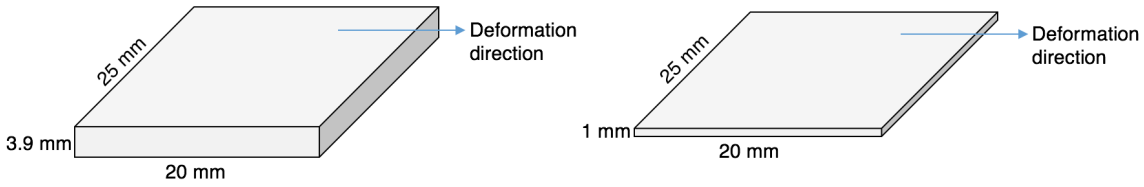

(a) 6005.40 and C28. **(b)** 6016 A and B.

Figure 3.6: Illustrations of dimensions on samples subjected to intergranular corrosion testing.

3.5.2 IGC test execution

IGC testing was performed by immersing the samples in an acidified electrolyte, containing 30 g/L sodium chloride (NaCl) and 10 mL/L 35% hydrochloric acid (HCl) for 24 h. Distilled water was used to prepare the solution. The samples were mounted in fishing line more than 20 mm below the solution level and there was no contact between the samples or the samples and the vessel wall. The ratio of the solution volume to the total sample surface area was kept constant for all tests and was approximately 20 cm^3/cm^2.

After 24 h the samples were rinsed in running water and corrosion products were removed by dipping the samples in 68% HNO_3 for about 2 min, followed by thorough cleaning in running water, distilled water and then drying. Eventually, the samples were weighted in order to calculate weight losses caused by corrosion.

3.5.3 Examination of corrosion in LM

A piece of all corrosion tested samples was cut off, as in accordance to the illustration of view plane in Figure 3.7, to examine the cross section parallel to the deformation direction in LM. Thereafter, the samples were mounted in EpoFix Resin and ground and polished as described in section 3.3.1, apart from anodizing.

The corrosion damages in the IGC tested samples were studied in bright field with the same apparatus as described in section 3.3.2. Maximum corrosion depth and corrosion depth range were measured, and corrosion mode was determined. To document the effect of deformation, micrographs were acquired at magnification 2.5x or 5x of a representative area on the samples and 10x of the most severe corrosion attack. These micrographs were not necessarily taken of the same area on the samples.

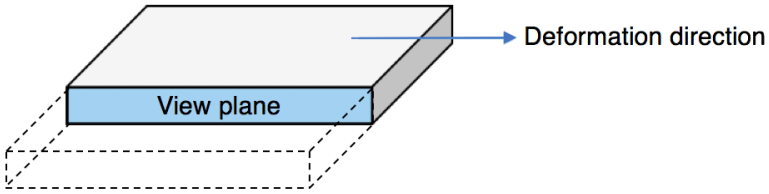

Figure 3.7: Illustration of view plane during examination of intergranular corrosion tested samples in light microscope.

3.6 Microstructure characterization in SEM and TEM

To obtain a better understanding of the corrosion properties of deformed AlMgSi alloys, the uncorroded microstructure of T6 tempered 6005.40 was further examined in scanning electron microscope (SEM) and transmission electron microscope (TEM).

3.6.1 Sample preparation

The view plane during studies in both SEM and TEM is illustrated in Figure 3.8. The surface was prepared as described in the following sections prior to the examinations.

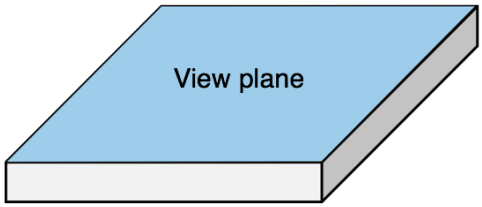

Figure 3.8: Illustration of view plane for microstructure characterization of T6 tempered 6005.40 samples in scanning and transmission electron microscope.

SEM

10% pre-rolled, 10% post-rolled and 10% post-stretched 6005.40 samples, as well as the undeformed sample, were studied in SEM. The examined surface was left unground to ensure examination of the very top surface of the samples and to avoid introducing deformation caused by grinding. Electropolishing was performed in Struers LectroPol-5 directly on the extruded surface. The parameters used during electropolishing are displayed in Table 3.4a. Immediately after electropolishing, the samples were rinsed in water and ethanol.

TEM

Only undeformed and 10% pre-rolled 6005.40 were studied in TEM due to time constraints. A defect free surface was required to achieve images of good quality in the TEM. Hence, the examined surface was firstly ground on SiC abrasive paper P2400 to remove all extrusion die lines. The surface was ground to the minimum and roughly 10-50 μm of the metal was removed in this process. The surface opposite to the examined surface was subsequently mechanically polished on finer and finer SiC abrasive papers to approximately 60-100 μm metal thickness was achieved. Disks of 3 mm in diameter were stamped from the thin metal foil and mounted in the sample holder for electropolishing. Electropolishing was performed in Struers TenuPol-5 and the parameters used are displayed in Table 3.4b. After electropolishing the samples were rinsed in methanol and then ethanol. Just before examinations in TEM the samples were plasma cleaned in Fischione Plasma Cleaner.

Table 3.4: Parameters used during electropolishing for preparation of samples to studies in scanning electron microscope (SEM) and transmission electron microscope (TEM).

(a) Electropolishing in Struers LectroPol-5 for SEM studies.

Parameter	Value
Electrolyte	A2
Temperature	-25 to -30°C
Voltage	28 V
Flow rate	12
Time	30 s

(b) Electropolishing in Struers TenuPol-5 for TEM studies.

Parameter	Value
Electrolyte	2/3 methanol 1/3 nitric acid
Temperature	-25 to -30°C
Voltage	20 V
Flow rate	20
Light stop value	20

3.6.2 Studies in SEM

Backscatter imaging and electron backscatter diffraction (EBSD) of the surface of undeformed and deformed, T6 tempered 6005.40 were performed in Field Emission SEM Zeiss Ultra, 55 Limited Edition. Backscatter images were acquired in backscatter mode to image particles and precipitates in the alloy microstructure. Acceleration voltage of 20 keV, aperture diameter of 60 μm and working distance of about 10 mm were used.

EBSD was performed to obtain knowledge of grain structure and grain boundary misorientation angles. Nordif UF-300 EBSD detector was used to record the diffraction patterns. The samples were tilted to 70°, and acceleration voltage of 20 keV, aperture diameter of 120 μm and working distance of about 24 mm were used. The recorded diffraction patterns were analyzed with OIM Data Collector and OIM Data Analysis.

3.6.3 Studies in TEM

Studies in TEM were performed by Sigurd Wenner[1] with the author as observer on undeformed and 10% pre-rolled, T6 tempered 6005.40 samples. TEM imaging was carried out on JEOL ARM-200F cold field emission gun microscope operated at 200 kV. The aim was to assess differences in the formation of dislocations and precipitates in the samples.

High angle annular dark field scanning TEM (HAADF-STEM) imaging was performed to see precipitate structure details and assess the Cu distribution within the precipitates. For this the JEOL ARM-200F cold field emission gun microscope was used, with probe and image spherical aberration correctors. The acceleration voltage was 200 kV, and the beam current approximately 20 pA. The beam convergence angle was 27 mrad, and the HAADF detector collected electrons scattered between 48 and 206 mrad. This set-up gave a good atomic number contrast while retaining an adequate signal for imaging, and was ideal for discerning Cu from the lighter elements Al, Mg and Si. Both TEM and HAADF-STEM images were acquired at $(001)_{Al}$ zone axis.

Energy dispersive X-ray spectroscopy (EDS) mapping was performed in JEOL 2100F TEM operated in STEM mode at 200 kV. Due to time constraints, only the 10% pre-rolled, T6 tempered 6005.40 sample was analyzed. Composition of a grain boundary and precipitates along the grain boundary, as well as composition of a primary α particle, was determined by EDS mapping using an Oxford Instrument system.

[1] SINTEF, Materials and Chemistry, Trondheim

Chapter 4

Results

4.1 Microstructure characterization in LM

The microstructure of uncorroded 6005.40, 6016 A and 6016 B was investigated in LM to assess the degree of recrystallization and grain size for the different alloys. In Figure 4.1 and 4.2 the microstructure of 6005.40 and 6016 in cross-sectional area, parallel to the extrusion or rolling direction, is presented. The microstructure of C28 is displayed in Appendix A.

Extruded 6005.40 was received in T5 temper and SHT was carried out before deformation and ageing. The microstructure in each temper is shown in Figure 4.1a and 4.1b. No differences in microstructure between the two tempers are visible. The alloy is fully recrystallized and a layer with larger grains is observed at the surface in relation to in the bulk. The grains in this surface layer are in the range of 20-300 μm. The smallest grains exist on the outermost surface.

The rolled 6016 alloys were received in pre-baked condition, which means they were given a short ageing treatment to facilitate ageing in the paint bake cycle. The microstructure of pre-baked 6016 A and 6016 B is presented in Figure 4.2a and 4.2b, respectively. These alloys are fully recrystallized as 6005.40, however the grain size is much smaller and the microstructure seems homogeneous throughout the thickness of the alloys. Moreover, there is a small difference in grain size between the 6016 alloys. The grain size in 6016 A is in the range of 35-45 μm, whereas in 6016 B it is between 50-60 μm.

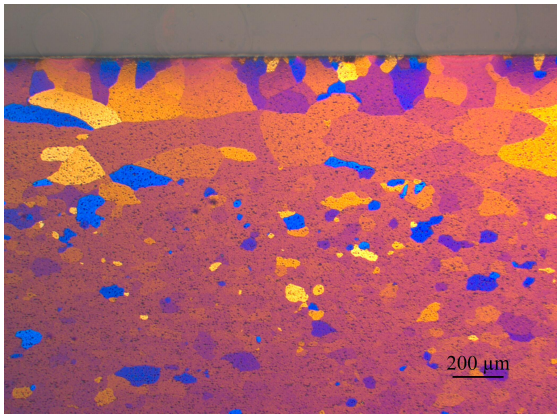

(a) T5 tempered.

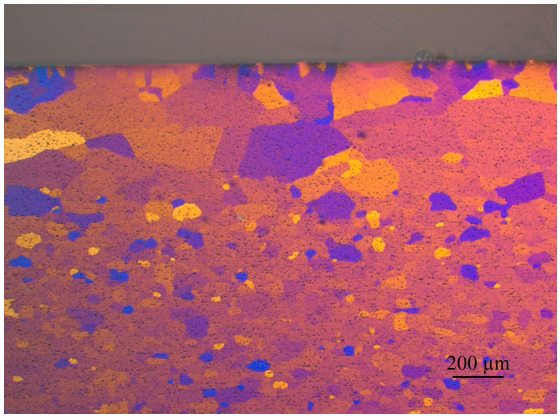

(b) T5 tempered and thereafter solution heat treated.

Figure 4.1: Optical micrographs showing microstructure of 6005.40 in cross-sectional area. The view plane is parallel to the extrusion direction. The scale bar is 200 µm on both micrographs.

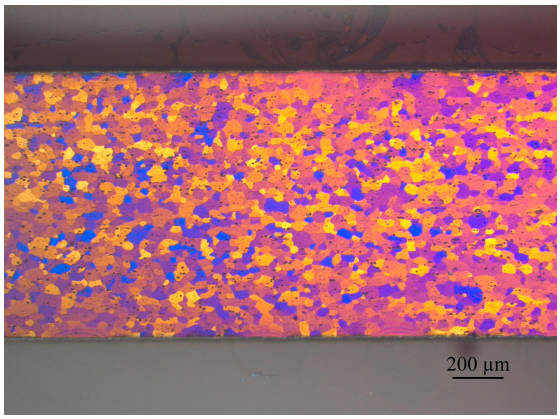

(a) 6016 A.

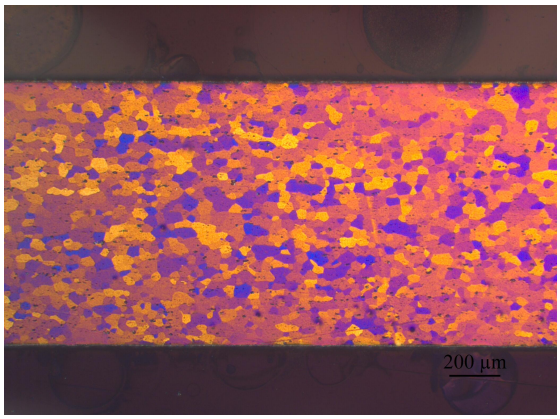

(b) 6016 B.

Figure 4.2: Optical micrographs showing microstructure of pre-baked 6016 A and B in cross-sectional area. The view plane is parallel to the rolling direction. The scale bar is 200 µm on both micrographs.

4.2 Vickers hardness measurements

Vickers hardness measurements (HV1) were performed on 6005.40, 6016 A, 6016 B and C28. To investigate the effect of deformation on hardness, the alloys were deformed by different deformation types and to different degree before the hardness measurements. The pre-deformed samples were measured both before and after ageing treatment to assess the influence of ageing on hardness of pre-deformed materials. Average hardness values and standard deviations for all measurements can be found in Table D.1 to D.4 in Appendix D.

4.2.1 Effect of pre-rolling on hardness

The result of hardness measurements on pre-rolled samples before and after ageing is graphically displayed in Figure 4.3a to 4.3c for 6005.40, 6016 A and 6016 B, respectively. 6005.40 was aged to T6 temper after deformation, whereas 6016 A and B were aged either to simulate the paint bake cycle used in the automotive industry (somewhat underaged temper) or to T6 temper.

Before ageing the overall trend for all alloys is increasing hardness as the degree of pre-rolling increases. Taking standard deviations into consideration, the rise in hardness as a function of pre-rolling is roughly linear. The hardness of 6005.40 increases more than 20 HV from the undeformed to the 10% pre-rolled sample before ageing. Approximately equal rises in hardness are observed for the 6016 alloys.

The effect of pre-deformation on hardness after ageing is rather different for the examined materials. 6005.40 achieves significantly higher hardness after ageing and the hardness is equal for the undeformed and the pre-rolled samples, that is independent of pre-rolling. Paint baked 6016 A and B exhibit slightly increasing hardness as degree of pre-rolling increases also after ageing. The rise in hardness due to ageing is low for these samples. This is evident in Figure 4.3b and 4.3c. On the other hand, 10% pre-rolled, T6 tempered 6016 A and B have somewhat lower hardness than the corresponding undeformed samples after ageing, but the rise in hardness due to ageing is large.

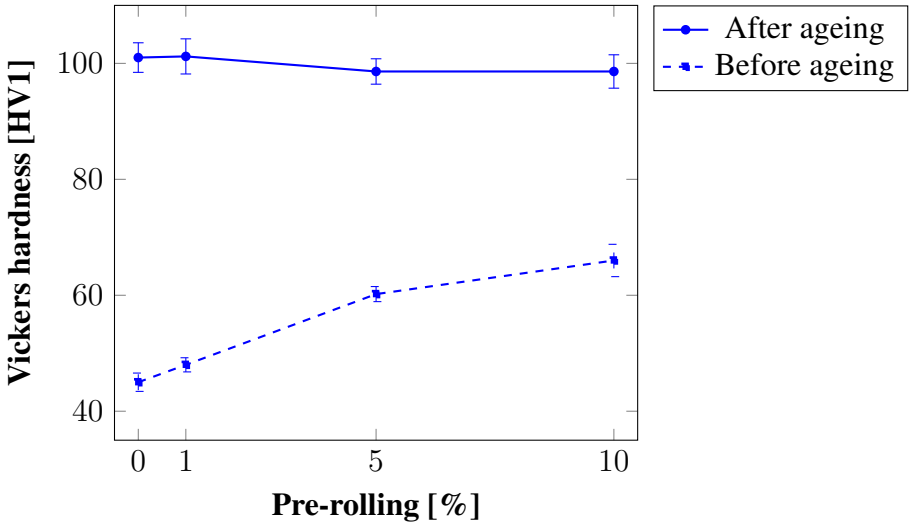

(a) 6005.40.

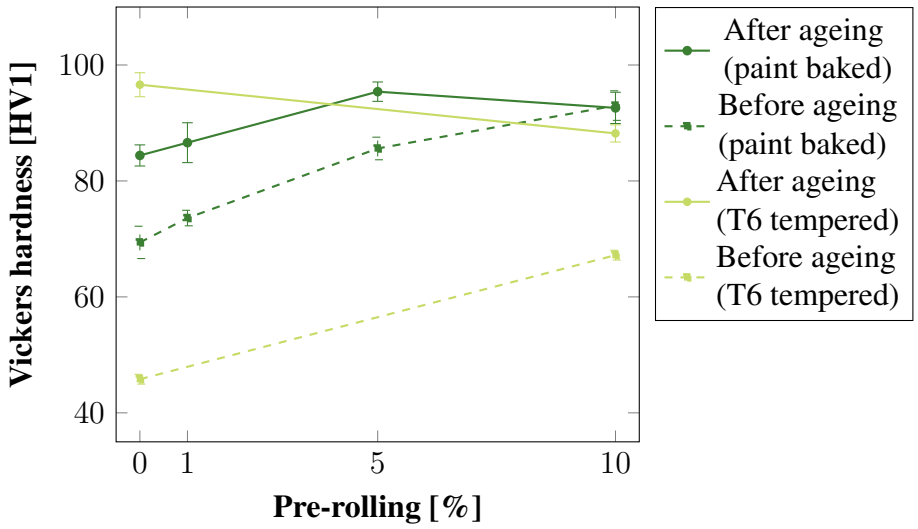

(b) 6016 A.

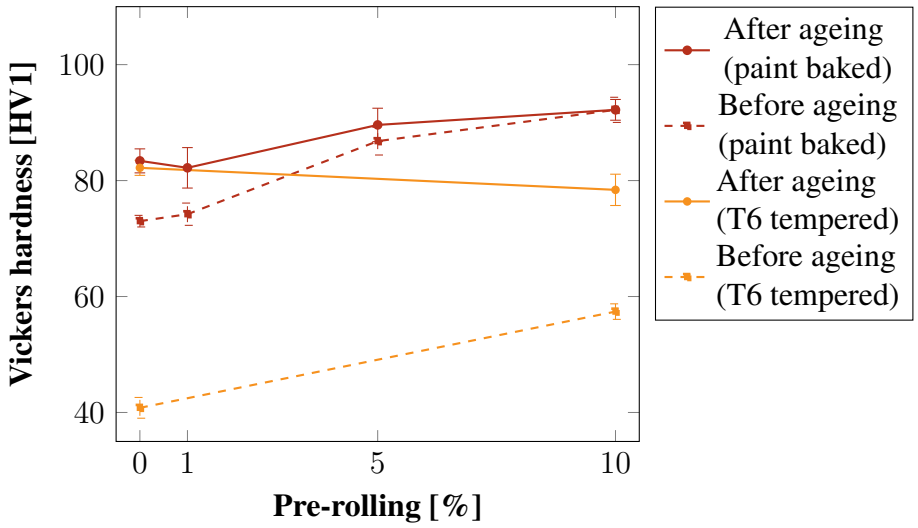

(c) 6016 B.

Figure 4.3: Vickers hardness measurements (HV1) before and after ageing of 6005.40, 6016 A and 6016 B, pre-rolled to different degree. 6005.40 was aged to T6 temper, whereas the 6016 alloys were aged either to simulate the paint bake cycle or to T6 temper.

4.2.2 Effect of pre-stretching on hardness

In Figure 4.4a to 4.4c hardness before and after ageing of pre-stretched 6005.40, 6016 A and 6016 B is displayed. The pre-stretched 6016 alloys were only aged to simulate the paint bake cycle, not T6 tempered.

All samples exhibit increasing hardness before ageing as a function of increasing degree of pre-stretching, although the measured hardness of undeformed 6005.40 is slightly larger

than the one measured for 1% pre-stretched 6005.40. It was generally measured higher hardness values for the pre-rolled samples compared to the pre-stretched samples before ageing.

The hardness of pre-stretched 6005.40 after ageing is equivalent to the hardness of pre-rolled 6005.40 after ageing and independent of degree of stretching, as seen in Figure 4.4a. Pre-stretched 6016 A and B exhibit slightly increasing hardness after ageing due to increasing %CW, but the increase is definitely minor. This result corresponds with the result obtained for the pre-rolled, paint baked 6016 samples, although the hardness was measured to be somewhat larger for the pre-rolled samples compared to the pre-stretched samples.

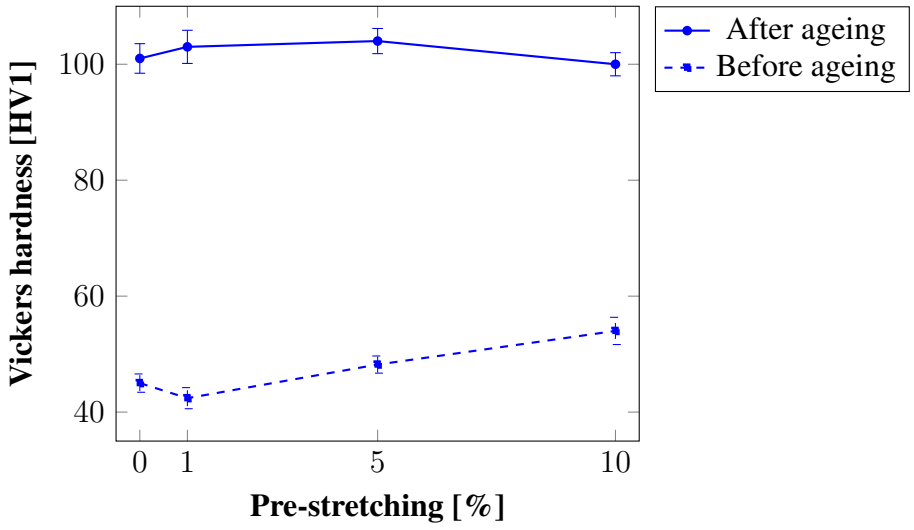

(a) 6005.40.

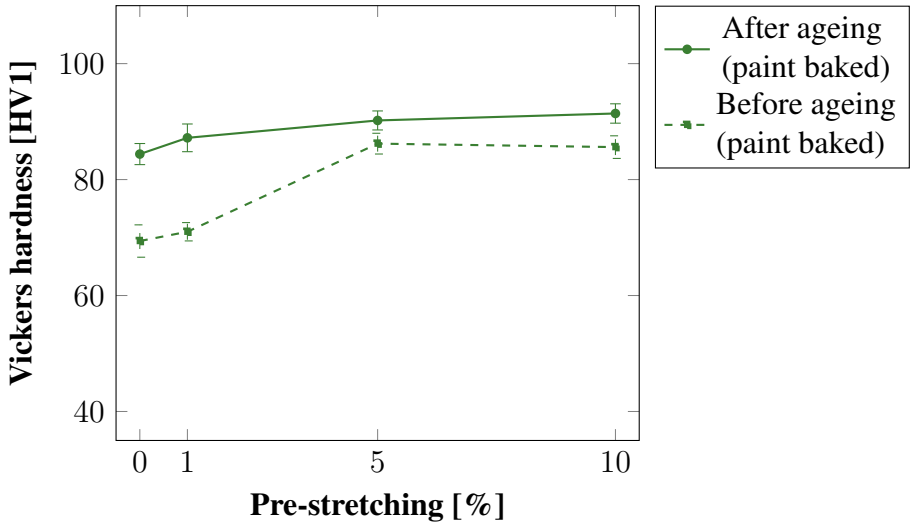

(b) 6016 A.

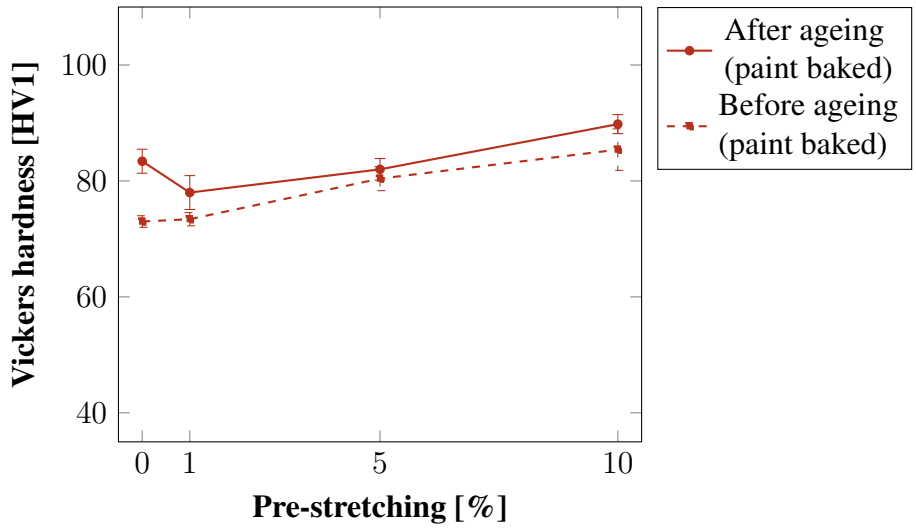

(c) 6016 B.

Figure 4.4: Vickers hardness measurements (HV1) before and after ageing of 6005.40, 6016 A and 6016 B, pre-stretched to different degree. 6005.40 was aged to T6 temper, whereas the 6016 alloys were aged to simulate the paint bake cycle.

4.2.3 Effect of post-rolling on hardness

The effect of post-rolling on hardness was investigated for 6005.40 and C28. The result of the measurements is displayed in Figure 4.5. No obviously trend in the effect of post-rolling on hardness is observed. Taking standard deviations into consideration, the hardness of undeformed and post-rolled samples is quite similar for both alloys. However, the hardness is slightly increasing for C28 as %CW increases from 1 to 10%. The hardness of post-rolled 6005.40 is rather close to the hardness obtained after ageing of pre-rolled and pre-stretched 6005.40, which was in the order of 100 HV.

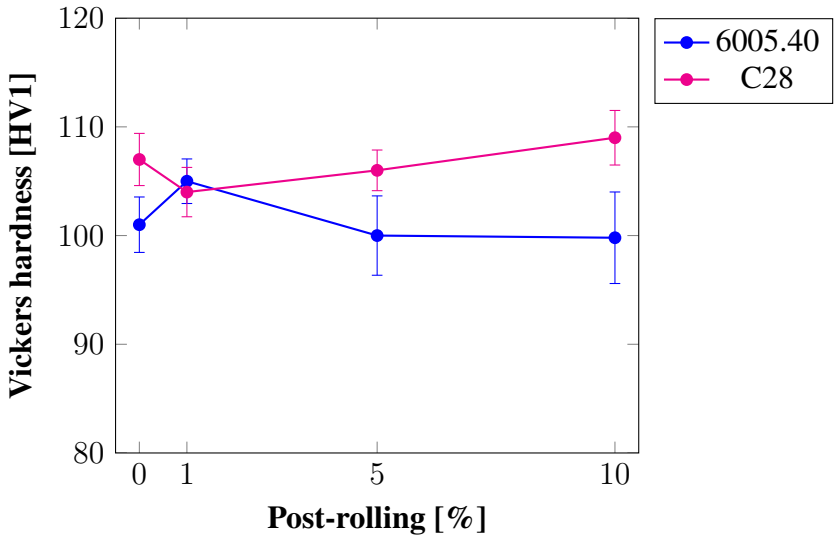

Figure 4.5: Vickers hardness measurements (HV1) on 6005.40 and C28, post-rolled to different degree after ageing to T6 temper.

4.2.4 Effect of post-stretching on hardness

The result of hardness measurements on post-stretched 6005.40 and C28 is displayed in Figure 4.6. The general trend is slightly increasing hardness as a function of increasing degree of post-stretching, although the difference in hardness between 0 or 1% and 10% post-stretched samples is only about 8 HV for both alloys. Furthermore, the hardness of post-stretched samples is generally higher than the hardness of post-rolled samples for both 6005.40 and C28.

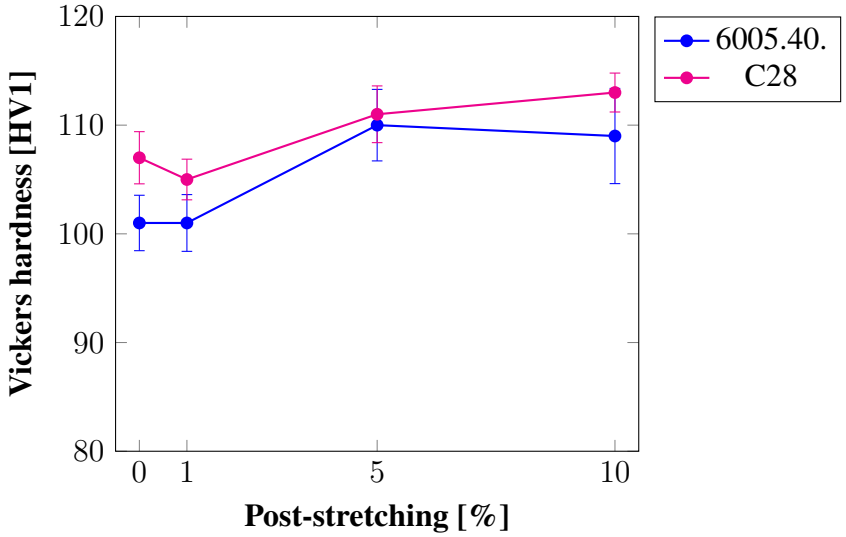

Figure 4.6: Vickers hardness measurements (HV1) on 6005.40 and C28, post-stretched to different degree after ageing to T6 temper.

4.3 Accelerated IGC testing

6005.40, 6016 A, 6016 B and C28, deformed to various degree by different deformation types, were subjected to an accelerated IGC test according to ISO 11846 (method B), a 24 h immersion test. Both pre-deformed and post-deformed samples by rolling or stretching were tested and an overview of the different parallels is displayed in Table 3.3 in section 3.5. The alloys were aged prior to IGC testing regardless of deformation type. 6005.40 and C28 were aged to T6 temper, whereas 6016 A and B were aged to either simulate the paint bake cycle, that is somewhat underaged temper, or aged to T6 temper.

Subsequent to testing, metallographic examinations in LM of cross-sectional area parallel to the metal working direction were performed in order to quantitatively assess the corrosion damages. The aim was to examine how pre- and post-deformation by rolling or stretching affect the alloys' susceptibility to corrosion. Optical micrographs were acquired at low magnification of representative areas on the samples to study the effect of deformation. In addition, the most severe corrosion attacks were imaged at higher magnification. Micrographs at low and high magnification were not necessarily taken at the same area on the samples. The corrosion damages were classified into different categories indicating the extent of corrosion (uniform or local) and type of corrosion (IGC, pitting and/or etching). Moreover, maximum corrosion depth, corrosion depth range and weight loss were measured for each sample. These results are summarized in a table for each alloy.

4.3.1 Effect of pre-deformation on IGC

The effect of deformation before the final ageing treatment on IGC susceptibility is presented for 6005.40, 6016 A and 6016 B in the following sections.

Pre-rolling of 6005.40

Micrographs of 6005.40, undeformed and pre-rolled to different levels, are displayed in Figure 4.7. The corrosion parameters are summarized in Table 4.1. It can be observed in Figure 4.7a and 4.7b that the undeformed sample exhibits uniform IGC, characterized by narrow and knife-edge sharp attacks along the grain boundaries. A surface layer of about 200 μm is partially detached from the material due to IGC. In quite a few areas the IGC front has propagated further into the material below this surface layer, resulting in extensive corrosion. This result is supported by the data in Table 4.1, which indicate large weight loss and profound maximum corrosion attack. The 1% pre-rolled sample also exhibits uniform and profound IGC.

The corrosion damages are strikingly reduced in the 5 and 10% pre-rolled samples in relation to the less deformed samples, as indicated by the micrographs in Figure 4.7e to 4.7h. The corrosion attacks are confined to local and shallower corrosion, initiated in discrete sites. Pitting, which is characterized by wider and more localized attacks in the grains, is observed along with IGC in the 5 and 10% pre-rolled samples.

Table 4.1: Corrosion parameters after intergranular corrosion testing of pre-rolled and subsequently T6 tempered 6005.40.

Deformation	**Corrosion mode**	**Max. corrosion depth [µm]**	**Weight loss [mg/cm^2]**
0%	Uniform IGC (200-430 µm)	529	7.75
1%	Uniform IGC (200-430 µm)	644	6.56
5%	Local IGC and pitting (180 µm)	206	3.20
10%	Local IGC and pitting (180 µm)	205	3.93

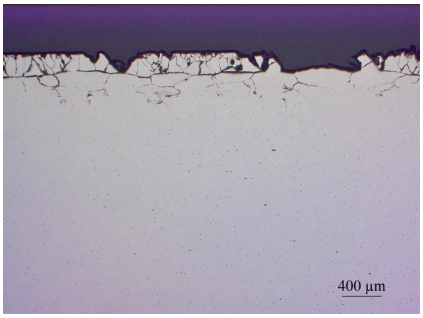

(a) Undeformed.

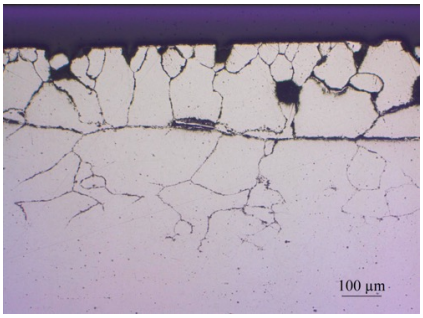

(b) Undeformed.

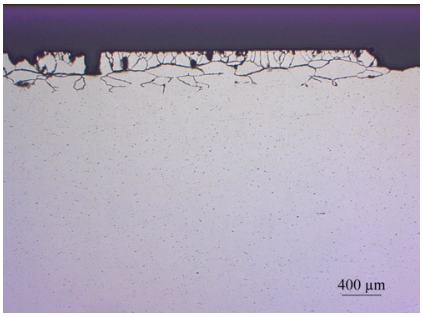

(c) 1% pre-rolled.

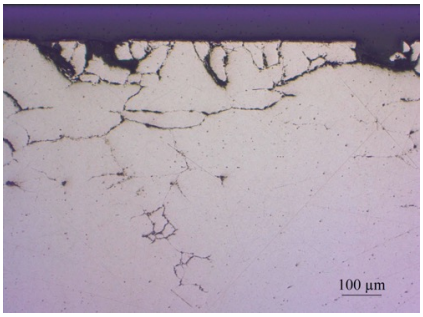

(d) 1% pre-rolled.

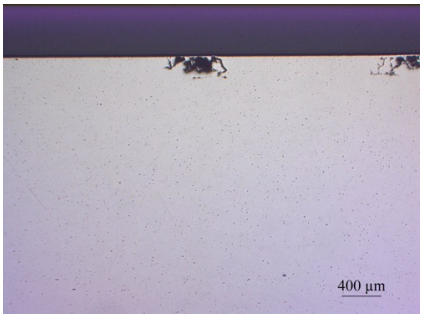

(e) 5% pre-rolled.

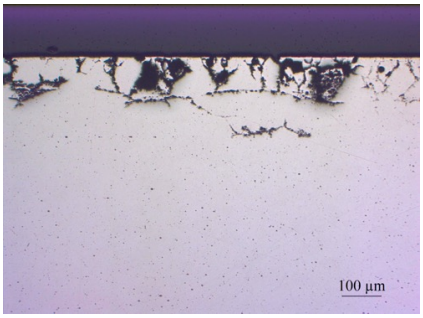

(f) 5% pre-rolled.

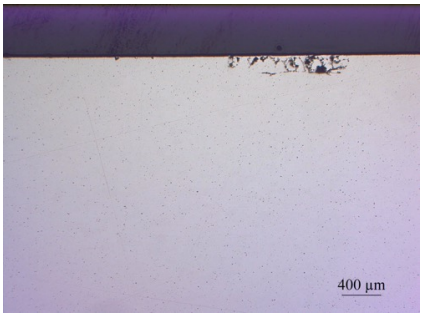

(g) 10% pre-rolled.

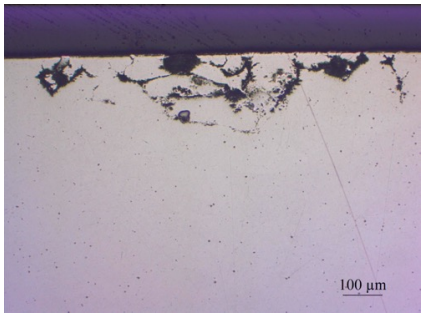

(h) 10% pre-rolled.

Figure 4.7: Optical micrographs of cross section parallel to extrusion direction of pre-rolled, subsequently T6 tempered and corrosion tested 6005.40. Figure (a), (c), (e) and (g) show corrosion attacks in representative areas. Figure (b), (d), (f) and (h) show the most severe attacks.

Pre-stretching of 6005.40

The micrographs of pre-stretched 6005.40 are shown in Figure 4.8 and the corrosion parameters are summarized in Table 4.2. The 1% pre-stretched sample exhibits localized IGC, though with quite a few initiation sites. The weight loss is considerably lower for the 1% pre-stretched sample in relation to the undeformed and the 1% pre-rolled sample. Furthermore, the corrosion depth is lower.

The corrosion attacks are further confined in the 5 and 10% pre-stretched samples, and pitting is observed along with IGC, as can be seen in Figure 4.8e to 4.8h. Micrographs and corrosion parameters indicate in summary that pre-deformation, either by rolling or stretching, is beneficial in reducing the susceptibility of 6005.40 to IGC.

Table 4.2: Corrosion parameters after intergranular corrosion testing of pre-stretched and subsequently T6 tempered 6005.40.

Deformation	**Corrosion mode**	**Max. corrosion depth [µm]**	**Weight loss [mg/cm^2]**
0%	Uniform IGC (200-430 µm)	529	7.75
1%	Local IGC (200-330 µm)	424	3.29
5%	Local IGC and pitting (235 µm)	371	2.29
10%	Local IGC and pitting (210 µm)	330	2.53

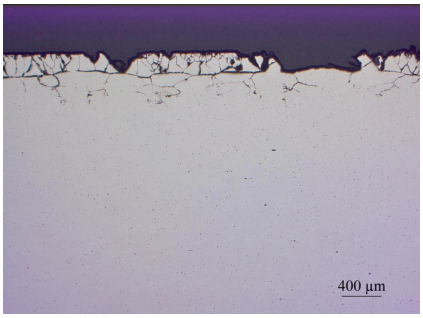

(a) Undeformed.

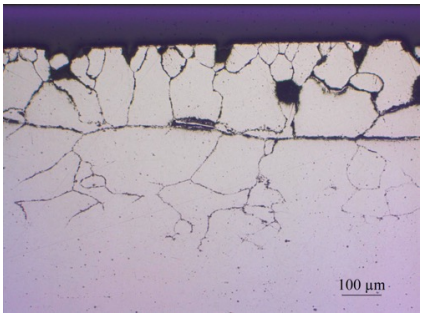

(b) Undeformed.

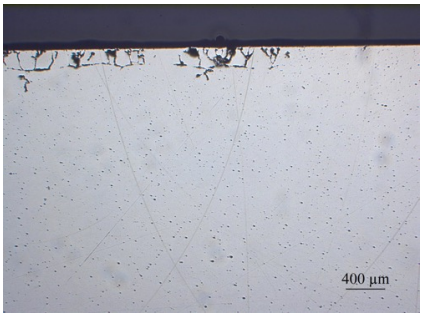

(c) 1% pre-stretched.

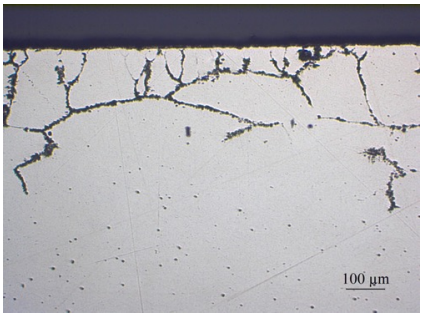

(d) 1% pre-stretched.

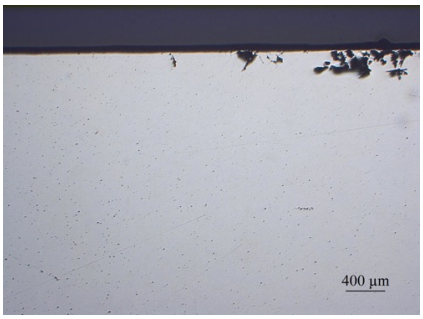

(e) 5% pre-stretched.

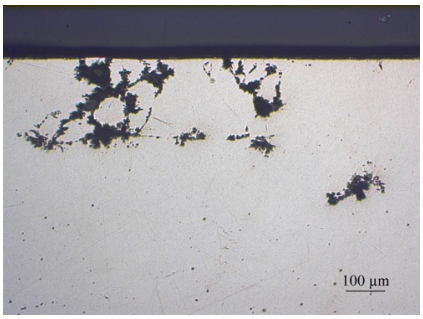

(f) 5% pre-stretched.

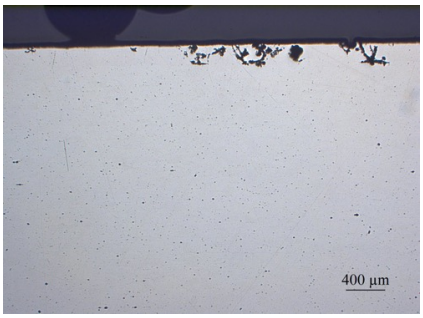

(g) 10% pre-stretched.

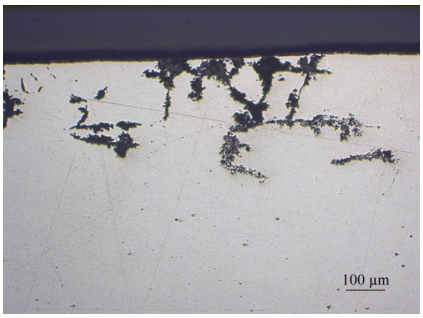

(h) 10% pre-stretched.

Figure 4.8: Optical micrographs of cross section parallel to extrusion direction of pre-stretched, subsequently T6 tempered and corrosion tested 6005.40. Figure (a), (c), (e) and (g) show corrosion attacks in representative areas. Figure (b), (d), (f) and (h) show the most severe attacks.

Pre-rolling of 6016 A, paint baked

Micrographs of paint baked 6016 A, which was pre-rolled to different degree after pre-baking, are displayed in Figure 4.9. The corrosion parameters are summarized in Table 4.3. The undeformed sample exhibits shallow, local IGC, although the high number of initiation sites results in almost uniform IGC. Both the maximum corrosion depth and the weight loss are rather low. The corrosion damages in the 1% pre-rolled sample are very similar to the undeformed sample and the maximum corrosion depth is even lower in this sample. However, the weight loss is larger for the 1% pre-rolled sample.

As the degree of pre-rolling is increased to 5 and 10%, the IGC resistance of paint baked 6016 A decreases. This can be observed in Figure 4.9e to 4.9h and Table 4.3. The number of initiation sites increases, causing uniform IGC. Moreover, the corrosion depths are larger than for the less deformed samples, and largest for the 10% pre-rolled sample.

Table 4.3: Corrosion parameters after intergranular corrosion testing of pre-rolled and subsequently paint baked 6016 A.

Deformation	**Corrosion mode**	**Max. corrosion depth [μm]**	**Weight loss [mg/cm^2]**
0%	Local IGC (20-80 μm)	147	2.38
1%	Local IGC (20-70 μm)	106	3.50
5%	Uniform IGC (20-130 μm)	248	3.30
10%	Uniform IGC (20-140 μm)	292	4.93

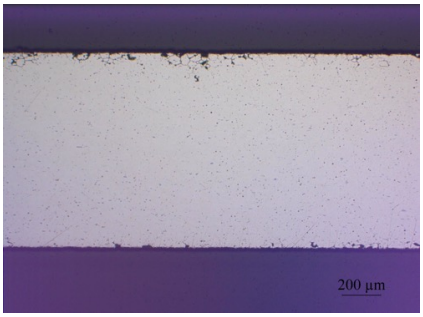

(a) Undeformed.

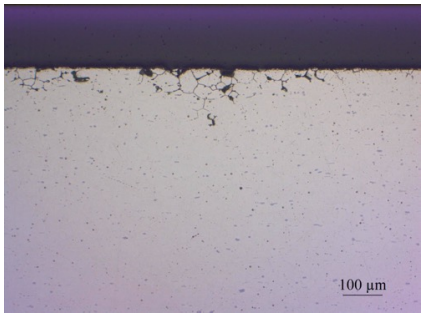

(b) Undeformed.

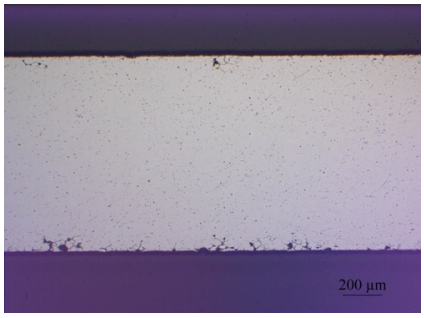

(c) 1% pre-rolled.

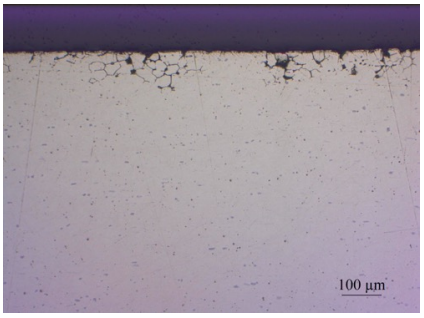

(d) 1% pre-rolled.

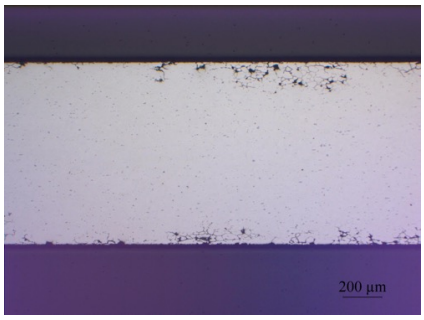

(e) 5% pre-rolled.

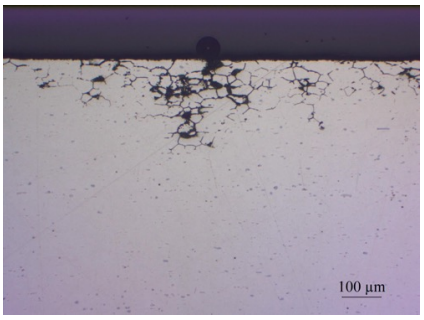

(f) 5% pre-rolled.

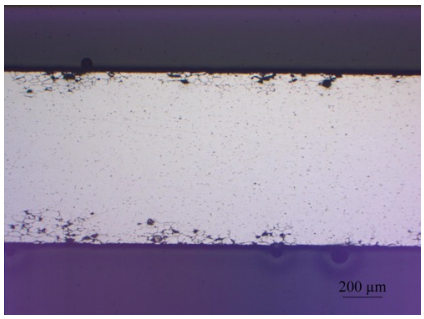

(g) 10% pre-rolled.

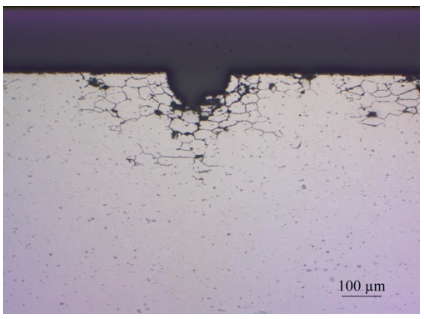

(h) 10% pre-rolled.

Figure 4.9: Optical micrographs of cross section parallel to rolling direction of pre-rolled, subsequently paint baked and corrosion tested 6016 A. Figure (a), (c), (e) and (g) show corrosion attacks in representative areas. Figure (b), (d), (f) and (h) show the most severe attacks. The scale bar is 200 µm in Figure (a), (c), (e) and (g).

Pre-stretching of 6016 A, paint baked

Micrographs of pre-baked, pre-stretched and subsequently paint baked 6016 A are presented in Figure 4.10 and the corrosion parameters are summarized in Table 4.4. An increase in IGC susceptibility as a consequence of increasing pre-stretching is evident from measurements of corrosion depths and weight losses, as well as the optical micrographs. All the pre-stretched samples exhibit uniform IGC, but the most extensive IGC attacks are observed in the 10% pre-stretched sample. This can be seen in Figure 4.10g and 4.10h. Hence, it is apparent that pre-stretching has adversely impact on the corrosion resistance of paint baked 6016 A,

and micrographs and weight loss measurements indicate that pre-stretching causes more susceptible samples in relation to pre-rolling.

Table 4.4: Corrosion parameters after intergranular corrosion testing of pre-stretched and subsequently paint baked 6016 A.

Deformation	**Corrosion mode**	**Max. corrosion depth [μm]**	**Weight loss [mg/cm^2]**
0%	Local IGC (20-80 μm)	147	2.38
1%	Uniform IGC (50-125 μm)	208	3.43
5%	Uniform IGC (40-145 μm)	264	4.00
10%	Uniform IGC (95-170 μm)	260	5.25

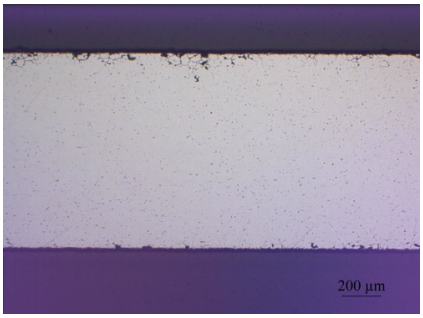

(a) Undeformed.

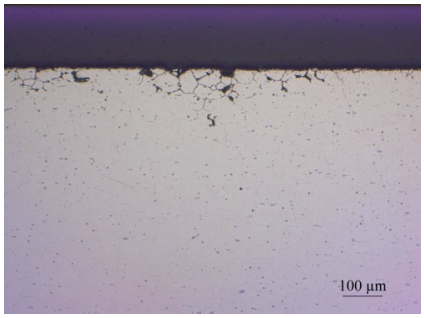

(b) Undeformed.

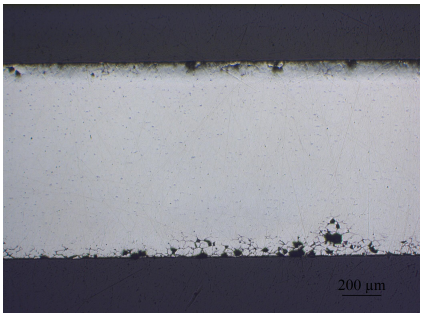

(c) 1% pre-stretched.

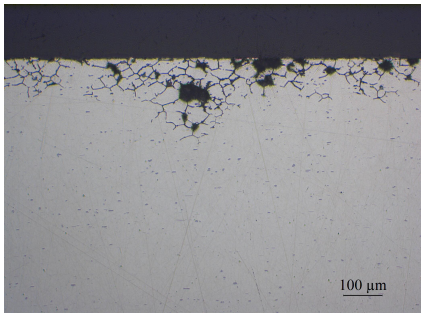

(d) 1% pre-stretched.

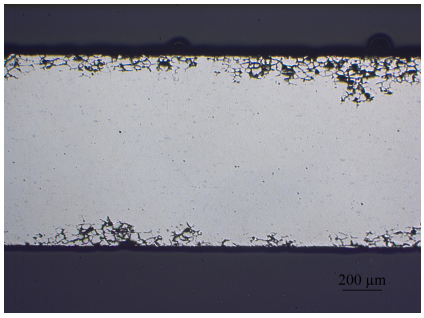

(e) 5% pre-stretched.

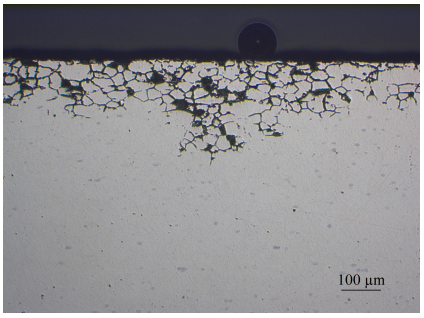

(f) 5% pre-stretched.

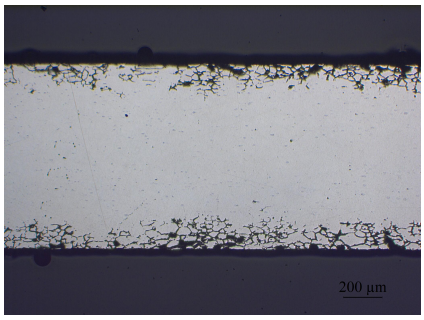

(g) 10% pre-stretched.

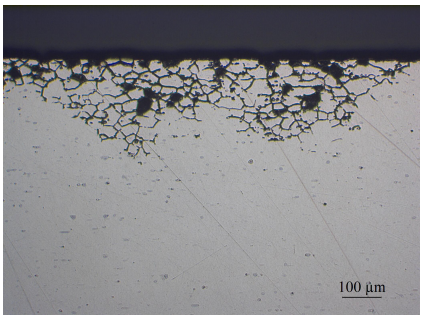

(h) 10% pre-stretched.

Figure 4.10: Optical micrographs of cross section parallel to rolling direction of pre-stretched, subsequently paint baked and corrosion tested 6016 A. Figure (a), (c), (e) and (g) show corrosion attacks in representative areas. Figure (b), (d), (f) and (h) show the most severe attacks. The scale bar is 200 µm in Figure (a), (c), (e) and (g).

Pre-rolling of 6016 A, T6 tempered

Micrographs of T6 tempered 6016 A, undeformed and 10% pre-deformed by rolling, are displayed in Figure 4.11. The corrosion parameters are summarized in Table 4.5. These samples were pre-deformed after SHT. Severe, uniform IGC is observed in the undeformed sample. The 10% pre-rolled sample exhibits shallower corrosion depth. However, a modest etching of the surface, characterized by very shallow pits spread over the entire surface causing relatively large weight loss, is observed as indicated in Figure 4.11c and 4.11d. Slightly improved IGC resistance as a consequence of pre-rolling after SHT is in contradiction to the result obtained for the paint baked 6016 A samples, pre-deformed after pre-baking, in which the IGC susceptibility grew more severe with increasing pre-deformation.

Table 4.5: Corrosion parameters after intergranular corrosion testing of pre-rolled and subsequently T6 tempered 6016 A.

Deformation	Corrosion mode	Max. corrosion depth [μm]	Weight loss [mg/cm^2]
0%	Uniform IGC (50-270 μm)	308	6.65
10%	Uniform etching, IGC and pitting (50-200 μm)	256	6.98

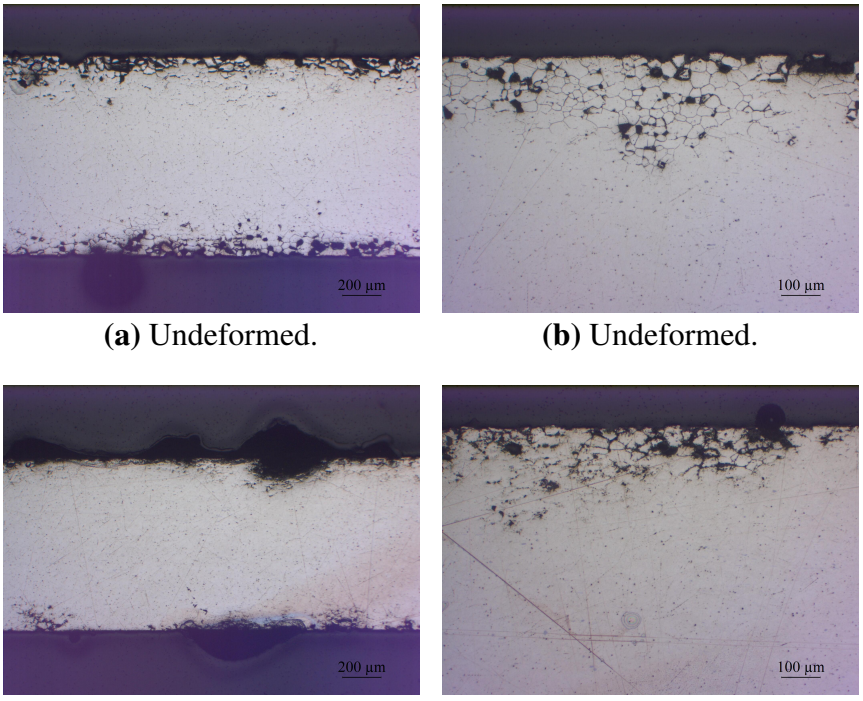

(a) Undeformed. **(b)** Undeformed.

(c) 10% pre-rolled. **(d)** 10% pre-rolled.

Figure 4.11: Optical micrographs of cross section parallel to rolling direction of pre-rolled, subsequently T6 tempered and corrosion tested 6016 A. Figure (a) and (c) show corrosion attacks in representative areas. Figure (b) and (d) show the most severe attacks. The scale bar is 200 μm in Figure (a) and (c).

Pre-rolling of 6016 B, paint baked

Micrographs of pre-baked, pre-rolled and subsequently paint baked 6016 B are displayed in Figure 4.12 and the corrosion parameters are summarized in Table 4.6. It is evident that this alloy exhibits extensive, uniform IGC regardless of pre-rolling. A relatively large amount of grains has detached from all samples due to the comprehensive IGC. There are small variations in maximum corrosion depth, as well as weight loss, but it is not readily seen a

general trend in the effect of pre-rolling on corrosion properties of this alloy, except that pre-rolling has little effect.

Table 4.6: Corrosion parameters after intergranular corrosion testing of pre-rolled and subsequently paint baked 6016 B.

Deformation	**Corrosion mode**	**Max. corrosion depth [μm]**	**Weight loss [mg/cm^2]**
0%	Uniform IGC (200-320 μm)	398	15.5
1%	Uniform IGC (200-320 μm)	406	16.6
5%	Uniform IGC (200-300 μm)	326	15.6
10%	Uniform IGC (200-340 μm)	355	16.8

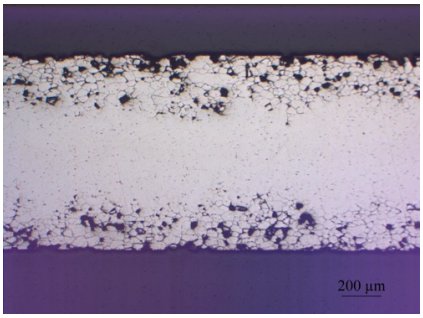

(a) Undeformed.

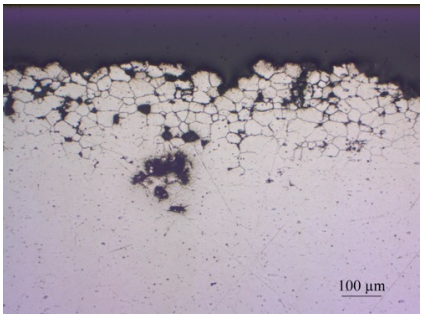

(b) Undeformed.

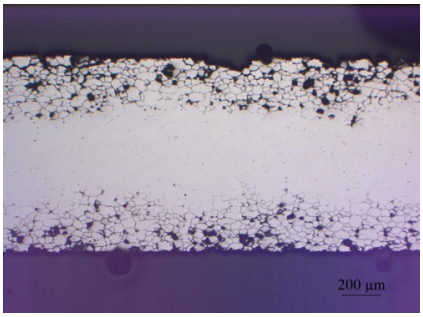

(c) 1% pre-rolled.

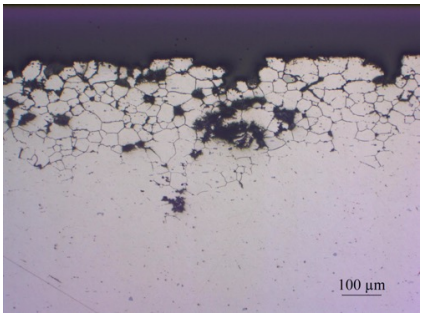

(d) 1% pre-rolled.

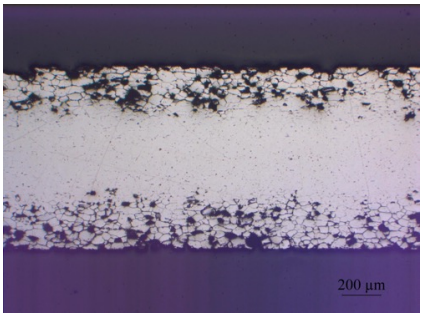

(e) 5% pre-rolled.

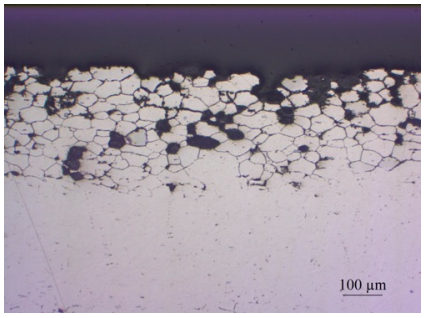

(f) 5% pre-rolled.

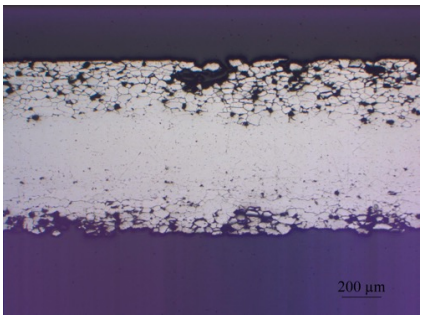

(g) 10% pre-rolled.

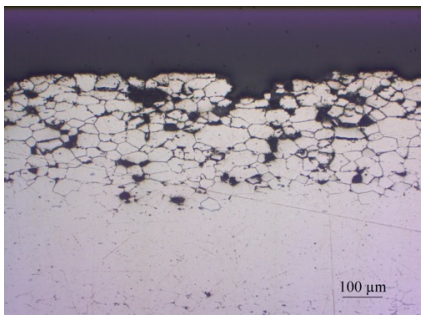

(h) 10% pre-rolled.

Figure 4.12: Optical micrographs of cross section parallel to rolling direction of pre-rolled, subsequently paint baked and corrosion tested 6016 B. Figure (a), (c), (e) and (g) show corrosion attacks in representative areas. Figure (b), (d), (f) and (h) show the most severe attacks. The scale bar is 200 µm in Figure (a), (c), (e) and (g).

Pre-stretching of 6016 B, paint baked

Micrographs of undeformed and pre-stretched, paint baked 6016 B are displayed in Figure 4.13 and the corrosion parameters are summarized in Table 4.7. Comprehensive IGC and grain detachment have occurred in all pre-stretched samples, like the pre-rolled samples. The extent of corrosion in the pre-stretched samples seems roughly similar to the extent of corrosion in the undeformed sample and no obviously effect of pre-stretching on IGC resistance of paint baked 6016 B is observed.

Table 4.7: Corrosion parameters after intergranular corrosion testing of pre-stretched and subsequently paint baked 6016 B.

Deformation	**Corrosion mode**	**Max. corrosion depth [μm]**	**Weight loss [mg/cm^2]**
0%	Uniform IGC (200-320 μm)	398	15.5
1%	Uniform IGC (250-330 μm)	366	16.3
5%	Uniform IGC (230-300 μm)	352	15.1
10%	Uniform IGC (270-350 μm)	385	14.8

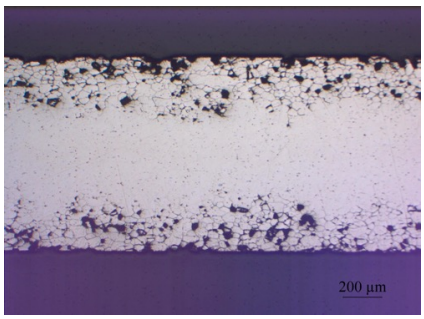

(a) Undeformed.

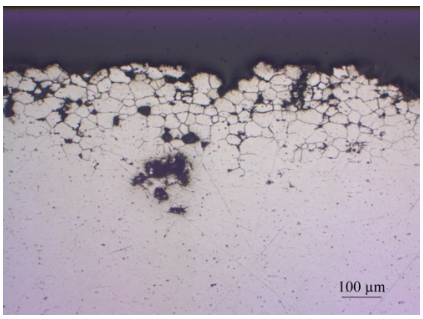

(b) Undeformed.

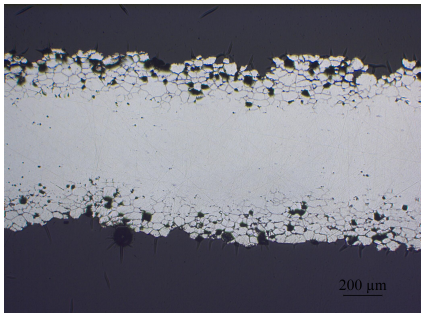

(c) 1% pre-stretched.

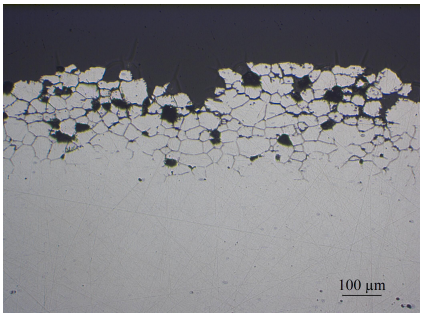

(d) 1% pre-stretched.

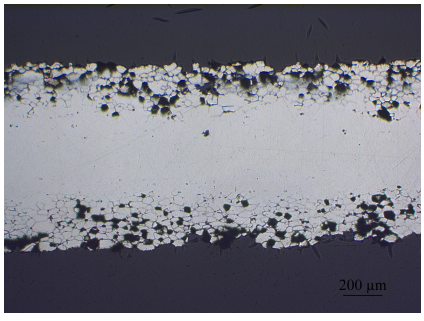

(e) 5% pre-stretched.

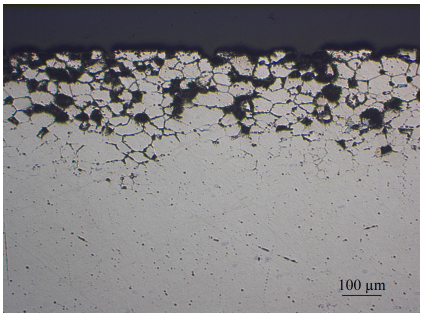

(f) 5% pre-stretched.

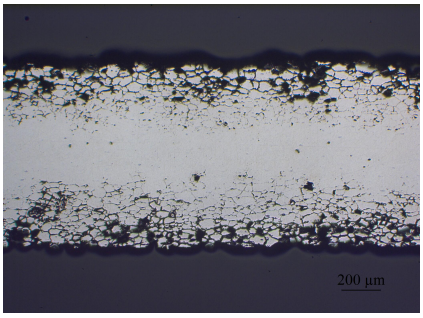

(g) 10% pre-stretched.

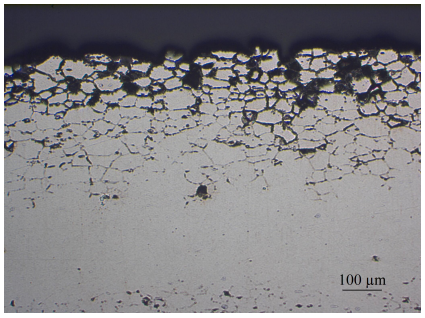

(h) 10% pre-stretched.

Figure 4.13: Optical micrographs of cross section parallel to rolling direction of pre-stretched, subsequently paint baked and corrosion tested 6016 B. Figure (a), (c), (e) and (g) show corrosion attacks in representative areas. Figure (b), (d), (f) and (h) show the most severe attacks. The scale bar is 200 µm in Figure (a), (c), (e) and (g).

Pre-rolling of 6016 B, T6 tempered

Corrosion damages in SHT, pre-rolled and T6 tempered 6016 B are shown in Figure 4.14 and the corrosion parameters are summarized in Table 4.8. The undeformed sample is heavily corroded by uniform IGC throughout the sample thickness. The mechanical integrity of this sample is strongly reduced. Moreover, large weight loss is measured for the sample and a lot of grains have detached.

The IGC susceptibility is significantly reduced at 10% pre-rolling. The corrosion mode for this sample is uniform etching, as well as a combination of IGC and pitting. Except for the etching, the profound corrosion attacks are confined to discrete sites.

Table 4.8: Corrosion parameters after intergranular corrosion testing of pre-rolled and subsequently T6 tempered 6016 B.

Deformation	**Corrosion mode**	**Max. corrosion depth [µm]**	**Weight loss [mg/cm^2]**
0%	Uniform IGC (500 µm)	500	17.0
10%	Uniform etching, IGC and pitting (30-330 µm)	391	13.6

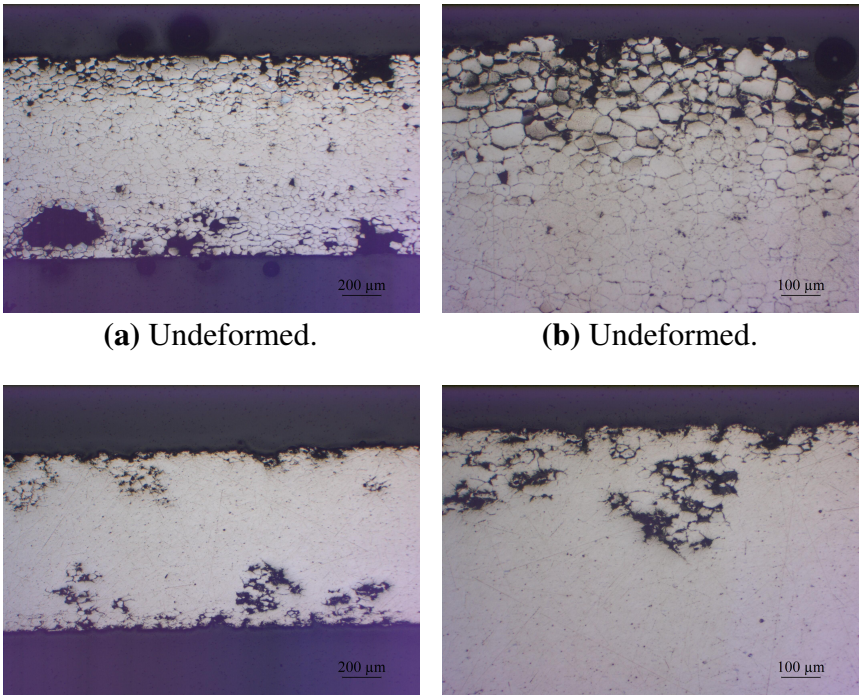

(a) Undeformed. **(b)** Undeformed.

(c) 10% pre-rolled. **(d)** 10% pre-rolled.

Figure 4.14: Optical micrographs of cross section parallel to rolling direction of pre-rolled, subsequently T6 tempered and corrosion tested 6016 B. Figure (a) and (c) show corrosion attacks in representative areas. Figure (b) and (d) show the most severe attacks. The scale bar is 200 µm in Figure (a) and (c).

4.3.2 Effect of post-deformation on IGC

The effect of deformation after the final ageing treatment on IGC susceptibility is presented for 6005.40 and C28 in the following sections. The undeformed samples are included for comparison in these sections as well.

Post-rolling of 6005.40

Micrographs of undeformed and post-rolled 6005.40 are displayed in Figure 4.15 and the corrosion parameters are summarized in Table 4.9. The 1% post-rolled sample exhibits uniform IGC as the undeformed sample, but the weight loss is lower for the 1% post-rolled sample. Improved IGC resistance is observed in 5 and 10% post-rolled samples, as the IGC attacks are confined to localized corrosion and large areas without IGC are observed. This is evident in Figure 4.15e and 4.15g. However, the susceptible areas exhibit profound IGC. Moreover, the IGC attacks occur in vicinity of the edges of the samples and the edges are significantly corroded as well. Hence, the weight losses are fairly large for these samples. The extent of edge corrosion in the undeformed and the 10% post-rolled sample is displayed in Figure 4.16.

Table 4.9: Corrosion parameters after intergranular corrosion testing of T6 tempered and subsequently post-rolled 6005.40.

Deformation	**Corrosion mode**	**Max. corrosion depth [µm]**	**Weight loss [mg/cm^2]**
0%	Uniform IGC (200-430 µm)	529	7.75
1%	Uniform IGC (100-430 µm)	551	5.20
5%	Local IGC (120-360 µm)	557	4.49
10%	Local IGC (40-400 µm)	530	5.22

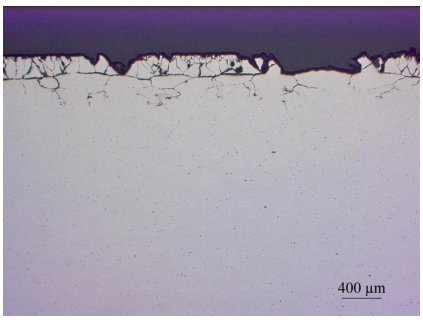

(a) Undeformed.

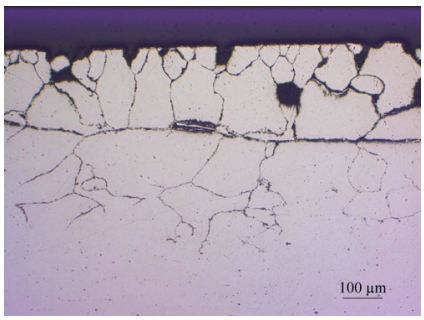

(b) Undeformed.

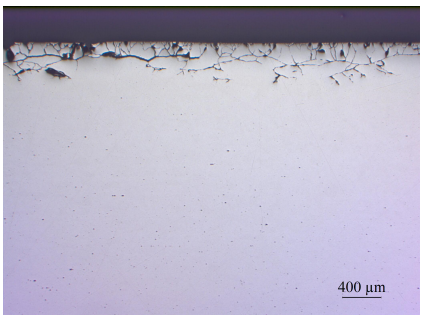

(c) 1% post-rolled.

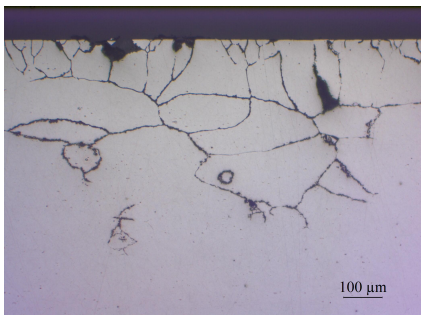

(d) 1% post-rolled.

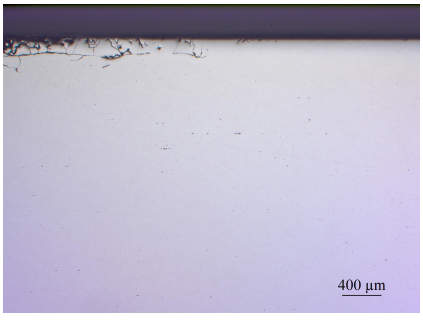

(e) 5% post-rolled.

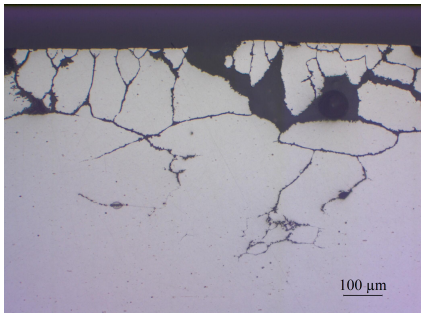

(f) 5% post-rolled.

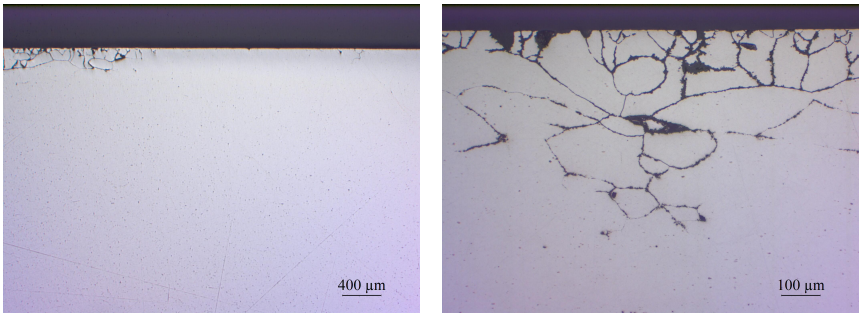

(g) 10% post-rolled. **(h)** 10% post-rolled.

Figure 4.15: Optical micrographs of cross section parallel to extrusion direction of T6 tempered, subsequently post-rolled and corrosion tested 6005.40. Figure (a), (c), (e) and (g) show corrosion attacks in representative areas. Figure (b), (d), (f) and (h) show the most severe attacks.

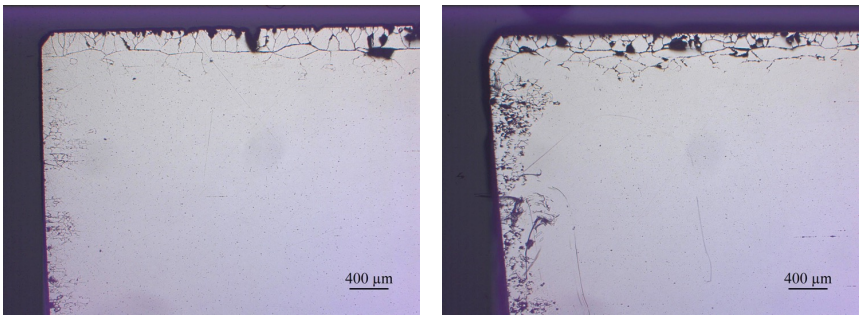

(a) Undeformed. **(b)** 10% post-rolled.

Figure 4.16: Optical micrographs of edge corrosion in undeformed and 10% post-rolled, T6 tempered 6005.40 after intergranular corrosion testing. The view plane is cross-sectional area parallel to extrusion direction.

Post-stretching of 6005.40

Micrographs of undeformed and post-stretched 6005.40 are displayed in Figure 4.17 and the corrosion parameters are summarized in Table 4.10. The aforementioned surface layer of approximately 200 µm is partly removed from 6005.40 to some extent due to uniform IGC, regardless of degree of post-stretching. The metallographic examinations reveal that the IGC front has propagated underneath the layer and further into the material on all samples. The 1 and 5% post-stretched samples seem most heavily corroded, whereas the 10% post-stretched sample seems less susceptible to IGC by inspection of the micrographs. This is supported by the data in Table 4.10. However, the variations are not large and all samples exhibit uniform and extensive IGC.

Table 4.10: Corrosion parameters after intergranular corrosion testing of T6 tempered and subsequently post-stretched 6005.40.

Deformation	**Corrosion mode**	**Max. corrosion depth [µm]**	**Weight loss [mg/cm^2]**
0%	Uniform IGC (200-430 µm)	529	7.75
1%	Uniform IGC (240-490 µm)	592	8.23
5%	Uniform IGC (220-440 µm)	603	7.38
10%	Uniform IGC (200-420 µm)	519	6.12

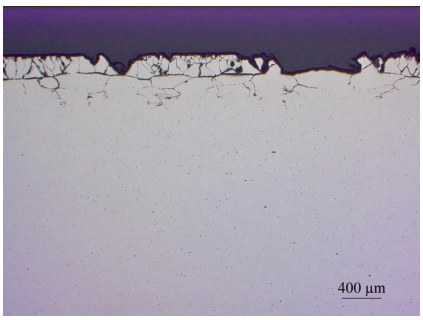

(a) Undeformed.

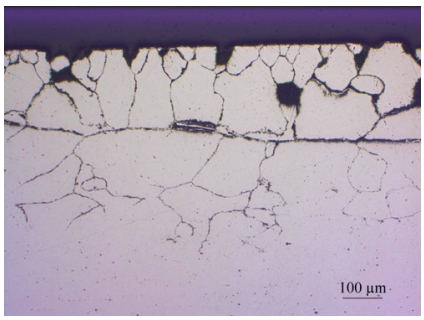

(b) Undeformed.

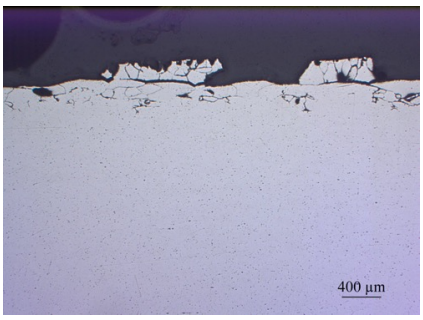

(c) 1% post-stretched.

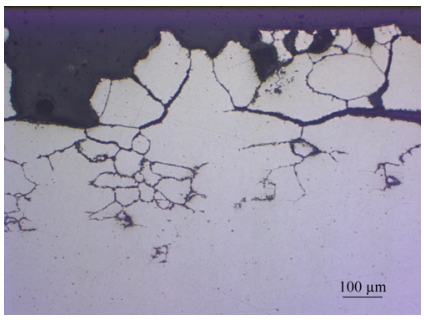

(d) 1% post-stretched.

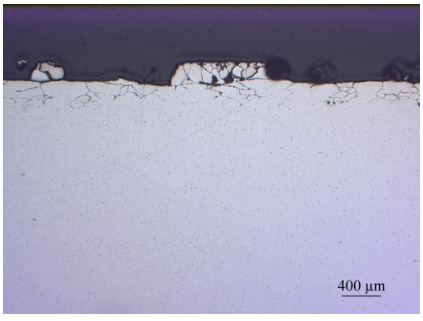

(e) 5% post-stretched.

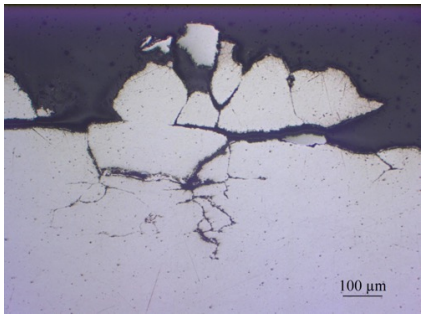

(f) 5% post-stretched.

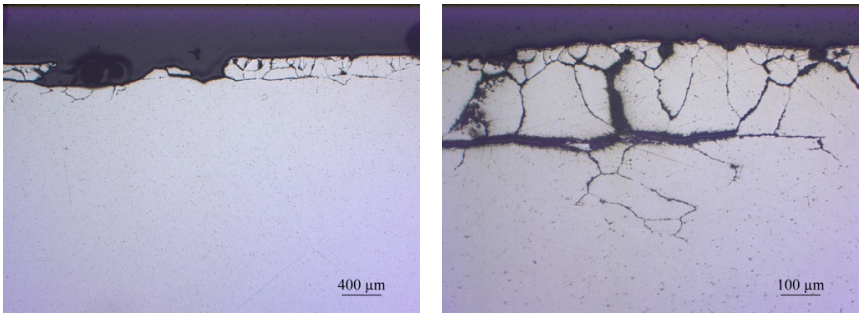

(g) 10% post-stretched. **(h)** 10% post-stretched.

Figure 4.17: Optical micrographs of cross section parallel to extrusion direction of T6 tempered, subsequently post-stretched and corrosion tested 6005.40. Figure (a), (c), (e) and (g) show corrosion attacks in representative areas. Figure (b), (d), (f) and (h) show the most severe attacks.

Post-rolling of C28

Micrographs of undeformed and post-rolled C28 are presented in Figure 4.18 and the corrosion parameters are summarized in Table 4.11. The undeformed sample suffers from quite profound, uniform IGC. However, a change in IGC morphology is indicated by the micrographs as a consequence of post-rolling. The IGC attacks are much narrower in the post-rolled samples in relation to the attacks in the undeformed sample. This can be observed in Figure 4.18c to 4.18h. Moreover, the corrosion attacks become roughly less profound as the degree of post-rolling increases. Nevertheless, the post-rolled samples are susceptible to uniform IGC as the undeformed sample, and additionally, a few pitting susceptible sites are observed.

Table 4.11: Corrosion parameters after intergranular corrosion testing of T6 tempered and subsequently post-rolled C28.

Deformation	**Corrosion mode**	**Max. corrosion depth [µm]**	**Weight loss [mg/cm^2]**
0%	Uniform IGC (360 µm)	428	3.88
1%	Uniform IGC, some pitting (30-390 µm)	437	4.26
5%	Shallow uniform IGC, some pitting (50-250 µm)	270	3.71
10%	Shallow uniform IGC, some pitting (30-230 µm)	339	3.98

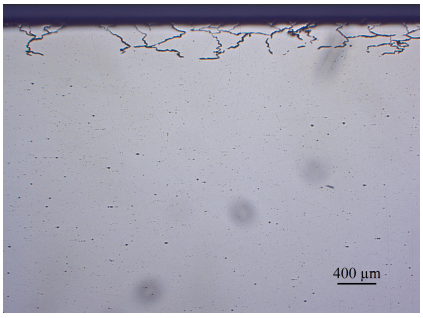

(a) Undeformed.

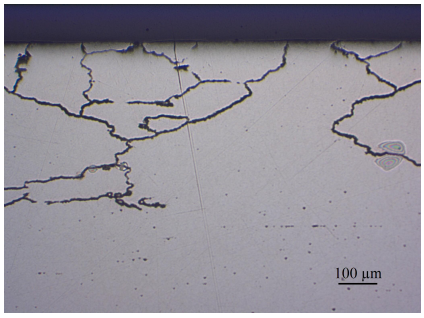

(b) Undeformed.

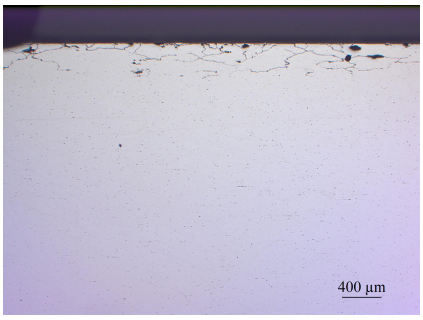

(c) 1% post-rolled.

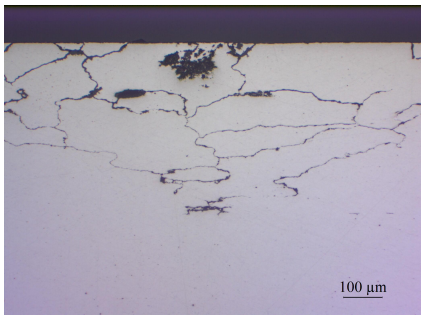

(d) 1% post-rolled.

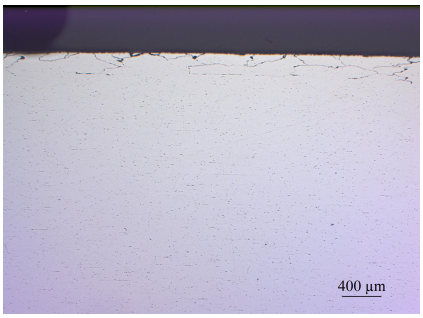

(e) 5% post-rolled.

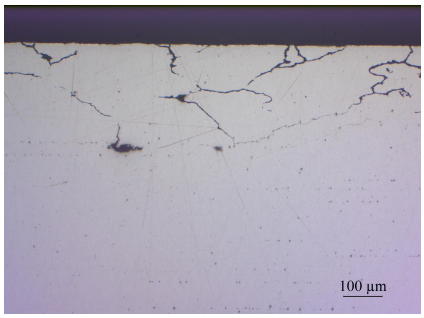

(f) 5% post-rolled.

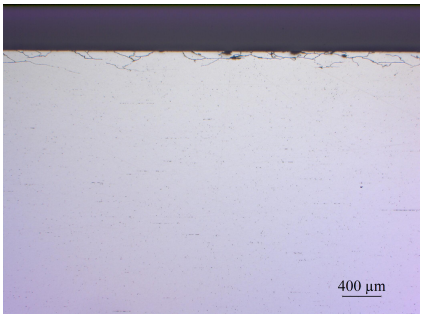

(g) 10% post-rolled.

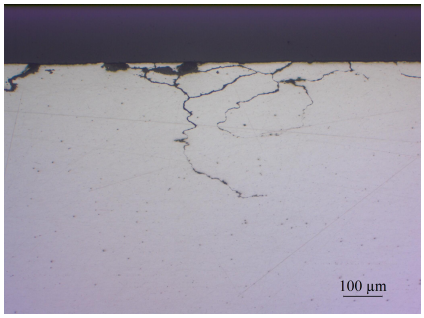

(h) 10% post-rolled.

Figure 4.18: Optical micrographs of cross section parallel to extrusion direction of T6 tempered, subsequently post-rolled and corrosion tested C28. Figure (a), (c), (e) and (g) show corrosion attacks in representative areas. Figure (b), (d), (f) and (h) show the most severe attacks.

Post-stretching of C28

The corrosion damages of undeformed and post-stretched C28 are displayed in Figure 4.19 and the corrosion parameters are summarized in Table 4.12. Both the undeformed and the post-stretched samples exhibit uniform IGC. However, the attacks are narrower in the post-stretched samples, like the post-rolled samples. Grain detachment has occurred to larger extent and this is particularly evident at 10% post-stretching, as can be observed in Figure 4.19g and 4.19h. No large differences in weight losses are measured, neither in the undeformed, post-rolled nor post-stretched C28 samples.

Table 4.12: Corrosion parameters after intergranular corrosion testing of T6 tempered and subsequently post-stretched C28.

Deformation	**Corrosion mode**	**Max. corrosion depth [μm]**	**Weight loss [mg/cm^2]**
0%	Uniform IGC (360 μm)	428	3.88
1%	Uniform IGC, some pitting (310 μm)	380	4.11
5%	Uniform IGC, some pitting (140-370 μm)	413	3.72
10%	Uniform IGC, some pitting (120-340 μm)	443	3.72

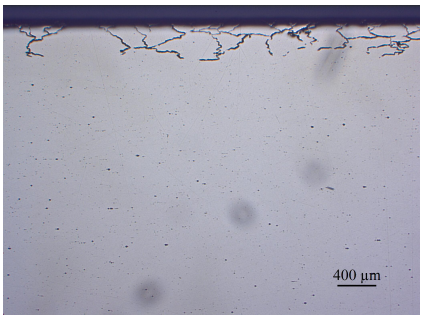

(a) Undeformed.

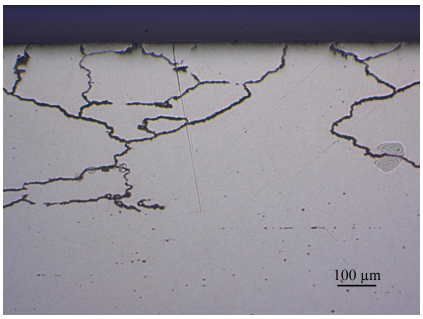

(b) Undeformed.

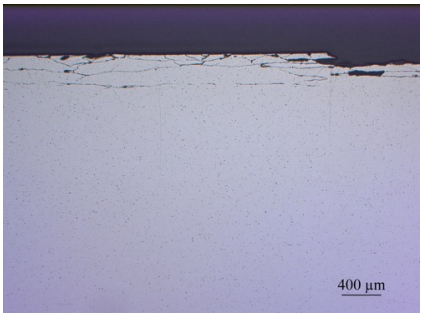

(c) 1% post-stretched.

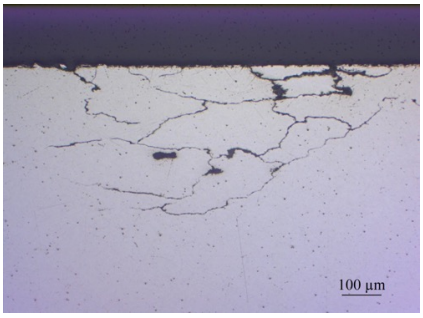

(d) 1% post-stretched.

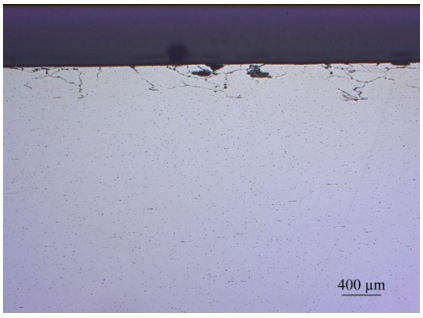

(e) 5% post-stretched.

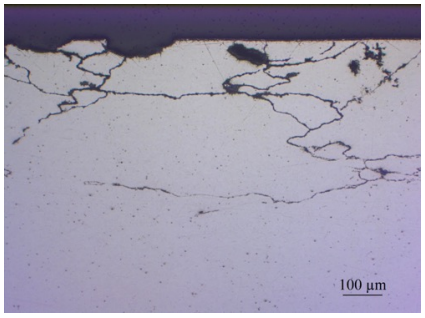

(f) 5% post-stretched.

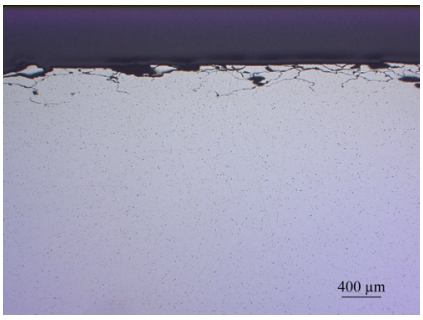

(g) 10% post-stretched.

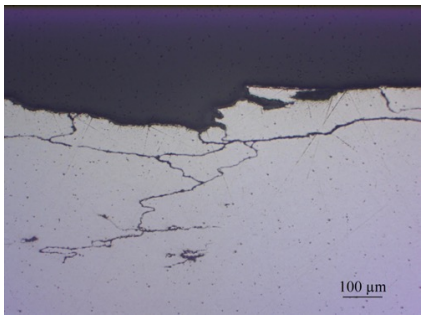

(h) 10% post-stretched.

Figure 4.19: Optical micrographs of cross section parallel to extrusion direction of T6 tempered, subsequently post-stretched and corrosion tested C28. Figure (a), (c), (e) and (g) show corrosion attacks in representative areas. Figure (b), (d), (f) and (h) show the most severe attacks.

4.4 SEM studies of 6005.40 surface

Studies in SEM were performed on undeformed, 10% pre-rolled, 10% post-rolled and 10% post-stretched 6005.40. The 10% pre-stretched sample was not studied in SEM since this sample had similar corrosion properties as the pre-rolled sample. The surface illustrated in Figure 3.8 in section 3.6.1 was examined and no grinding or polishing was performed on the surface prior to the examination, apart from electropolishing.

4.4.1 Backscatter imaging

The aim of backscatter imaging was to investigate any differences in microstructure regarding the distribution of particles on the surface of 6005.40. Figure 4.20 displays the acquired micrographs of the different samples. The backscatter images reveal that bright particles are more or less homogeneously distributed on the surface of all samples. Particles brighter than the aluminum matrix consist of elements heavier than aluminum itself. Thus, these particles are likely to be primary α phase particles (Al(FeMn)Si). It is not possible to discern any significant difference in the particle distribution or the particles themselves between the different deformation conditions.

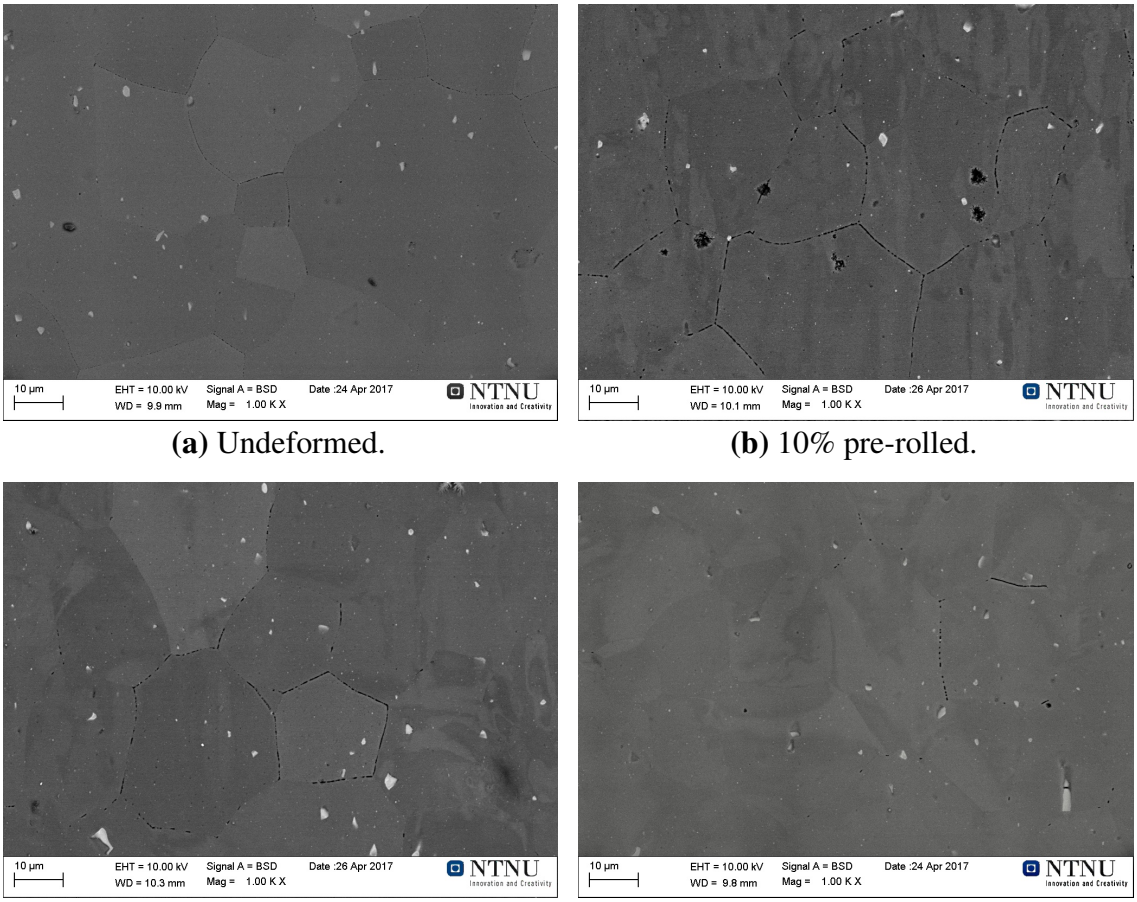

(a) Undeformed. **(b)** 10% pre-rolled.

(c) 10% post-rolled. **(d)** 10% post-stretched.

Figure 4.20: Backscatter images from scanning electron microscope studies of surface of T6 tempered 6005.40. The scale bar is 10 µm on all images.

4.4.2 EBSD

EBSD was performed on the surface of T6 tempered 6005.40 to investigate any differences in formation of subgrains with LAGBs between the undeformed and the deformed samples. Grain boundary misorientation histograms and pole figures of the samples are shown in Appendix E and F, respectively.

Undeformed 6005.40

Images of the grain structure and grain boundary misorientation of undeformed 6005.40 are displayed in Figure 4.21. The grain structure consists mainly of HAGBs with misorientation angle larger than 15°. The fraction of HAGBs is 0.895.

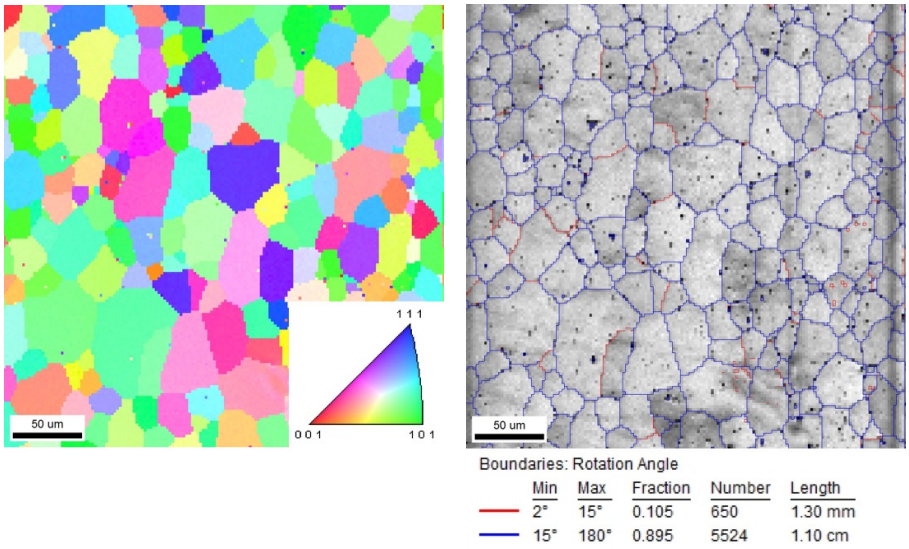

(a) Grain structure. **(b)** Grain boundary misorientation.

Figure 4.21: Electron backscatter diffraction in scanning electron microscope of surface of undeformed, T6 tempered 6005.40. The scale bar is 50 µm on both images.

10% pre-rolled 6005.40

In Figure 4.22 grain structure and grain boundary misorientation of 10% pre-rolled 6005.40 are displayed. HAGBs exist between the grains in Figure 4.22a. However, as indicated by the red lines in Figure 4.22b, deformation bands with LAGBs are readily visible in the direction of rolling, and the fraction of LAGBs is 0.680. Moreover, the grains in Figure 4.22a appear more smudged in relation to the grains in the undeformed sample.

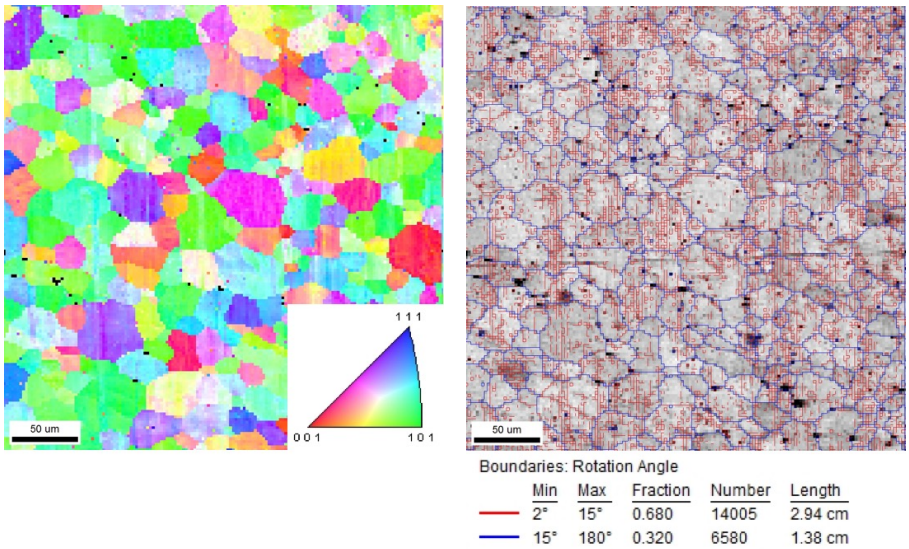

(a) Grain structure. **(b)** Grain boundary misorientation.

Figure 4.22: Electron backscatter diffraction in scanning electron microscope of surface of 10% pre-rolled, T6 tempered 6005.40. The scale bar is 50 µm on both images.

10% post-rolled 6005.40

Images of grain structure and grain boundary misorientation of 10% post-rolled 6005.40 are presented in Figure 4.23. There are many similarities between the grain structure in this sample and the 10% pre-rolled sample. The grains in both samples appear smudged, and subgrain structures with LAGBs are evident in the direction of rolling. The fraction of LAGBs is 0.608 in the 10% post-rolled sample, hence it is slightly higher in the pre-rolled sample.

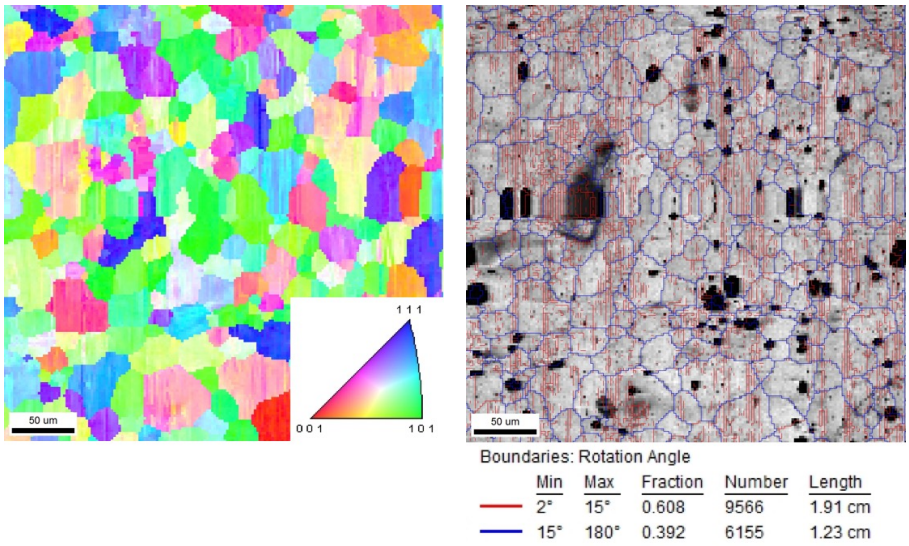

(a) Grain structure. **(b)** Grain boundary misorientation.

Figure 4.23: Electron backscatter diffraction in scanning electron microscope of surface of T6 tempered and subsequently 10% post-rolled 6005.40. The scale bar is 50 µm on both images.

10% post-stretched 6005.40

Images of grain structure and grain boundary misorientation of 10% post-stretched 6005.40 are presented in Figure 4.24. This sample differs slightly from the other deformed samples, since Figure 4.24a indicates that the grains are less smudged. Moreover, the LAGBs seem to be less directional in the stretching direction in relation to in the rolled samples. Nevertheless, the fraction of LAGBs is substantial, 0.539, and considerably larger than in the undeformed sample.

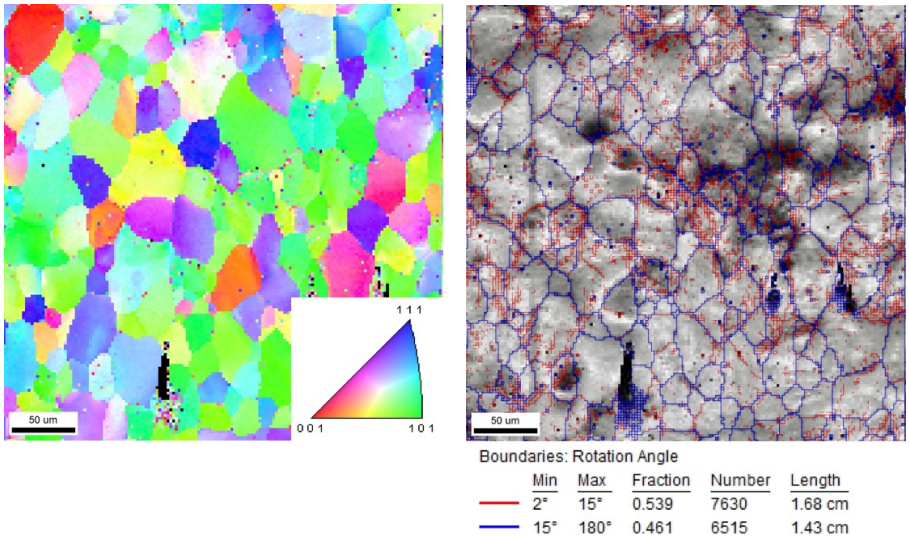

(a) Grain structure. **(b)** Grain boundary misorientation.

Figure 4.24: Electron backscatter diffraction in scanning electron microscope of surface of T6 tempered and subsequently 10% post-stretched 6005.40. The scale bar is 50 μm on both images.

4.5 TEM studies of 6005.40 surface

Studies in TEM were performed on undeformed and 10% pre-rolled, T6 tempered 6005.40, on the surface illustrated in Figure 3.8 in section 3.6.1. The results of TEM imaging, HAADF-STEM imaging and EDS mapping are presented in the following sections.

4.5.1 TEM imaging

TEM imaging was performed to document the distribution of precipitates and to reveal potential dislocation networks in the undeformed and the 10% pre-rolled sample. The result is displayed in Figure 4.25. A high number density of homogeneously distributed, needle shaped precipitates is evident in the undeformed sample in Figure 4.25a. In the 10% pre-rolled sample in Figure 4.25b, dislocation lines are revealed and it is apparent that precipitates have formed on the dislocations. The number density of precipitates seems lower in the pre-rolled material. Moreover, it was noted during the HAADF-STEM examination that precipitates in the pre-rolled material appeared somewhat coarser than in the undeformed material.

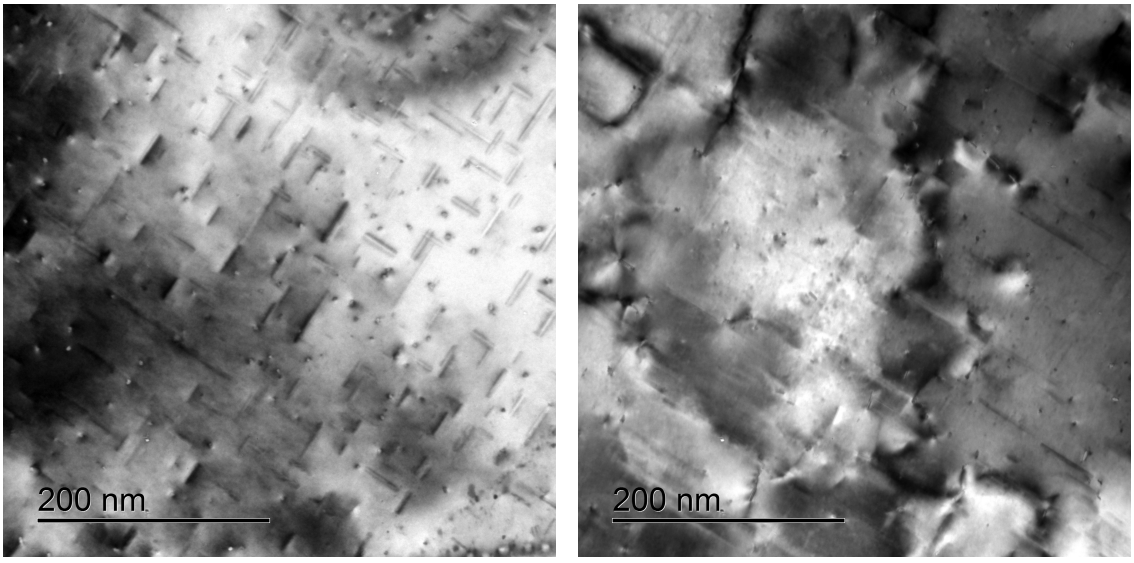

(a) Undeformed. **(b)** 10% pre-rolled.

Figure 4.25: Transmission electron microscope images of surface of undeformed and 10% pre-rolled, T6 tempered 6005.40.

4.5.2 HAADF-STEM imaging

HAADF-STEM imaging was performed to see precipitate structure details and assess the Cu distribution within the precipitates. The result of the examination is presented in Figure 4.26 and 4.27. Cu atomic columns have high atomic number contrast and appear as bright spots in the HAADF-STEM images. In the undeformed 6005.40 sample mainly β''/disordered precipitates were found, and one is displayed in Figure 4.26a. A few Cu atomic columns are evident in this precipitate, but only in the disordered regions. Bright Cu atomic columns were also found to occur on the precipitate/matrix interface of several precipitates in the undeformed sample.

The predominating precipitate in the 10% pre-rolled 6005.40 sample had different structure. A disordered Q′/B′ precipitate, which was the most frequent in the pre-rolled sample, is displayed in Figure 4.26b. Quite a few Cu atomic columns are observed in the precipitate. Figure 4.27 shows how Cu containing precipitates have formed presumably along a dislocation line in the pre-rolled material. The number of Cu atomic columns was generally higher in precipitates in the pre-rolled sample in relation to in the undeformed sample. However, it should be noted that Cu free β'' precipitates were found in the pre-rolled material as well, although disordered Q′/B′ precipitates were predominating in the 10% pre-rolled sample.

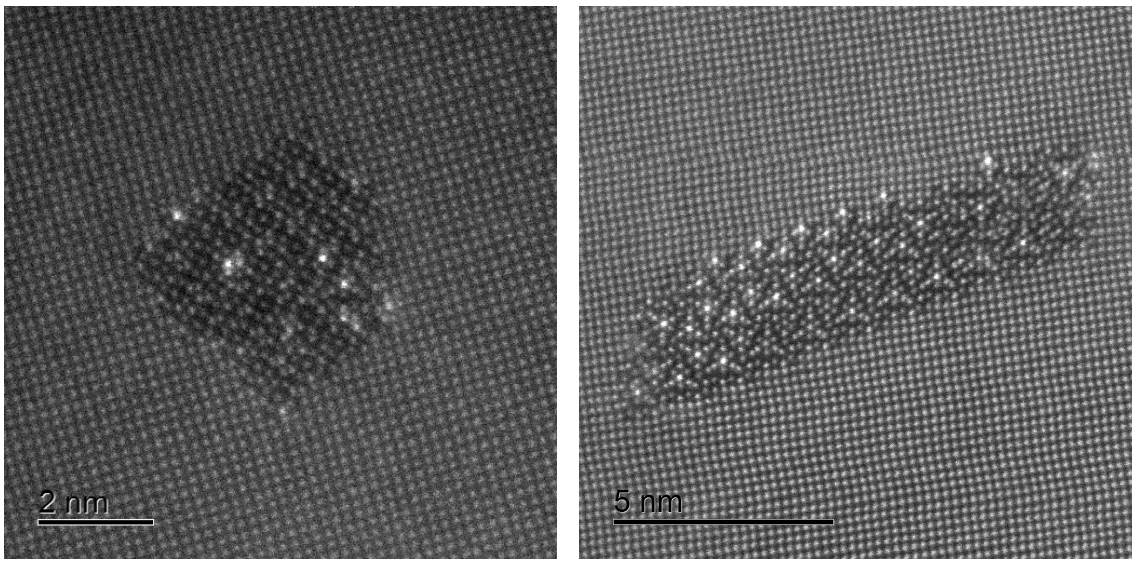

(a) Undeformed. **(b)** 10% pre-rolled.

Figure 4.26: High angle annular dark field scanning transmission electron microscope images of precipitates in undeformed and 10% pre-rolled, T6 tempered 6005.40.

Figure 4.27: High angle annular dark field scanning transmission electron microscope image of precipitates presumably along a dislocation line in 10% pre-rolled, T6 tempered 6005.40.

4.5.3 EDS mapping

EDS mapping of a presumably HAGB and a primary α particle on the surface of 10% pre-rolled, T6 tempered 6005.40 was performed in STEM mode to determine grain boundary and particle composition. EDS mapping was not performed on the undeformed 6005.40 sample due to time constraints.

The elemental maps of the grain boundary depicted in Figure 4.28a are displayed in Figure 4.28b to 4.28e. Discrete precipitates rich in Mg and Si on the grain boundary, as well as a Mg and Si depleted zone along the grain boundary, are evident in Figure 4.28c and 4.28d. Moreover, Cu is incorporated into the grain boundary precipitates and it is possible to discern what looks like a continuous, Cu rich film along the grain boundary in Figure 4.28e. Depletion of Cu in the PFZ is however scarcely visible, and the Cu depleted zone is in any case much narrower than the Mg and Si depleted zone. The large Cu depleted area on one side of the grain boundary in Figure 4.28e is probably due to the orientation of the grain and is not a real PFZ.

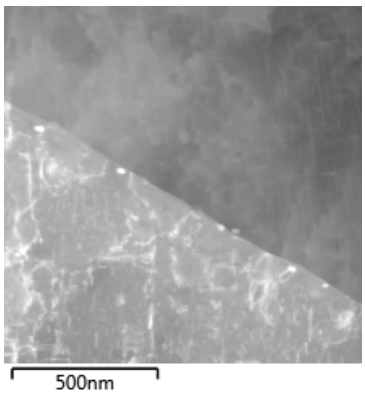

(a) Grain boundary.

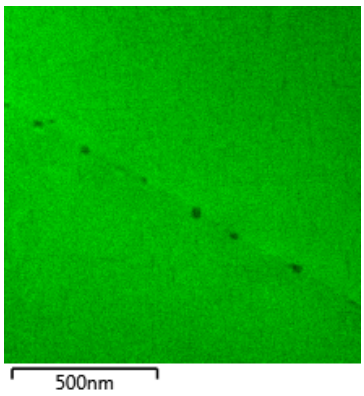

(b) Al.

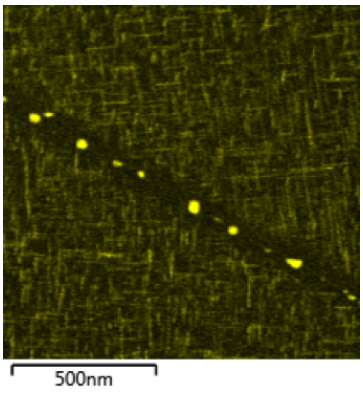

(c) Mg.

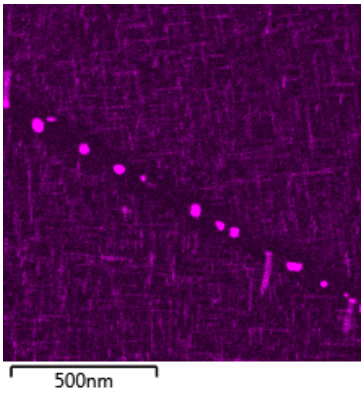

(d) Si.

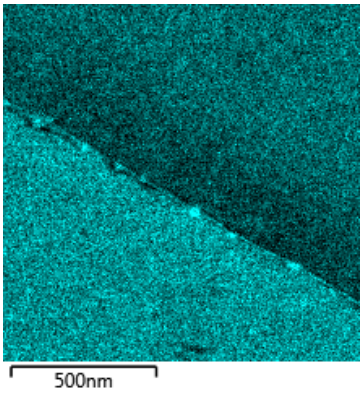

(e) Cu.

Figure 4.28: Energy dispersive X-ray spectroscopy mapping of a presumably high angle grain boundary in 10% pre-rolled, T6 tempered 6005.40.

The elemental maps of the primary α particle depicted in Figure 4.29a are displayed in Figure 4.29b to 4.29g. It is evident that the particle primarily contains Si, Fe and Mn. Cu is also somewhat incorporated into the particle. Precipitates containing Mg, Si and Cu are discernible along the periphery of the particle.

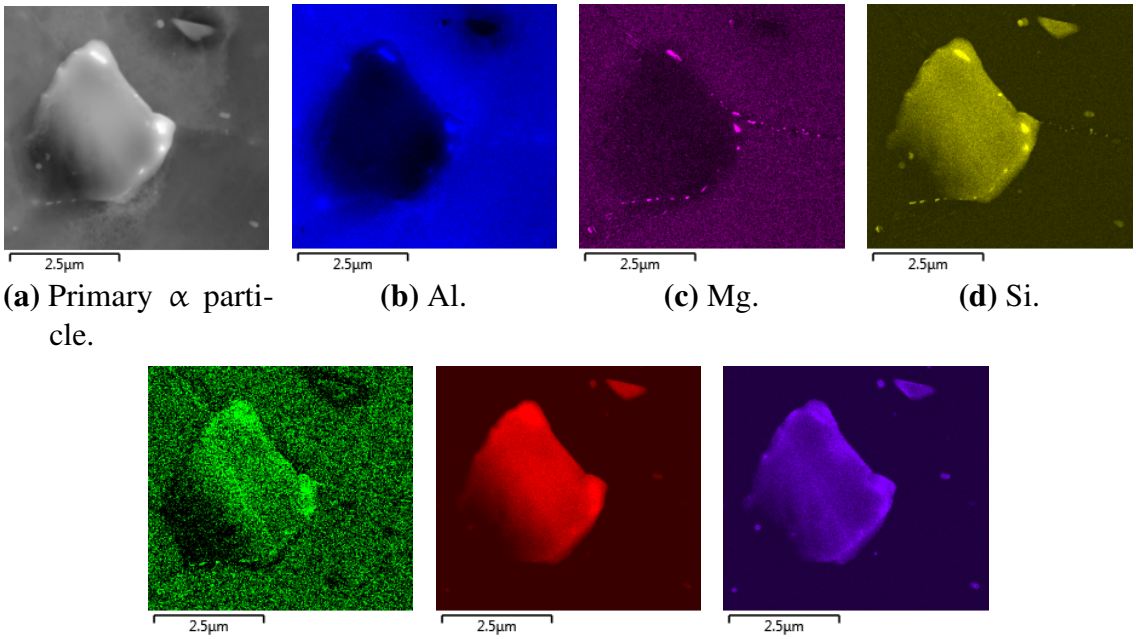

(a) Primary α particle. **(b)** Al. **(c)** Mg. **(d)** Si.

(e) Cu. **(f)** Fe. **(g)** Mn.

Figure 4.29: Energy dispersive X-ray spectroscopy mapping of a primary α particle in 10% pre-rolled, T6 tempered 6005.40.

Chapter 5

Discussion

5.1 Effect of pre-deformation on hardness

Vickers hardness measurements (HV1) were performed on pre- and post-deformed samples to assess the effect of deformation on mechanical properties of AlMgSi alloys. The hardness was measured both before and after ageing for the pre-deformed samples.

The general trend for all alloys before ageing was increasing hardness as a function of increasing pre-deformation. Taking standard deviations into consideration, there was a roughly linear increase. This was for instance observed for pre-rolled 6005.40 in Figure 4.3a in section 4.2.1, in which the difference in hardness between the undeformed and the 10% pre-rolled sample was more than 20 HV. Strain hardening is the predominating strengthening mechanism in annealed or slightly aged condition for deformed, heat treatable aluminum alloys [24]. As detailed in section 2.4.1, the mechanical properties are enhanced as a function of increasing %CW during strain hardening [53]. Thus, the observed result is as expected considering the theoretical aspect.

Results presented in section 4.2.1 and 4.2.2 indicated that the effect of pre-deformation on hardness after ageing was dependent on ageing time. The measured hardness after pre-rolling and ageing of 6005.40, 6016 A and 6016 B is summarized in Figure 5.1. As elaborated in section 2.4.4, the hardening mechanism in pre-deformed and subsequently artificially aged materials is complex, considering that the materials are subjected to a combination of strain hardening and age hardening [60]. The dislocations introduced in the material during deformation cause improved mechanical properties [53]. However, annihilation of these dislocations occurs during subsequent ageing [78], and the density of β'', which is related to maximum hardness, is lower after ageing of a pre-deformed material compared to an undeformed material [25, 26]. Thus, the age hardening response is lower in pre-deformed materials. Studies have shown different results regarding the effect of pre-deformation on mechanical properties of AlMgSi alloys [77, 79, 82, 84]. In the present work it was found that the hardness of T6 tempered 6005.40 was independent of degree of pre-deformation, that is approximately equal for the undeformed and the pre-deformed samples, as illustrated in Figure 5.1. This result is in accordance to the result obtained during the specialization project [28], in which the hardness of all T6 tempered AlMgSi alloys examined was independent of degree of pre-deformation. Moreover, the result corresponds to the findings Furu et al. [79] obtained in a study of the effect of pre-deformation on yield strength of AA6005. They found that maximum yield strength was independent of whether the material was pre-deformed or not.

The fact that the hardness of 6005.40 was independent of degree of pre-deformation, demonstrates that the hardness contribution from dislocations compensates for the lower age hardening response at peak ageing in the case of pre-deformed condition. However, the dislocations are not providing enough strain hardening in this alloy to obtain higher peak hardness in the pre-deformed samples, as Kolar et al. [77] observed in their study of the effect of pre-deformation on hardness.

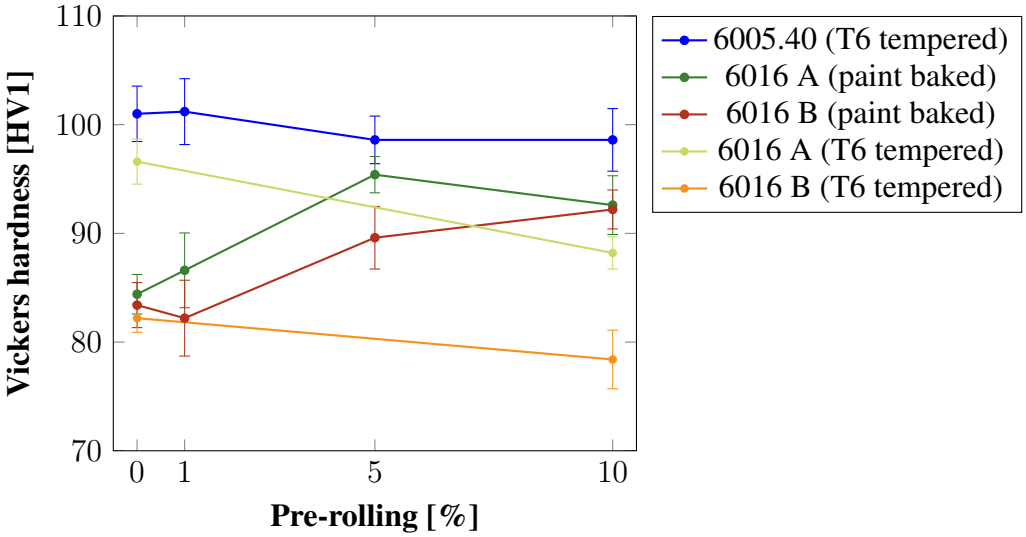

Figure 5.1: Comparison of Vickers hardness (HV1) after pre-rolling and ageing of 6005.40, 6016 A and 6016 B, subjected to different heat treatments.

Nevertheless, due to differences in heat treatment and chemical composition, the hardness after ageing of the 6016 alloys was not independent of deformation degree. The hardness after ageing of paint baked 6016 increased slightly with increasing pre-deformation, as can be seen for the pre-rolled samples in Figure 5.1. These alloys were aged to simulate the paint bake cycle used in the automotive industry and were accordingly subjected to a short ageing treatment. Hence, the samples were somewhat underaged [62–64]. Fewer dislocations are annealed out in underaged temper as annihilation of dislocations is dependent on time at elevated temperature [79]. The strain hardening is therefore more substantial in an underaged material in relation to a peak aged material. Zhen et al. [25] found considerably difference in dislocation density in 5 and 10% pre-deformed materials compared to undeformed materials after ageing for 30 min at 180°C. Hence, the increasing dislocation density in the material after paint baking as a function of degree of pre-deformation, contributes to increasing hardness.

Increased hardness and strength as degree of pre-deformation increased were also observed in the studies of Kolar et al. [77] and Furu et al. [79] early in the ageing procedures. These results and the result presented herein demonstrate that pre-deformation may be advantageous for AlMgSi alloys used in the automotive industry, considering that higher hardness is achieved for pre-deformed materials compared to undeformed materials in underaged temper. On average, the hardness was approximately 8 HV higher for 10% pre-deformed 6016 compared to undeformed 6016 after ageing. However, pre-deformation

also caused higher hardness in the 6016 alloys before ageing. Furthermore, the increase in hardness as a consequence of simulated paint baking was much lower for the pre-deformed samples than the undeformed samples. In fact, there was no difference in hardness before and after paint baking for 10% pre-rolled 6016 A and B, as can be seen in Figure 4.3b and 4.3c in section 4.2.1. This is an unwanted consequence of pre-deformation as it is favorable that the mechanical response is low before paint baking, when the shaping and forming procedure to a body-in-white is performed. Too high hardness and strength during this operation may risk the formability [101]. Hence, although pre-deformation of paint baked 6016 alloys results in higher hardness after paint baking, the increase in mechanical response prior to paint baking, due to strain hardening, may be adverse.

In addition to paint baking, another set of 6016 samples was subjected to the same ageing procedure as 6005.40, that is 5 h at 185°C after SHT and pre-rolling. The 10% pre-rolled 6016 samples subjected to this treatment reached slightly lower hardness than the corresponding undeformed samples, as can be observed in Figure 5.1. This strongly suggests that overageing occurred in the 10% pre-rolled 6016 alloys, considering that overageing is related to reduced hardness due to coarsening of the strengthening precipitates [24].

According to the literature reviewed in section 2.4.3, faster ageing kinetics are observed in pre-deformed materials [26, 77]. The activation energy for diffusion of solutes is lower in dislocation rich materials due to dislocation pipe diffusion, facilitating accelerated precipitation kinetics [80]. Therefore may pre-deformation of "T6 tempered" 6016 have led to faster overageing compared to the undeformed samples. However, the results indicated that 6005.40 subjected to equal ageing treatment did not overage due to pre-deformation, since a decline in hardness with increasing %CW was not observed. Difference in mechanical properties for materials subjected to equal thermomechanical treatment is likely to be caused by difference in chemical composition. 6016 A and B contain 1.49 and 1.33 wt% Si, respectively, compared to 0.62 wt% Si in 6005.40. Moreover, the 6016 alloys have greatly excess Si content with regard to the Mg_2Si stoichiometry. The high Si content in 6016 may explain the fast ageing kinetics, considering that Murayama et al. [64] observed faster ageing kinetics in alloys containing excess of Si, which resulted in faster overageing. On the other hand, Marioara et al. [55] found that the needle length of β'' increased more slowly in Si rich materials, giving slower ageing kinetics. Nevertheless, the result obtained in the present work suggests that the high content of Si in the 6016 alloys caused faster ageing kinetics, and hence overageing in 10% pre-rolled, "T6 tempered" 6016. The difference in hardness between the undeformed and the 10% pre-rolled sample was largest for 6016 A, in which the difference was 8.4 HV. 6016 A contains more Si than 6016 B, and accordingly the result corresponds well with the suggested hypothesis.

5.2 Effect of post-deformation on hardness

Hardness measurements after post-deformation were performed on 6005.40 and C28. These alloys were aged to T6 temper and subsequently deformed, hence strengthening precipitates were already formed and the materials were at their maximum hardness regarding age hardening capability prior to deformation. Nevertheless, strain hardening occurs during

deformation as dislocations are introduced in the material [53]. A slightly increase in hardness as a function of increasing post-deformation was observed for the stretched samples in Figure 4.6. Figure C.1 and C.4 in Appendix C show that 6005.40 and C28 work hardened to a modest extent during stretching, and this is expressed in the hardness values in terms of increased hardness. However, no general trend of increasing hardness as a function of increasing post-deformation was observed for the rolled samples, as shown in Figure 4.5, although it was expected an increase in dislocation density and thus strain hardening for these samples as well. This discrepancy remains unclear.

5.3 Effect of rolling versus stretching on hardness

Two different deformation techniques were used in this work; rolling and stretching. As detailed in section 2.4.2, deformation occurs differently in materials subjected to these types of cold working. Modest rolling results in a highly deformed surface and gradually reduction of deformation towards the center of the specimen. On average, the rolled specimen will be cold worked a certain percent, for instance 10%. On the other hand, a stretched specimen is nearly uniformly deformed throughout its thickness. Thus, considering that the hardness measurements were performed on the surface of the deformed samples (HV1), it is likely that the hardness was higher for the rolled samples. It was evident by the results in section 4.2.1 and 4.2.2 that the pre-rolled samples exhibited higher hardness before ageing and in underaged temper than the pre-stretched samples, as expected. However, the hardness of pre-rolled and pre-stretched, T6 tempered 6005.40 was equal. This demonstrates that in areas where the strain hardening is larger, the age hardening becomes correspondingly smaller in peak aged temper and vice versa, which accordingly implies once more that the hardness contribution from dislocations compensates for the lower age hardening response at peak ageing in the case of pre-deformed condition.

5.4 Effect of pre-deformation on IGC susceptibility

The main objective of this master thesis was to examine the effect of cold deformation on the IGC susceptibility of different AlMgSi alloys. The initially proposed hypothesis was that deformation would alter the microstructure and introduce a higher number of LAGBs in the material, which successively is advantageous for the corrosion properties. Minoda et al. [11] and Yang et al. [27] found that LAGBs were less susceptible to IGC compared to HAGBs, as a consequence of differences in the precipitates which form on LAGBs and HAGBs. This research was further detailed in section 2.3.2. Moreover, pre-deformation affects how precipitation during ageing occurs [25, 26], which in turn may influence corrosion properties and accordingly IGC susceptibility.

To study the effect of deformation on IGC susceptibility, different deformation techniques were used. AlMgSi alloys with dissimilar chemistry were either subjected to pre-deformation by rolling or stretching or post-deformation by rolling or stretching. Different heat treatments were performed on the alloys, and thermomechanical processing of all alloys was thoroughly

described in section 3.2. The only varying parameters for each alloy subjected to a given heat treatment were type and degree of deformation. Hence, any variations in corrosion behavior are attributable to variations in these parameters. The most extensively studied alloy in this work was 6005.40. Therefore, the discussion will focus mainly on this alloy. Moreover, the focus will be on the difference between undeformed and 10% deformed samples, as the difference between these samples was most apparent. The effect of 1% deformation was generally minor for all alloys, although some effect was observed in a few cases. This is as expected considering that the dislocation density in 1% deformed materials is assumed to be low [25].

The effect of pre-deformation on IGC susceptibility of AlMgSi alloys was first studied by the author during fall 2016 in the specialization project [28]. The results from that study indicated that pre-deformation had beneficial influence on the IGC resistance of the examined alloys. It was proposed that pre-deformation altered the orientation of the surface grains, making the grain boundaries at the surface less accessible for corrosive media. However, examinations of the microstructure of the pre-deformed materials in LM revealed that there was no difference in orientation of the surface grains between undeformed and pre-deformed materials, although the corrosion susceptibility was lower in the pre-deformed samples. The effect of pre-deformation on IGC was further studied in this work in order to achieve a better understanding of the corrosion mechanism in pre-deformed materials. Results obtained during metallographic examinations of IGC tested AlMgSi alloys revealed that the effect of pre-deformation on corrosion susceptibility was highly dependent on heat treatment before and after deformation. To study the different cases, the discussion is divided in two sections which concern pre-deformation after SHT and after pre-baking, respectively.

5.4.1 Pre-deformation subsequent to solution heat treatment

6005.40 was pre-deformed by rolling or stretching after SHT and subsequently aged to T6 temper. The result, presented in its entirety in section 4.3.1, indicated that pre-deformation by either rolling or stretching considerably reduced the IGC susceptibility of 6005.40. Uniform IGC in the undeformed sample was confined to localized pitting and IGC in a few discrete sites in the 5 and 10% pre-deformed samples. Moreover, the maximum corrosion depth and weight loss were significantly reduced. The result is summarized in Figure 5.2. The microstructure of T5 tempered and thereafter SHT 6005.40 is included in Figure 5.2, as the corrosion properties are highly dependent on microstructure [14, 86].

”T6 tempered” 6016 A and B were also SHT, pre-deformed by 10% rolling and aged in the same manner as 6005.40, to obtain a basis of comparison for the different alloys. It was evident, particularly from the micrographs of the 6016 B samples in section 4.3.1, that the IGC susceptibility was somewhat reduced as a consequence of pre-deformation for these samples as well. However, uniform etching and quite significant IGC/pitting occurred in the 10% pre-rolled samples, although they exhibited less IGC than the undeformed samples. Nevertheless, lower hardness values were measured for the 10% pre-rolled samples in relation to the undeformed samples as discussed in section 5.1, hence the pre-rolled samples

were likely to be overaged. This would greatly influence the corrosion properties [13, 91, 93–95].

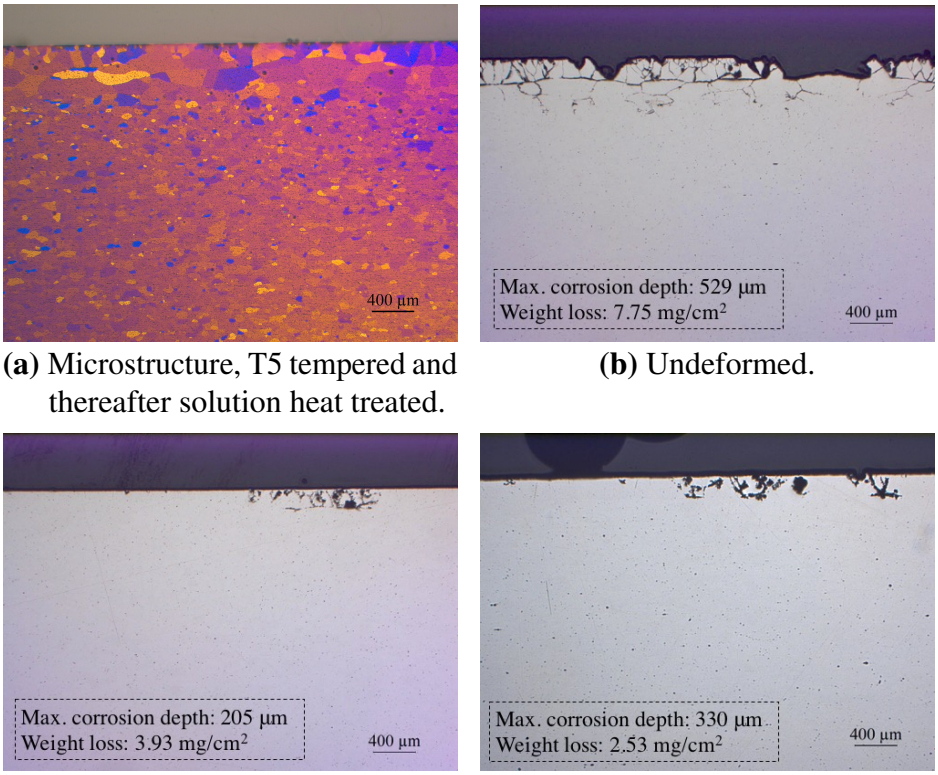

(a) Microstructure, T5 tempered and thereafter solution heat treated.

(b) Undeformed.

(c) 10% pre-rolled.

(d) 10% pre-stretched.

Figure 5.2: Comparison of optical micrographs of intergranular corrosion attacks in T6 tempered 6005.40. The microstructure of 6005.40 after T5 tempering and solution heat treatment is also displayed.

Precipitation in undeformed versus pre-deformed materials during ageing

Corrosion properties of aluminum alloys are highly dependent on alloy microstructure and thermomechanical treatment, and it is commonly agreed that AlMgSi alloys become sensitized to IGC during thermomechanical processing [13, 14, 20]. Shimizu et al. [19] found that the presence of a continuous, Cu rich, nanoscale film along the grain boundaries was crucial for deep-penetrating IGC to occur. Hence, it is reason to believe that improved resistance to IGC in pre-deformed 6005.40 is caused by rupture of the grain boundary film's continuity, formation of LAGBs on which the Cu rich film may not form, or any other circumstances which impede formation of the Cu rich grain boundary film.

According to the literature reviewed in section 2.4.3, the dislocations introduced during pre-deformation change how precipitation occurs in a material during ageing [25, 26, 81]. To illustrate the differences in precipitation behavior between undeformed and pre-deformed materials, the precipitation process in undeformed materials is firstly discussed.

After SHT and quenching of an undeformed material, alloying elements such as Mg, Si and

Cu exist homogeneously distributed in SSSS with a high concentration of vacancies [24, 53, 55]. This is illustrated in Figure 5.4a. The legend to Figure 5.4 and 5.5 is given in Figure 5.3. During ageing, the alloying elements diffuse to vacancies by vacancy diffusion and form clusters, which eventually grow into strengthening precipitates as illustrated in Figure 5.4b. Grain boundaries serve as fast diffusion paths for solutes, and alloying elements therefore tend to diffuse to the grain boundaries and precipitate during the ageing treatment. Moreover, the grain boundaries act as vacancy sinks, hence the amount of vacancies adjacent to the grain boundaries is limited. Since few vacancies exist in the zone along the grain boundaries, solute atoms would not form precipitates in that area, thus a PFZ arises as discussed in section 2.5.1 [24]. Furthermore, in several studies [13, 15, 18] a continuous, Cu rich film has been found to precipitate on the grain boundaries in Cu containing AlMgSi alloys, as the schematic illustration in Figure 5.4b displays. Microgalvanic coupling between the Cu rich film and the PFZ occurs if the material is exposed to corrosive media and the difference in electrochemical potential is sufficiently large [85]. Thus, extensive IGC may occur, as observed in the undeformed sample of 6005.40 in Figure 5.2b.

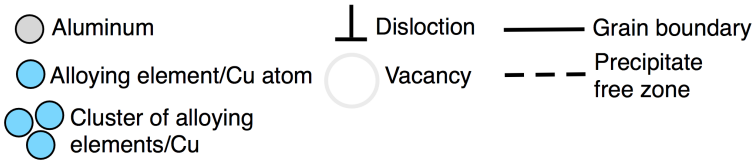

Figure 5.3: The legend to microstructure evolution during ageing of undeformed and pre-deformed AlMgSi alloys.

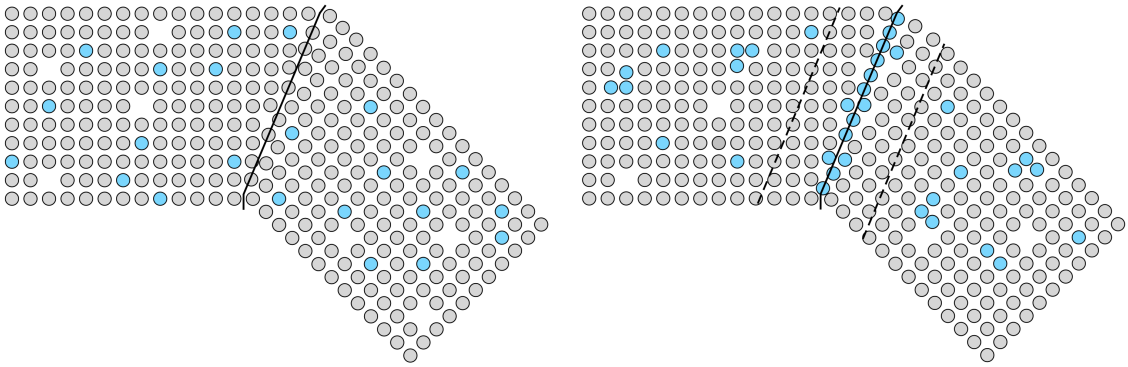

(a) Solution heat treated and quenched. **(b)** Artificially aged.

Figure 5.4: Schematic illustrations of microstructure in undeformed AlMgSi alloys before and after ageing.

However, it is believed that the microstructural changes during ageing of a pre-deformed material differ from the above description. Zhen et al. [25] and Teichmann et al. [26] discovered that dislocations, introduced during pre-deformation of a material, act as nucleation sites for precipitates during ageing. Hence, clustering of alloying elements occurs on dislocations during ageing of pre-deformed AlMgSi alloys. It was evident from the TEM image of the 10% pre-rolled sample in section 4.5.1 that precipitates had formed on dislocations

and that the number density of precipitates was much lower in this sample compared to in the undeformed sample. It is suggested that this may prevent the preferred precipitation of solute atoms, most importantly Cu, on the grain boundaries, which accordingly may reduce the susceptibility to IGC.

The microstructure of a SHT, quenched and pre-deformed material is illustrated in Figure 5.5a. Alloying elements exist in SSSS in matrix and dislocations occur on preferred slip planes [53]. The vacancy concentration is considerably reduced in the pre-deformed material in relation to the undeformed material, because dislocations serve as vacancy sinks [60]. Consequently, a PFZ will surround the dislocations after ageing as demonstrated in Figure 5.5b, correspondingly to the PFZ along the grain boundaries [26]. During ageing, the alloying elements diffuse to dislocations by dislocation pipe diffusion and form precipitates [25, 80]. The lower number of quenched-in vacancies significantly reduces the formation of clusters on vacancies, formed by vacancy diffusion [60]. Formation of a continuous, Cu rich film on the grain boundaries may be impeded as a result of preferred precipitation on dislocations, as illustrated in Figure 5.5b. Zhang et al. [102] found that a special pre-deformation procedure produced smaller PFZs and discontinuous precipitates along the grain boundaries in an AlCuMg alloy, providing less corrosion susceptibility. The observed effect was attributed to a highly homogeneous distribution of dislocations in the material which accordingly caused a homogeneous distribution of precipitates. This pre-deformation procedure included both rolling and stretching of the same sample, and was therefore not equal to the ones used in this work. However, it demonstrates that presence of dislocations and preferred precipitation on dislocations may result in improved corrosion resistance.

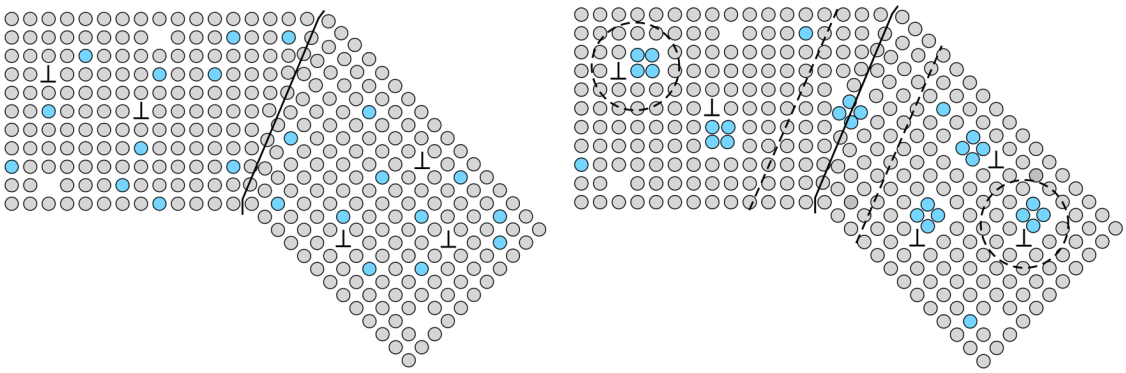

(a) Solution heat treated, quenched and pre-deformed.

(b) Artificially aged.

Figure 5.5: Schematic illustrations of suggested microstructure in pre-deformed AlMgSi alloys before and after ageing.

Furthermore, dislocation rich materials are found to promote precipitation of post-β'' phases [26, 83]. As elaborated in section 2.4.3, Teichmann et al. [26] attributed this to the lower number of quenched-in vacancies in pre-deformed materials, which consequently impedes formation of β''. Yassar et al. [83] found that β' and Q' precipitates were formed on dislocations instead of β'' in a pre-deformed AlMgSi alloy with 0.06 wt% Cu. The HAADF-STEM images in section 4.5.2 revealed that there was an unambiguous difference between

precipitates formed in undeformed and 10% pre-rolled 6005.40. In the undeformed sample β″/disordered precipitates with some Cu atomic columns in the disordered regions were observed. On the other hand, disordered Q′/B′ precipitates were observed in the pre-rolled sample. These precipitates displayed higher number of Cu atomic columns, and hence were able to incorporate more Cu. The fact that the predominating precipitates in pre-deformed materials are able to incorporate more Cu in relation to the predominating precipitates in undeformed materials, might be of highly importance for the IGC susceptibility. This means that less Cu is available for formation of a Cu rich film on the grain boundaries in pre-deformed materials. Thus, the formation of a continuous, internal cathode along the grain boundaries, which is found to be the reason for deep-penetrating IGC in AlMgSi(Cu) alloys [13, 15, 18, 19] may be avoided.

The EDS mapping of a presumably HAGB in 10% pre-rolled 6005.40 in section 4.5.3 did however reveal what looked like a continuous, Cu rich film along the grain boundary, but a Cu depleted zone along the grain boundary was hard to discern and in any case very narrow. Currently unpublished studies of Calin D. Marioara[1] have revealed comparable results as in the present work. In his studies, Marioara examined the effect of different ageing temperatures on corrosion properties and grain boundary chemistry of an equivalent 6005.40 alloy as herein. The alloy aged for 2 h at 205°C was resistant to IGC, whereas the alloy aged for 2 h at 185°C was highly susceptible. Cu elemental maps of a grain boundary in each alloy are displayed in Figure 5.6, as well as the Cu elemental map of the grain boundary in the 10% pre-rolled 6005.40 sample studied in this work. Although the IGC resistance was highly different for these samples, a Cu rich film is discernible along the grain boundary in all samples. Moreover, a distinct Cu depleted zone along the grain boundary is hard to recognize in all samples. It is therefore difficult to draw conclusions regarding the IGC susceptibility based on the elemental maps. Nevertheless, it is believed that any heat treatment, for instance overageing, or deformation that promotes precipitation of phases which incorporate more Cu, would result in improved IGC resistance.

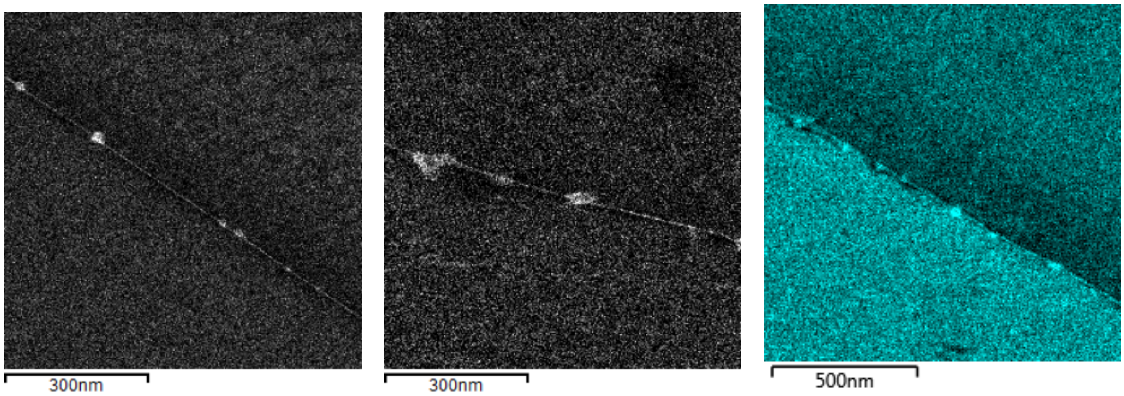

(a) Aged 2 h at 185°C. **(b)** Aged 2 h at 205°C. **(c)** 10% pre-rolled and aged 5 h at 185°C.

Figure 5.6: Comparison of Cu elemental maps from energy dispersive X-ray spectroscopy mapping of grain boundaries in 6005.40 alloys subjected to different thermo-mechanical treatments.

[1] SINTEF, Materials and Chemistry, Trondheim

Larger amounts of Cu incorporated into the precipitates in pre-deformed 6005.40 is presumably attributable to the lower activation energy for diffusion of solutes in dislocation rich materials. Cu has lower diffusivity in the aluminum matrix in relation to the other alloying elements Si and Mg [15]. Consequently, it requires longer time at elevated temperature for Cu to diffuse and become incorporated into the precipitates compared to Si and Mg. However, since less energy is required for diffusion of solutes in pre-deformed and dislocation rich materials, the diffusion rate of Cu is higher and incorporation of Cu into the precipitates can occur after shorter ageing time. Thus, more Cu is incorporated into the precipitates in pre-deformed 6005.40 in relation to undeformed 6005.40 at peak ageing.

Transition to pitting-like corrosion

A great reduction in extent of corrosion was evident in 6005.40 as a consequence of pre-deformation. However, also a change in corrosion mode was observed. Figure 5.7 displays that there is a transition from IGC to more pitting-like corrosion in pre-deformed 6005.40 samples in relation to the undeformed sample. This transition was also considerable for pre-deformed C28, studied in the specialization project [28]. The result of examinations of C28 is presented in Appendix A.

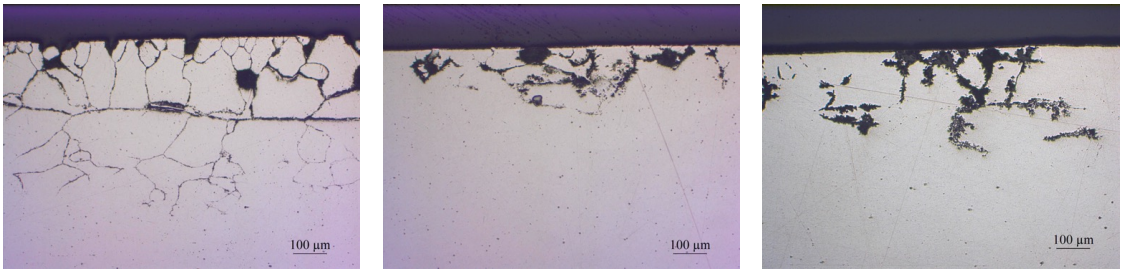

(a) Undeformed. **(b)** 10% pre-rolled. **(c)** 10% pre-stretched.

Figure 5.7: Comparison of optical micrographs of corrosion attacks in T6 tempered 6005.40. A transition from intergranular corrosion to pitting-like corrosion is observed as a consequence of pre-deformation.

Pitting susceptibility in AlMgSi alloys was elaborated in section 2.5.2. Research states that large precipitates or particles influence pitting susceptibility by introducing heterogeneity in the protective oxide film and acting as initiation sites for pitting [13, 91, 103, 104]. Several studies have shown that AlMgSi alloys become susceptible to pitting in overaged temper due to coarsening of matrix precipitates [13, 91, 93–95]. Dislocations are found to accelerate precipitation kinetics in pre-deformed materials due to lower activation energy for diffusion of solutes in dislocation rich materials [26, 60, 80]. As a consequence, coarser precipitates have been observed in pre-deformed materials compared to undeformed materials in several studies [25, 26]. From the examinations of 6005.40 in HAADF-STEM, it was possible to discern somewhat larger precipitates formed on dislocations in the pre-deformed sample compared to in the undeformed sample. Coarser precipitates cause larger fractions of alloying elements to be incorporated into the precipitates. Accordingly, the matrix becomes more depleted of alloying elements in pre-deformed materials in relation to in undeformed

materials. Hence, the electrochemical potential difference between the precipitates and matrix becomes larger in pre-deformed materials, whereas the electrochemical potential difference between the PFZ along the grain boundaries and the matrix becomes less pronounced. This increases the driving force for pitting, while the driving force for IGC is reduced [13, 15].

Considering that pre-deformation causes coarser precipitates and post-β'' phases frequently form on dislocations, the precipitate structure in pre-deformed materials presumably is quite similar to that in overaged materials. As mentioned, it is found in research that overaged materials are susceptible to pitting since the coarse matrix precipitates act as initiation sites for pits [13, 91, 93–95]. However, it is important to emphasis that pre-deformed 6005.40 did not overage, although pitting and coarser precipitates were observed in this sample. The hardness measurements revealed that the hardness of 6005.40 was independent of whether the material was pre-deformed or not, hence a decline in hardness was not observed for this alloy, as in overaged alloys. Strain hardening contributes to hardness in the pre-deformed material and compensates for the lower age hardening response [77]. In fact, Saito et al. [105] observed delayed overageing in an AlMgSi alloy due to pre-deformation, although the precipitation kinetics were initially faster.

Nevertheless, as can be seen in Figure 5.7, the corrosion mode in pre-deformed 6005.40 is a combination of IGC and pitting, not exclusively pitting as observed in overaged temper in for instance the study of Svenningsen et al. [13]. It is possible that corrosion in susceptible areas in both undeformed and pre-deformed 6005.40 initially propagates as IGC from minor pits at the surface, promoted by external cathodes. The precipitates in pre-deformed materials contain more Cu than in undeformed materials, and during corrosion the less noble constituents of the Cu containing precipitates are leached out. As a consequence, the precipitates become enriched in Cu, which may cause effective cathodic reactions facilitating cavity widening and pitting-like corrosion in pre-deformed materials.

Formation of subgrains with low angle grain boundaries

An important aspect in the discussion of how dislocations influence precipitation during ageing and in turn corrosion properties, is that the dislocations become annihilated during ageing or form subgrains with lower energy [78, 79]. Hence, the high dislocation density immediately after deformation will be considerably reduced during ageing. Furu et al. [79] found that the dislocation density was reduced from $5 \cdot 10^{14}$ m^{-2} to $2 \cdot 10^{14}$ m^{-2} subsequent to peak ageing of AA6005, pre-deformed 10%. However, clustering of solute atoms on dislocations occurs initially during ageing, before the dislocation density is significantly reduced [25, 26]. It is therefore reason to believe that the presence of dislocations is important for how precipitation occurs. Teichmann et al. [106] discovered that precipitates were formed on dislocations after only 10 min ageing at 190°C.

Nevertheless, the process of annihilation of dislocations and formation of low energy configurations, which is termed recovery and was detailed in section 2.4.2, may also influence corrosion performance. A proposed hypothesis in this work was that deformation could increase the number of LAGBs and reduce the number of HAGBs on the surface of the

material, thus reduce the danger of IGC. Minoda et al. [11] discovered that grain boundary precipitates and PFZs only existed along HAGBs in an AA6016 alloy, not along LAGBs. Yang et al. [27] documented that Cu free pre-β''/β'' precipitated on LAGBs, whereas Cu containing Q′/Q phases precipitated on HAGBs, making HAGBs more susceptible to corrosion. Both studies imply that attaining more LAGBs in the material would be beneficial for corrosion properties.

EBSD in SEM of the sample surface was performed to study the grain boundary misorientation angles in undeformed and deformed 6005.40, and the result was presented in section 4.4.2. The undeformed sample exhibited predominantly HAGBs and the fraction of LAGBs was only 0.105. On the other hand, deformation bands with LAGBs were unambiguously evident in the 10% pre-rolled sample in the direction of rolling. The fraction of LAGBs in this sample was 0.680. Hence, it is reason to believe that pre-deformation not only affects corrosion properties by altering the precipitation during ageing, but also affects the grain structure in a beneficial manner considering that less IGC susceptible precipitates or no precipitates at all are found to form on LAGBs. However, a grain structure with HAGBs was also apparent in the pre-rolled sample and it should be noted that the total length of HAGBs in the pre-rolled sample actually was slightly greater than the total length of HAGBs in the undeformed sample. Hence, the IGC susceptible area in the pre-rolled sample is expected to be similar to that in the undeformed sample. Accordingly, the importance of the changes in precipitation during ageing that pre-deformation promotes, becomes more evident.

Initiation sites for corrosion

Large areas on the surface of both pre-rolled and pre-stretched 6005.40 were found to be resistant to corrosion. However, in a few areas the corrosion had propagated as IGC and pitting in the interior of the material. Corrosion in AlMgSi alloys usually initiates as small pits on the metal surface [16]. Some mV below the E_c of a given alloy, metastable pits nucleate on the surface but largely repassivate. Stable pits are formed above E_c. However, it is found that the number of metastable pits on the surface is proportional to the number of stable pits that subsequently form and grow into deeper corrosion attacks [107]. Kairy et al. [107] found that there exists a critical precipitate thickness, above which the precipitates contribute to metastable pit formation and hence corrosion of the alloy. Below this critical thickness the precipitates do not act as individual entities but are incorporated into the electrochemical behavior of the aluminum matrix [107].

It is expected that more precipitates are above the critical thickness in pre-deformed materials, considering that coarser precipitates are found to occur in pre-deformed alloys [25, 26] and that coarser precipitates were found herein in 10% pre-rolled 6005.40 in relation to in undeformed 6005.40. Thus, fewer corrosion attacks in the pre-deformed materials are in contradiction to expectations based on the study of Kairy et al. [107]. However, numerous factors influence the corrosion behavior of AlMgSi alloys, hence there may be other reasons for fewer corrosion attacks in pre-deformed materials.

Coarse, primary α particles on the metal surface containing noble elements like Fe, have been found to act as initiation sites for corrosion in AlMgSi alloys [19, 100]. The amount

and distribution of these particles may have significant effect on corrosion behavior [108]. The primary α particles in the different 6005.40 samples were examined in backscatter mode in SEM, and the result was reported in section 4.4.1. It was not possible to detect any difference in distribution of α particles between the undeformed and the deformed samples. Thus, based on these images, it is not believed that pre-deformation affects the particles so that corrosion is initiated in fewer sites. It is possible, however, that it arises turbulence around the primary particles during deformation and that there will be higher density of dislocations around the particles. Precipitates may therefore form at the periphery of the particles during ageing, which accordingly may affect the initiation of corrosion. The result of EDS analysis of a primary α particle in 10% pre-rolled 6005.40, displayed in section 4.5.3, revealed that precipitates containing Mg, Si and Cu occurred on the particle periphery. However, it is not possible to assert if this is unique for the pre-deformed sample, considering that EDS mapping was not performed on the undeformed sample due to time constraints. Nevertheless, the effect this potentially may have is difficult to predict, but it might affect initiation of corrosion and also pitting susceptibility. It is not in any case believed that this turbulence around the primary particles would result in fewer initiation sites for corrosion.

It probably is a relatively large degree of formation of minor pits on the surface of pre-deformed alloys that could have been revealed during potentiodynamic polarization scans, considering that the circumstances which have been shown to initiate corrosion in AlMgSi alloys are present in the pre-deformed materials. However, since only a few corrosion attacks were apparent in the optical micrographs of the pre-deformed 6005.40 samples, these pits repassivate to larger extent in pre-deformed materials compared to undeformed materials. This is presumably due to the aforementioned changes in precipitation during ageing of a pre-deformed material or the formation of subgrains with LAGBs.

5.4.2 Pre-deformation subsequent to pre-baking

It was observed in this work that the influence of pre-deformation on corrosion properties was dependent on heat treatment before and after deformation. 6005.40, 6016 A and 6016 B discussed in the previous section were pre-deformed after SHT, without allowing any natural ageing to occur before deformation. Nonetheless, another set of 6016 samples was pre-deformed after pre-baking, that is a short ageing treatment to facilitate precipitation and accelerate the following paint baking. Formation of clusters which transform into hardening precipitates during ageing occurs during pre-baking [61].

The effect of pre-deformation, particularly stretching, was detrimental for the corrosion properties of paint baked 6016 A. This is evident from the micrographs in Figure 4.9 and 4.10 in section 4.3.1. The undeformed and 10% pre-stretched 6016 A samples, as well as the microstructure of the pre-baked alloy, are displayed in Figure 5.8 to illustrate the adverse effect of pre-deformation. The 6016 B samples were heavily corroded regardless of deformation. These results imply that pre-deformation has opposite effect on IGC resistance of materials deformed in pre-baked condition in relation to materials deformed in SHT condition.

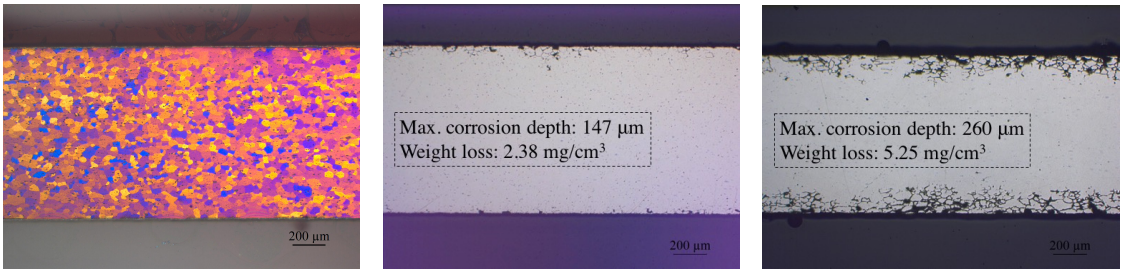

(a) Microstructure, pre-baked condition. **(b)** Undeformed. **(c)** 10% pre-stretched.

Figure 5.8: Comparison of optical micrographs of intergranular corrosion attacks in undeformed and 10% pre-stretched, paint baked 6016 A. The pre-stretched sample is evidently more susceptible to intergranular corrosion than the undeformed sample. The microstructure of pre-baked 6016 A is also shown. The scale bar is 200 µm on all images.

The pre-baked and successively pre-deformed 6016 alloys were aged to simulate the paint bake cycle used in the automotive industry, that is 20 min at 185°C, which means they were somewhat underaged. Larsen et al. [20] found that an AlMgSi alloy with 0.18 wt% Cu was most susceptible to IGC in underaged temper. However, 20% pre-deformation after SHT and water quenching improved the IGC resistance [20]. Somewhat improved IGC resistance was also observed for the ”T6 tempered” 6016 samples in which pre-deformation was conducted after SHT. Although the pre-deformed, ”T6 tempered” 6016 samples were overaged, it is reason to believe that the formation of clusters during pre-baking may be the adverse factor responsible for the detrimental effect of pre-deformation on IGC resistance of pre-baked 6016 A.

The clusters formed during pre-baking will presumably grow into strengthening precipitates during ageing. The grain boundaries act as vacancy sinks, and therefore a PFZ along the grain boundaries is expected. Hence, the precipitation process in pre-baked and subsequently pre-deformed materials may be quite similar to that in an undeformed material. However, the dislocations introduced during pre-deformation may also act as nucleation sites for precipitates [25, 26]. It is possible that the resulting distribution of precipitates increases the number of initiation sites for corrosion and hence results in higher IGC susceptibility. Furthermore, the dislocations themselves, remaining in the material after short ageing, may also act as initiation sites for corrosion considering that they may cause heterogeneities on the metal surface [99]. Zhen et al. [25] found considerably higher dislocation density in 5 and 10% pre-deformed AlMgSi alloys in relation to undeformed alloys after ageing for 30 min at 180°C. However, high dislocation density did not reduce the IGC resistance of the previously mentioned alloys examined by Larsen et al. [20]. The dislocation density was presumably higher in these materials in relation to the materials studied herein, since the degree of pre-deformation was larger.

Not only was there observed more initiation sites for corrosion in pre-deformed, paint baked 6016 A, but there was also found to be more profound corrosion, as can be seen in Figure 5.8. Hence, the combination of pre-baking and pre-deformation caused higher

IGC susceptibility of the grain boundaries inwards in the material as well. It is difficult to assess the microstructural changes which have caused the increased IGC susceptibility. Nevertheless, it is reason to believe that pre-baking and formation of clusters before pre-deformation are the decisive factors responsible for increased IGC susceptibility of pre-deformed, paint baked 6016 A, since improved IGC resistance has been observed herein and in other research [20] for materials pre-deformed after SHT. The Cu content in 6016 is negligible. It is therefore likely that external cathodes cause anodic dissolution of the grain boundaries [23]. Another possibility is that microgalvanic effects arise due to the electrochemical potential difference between the PFZ and matrix, considering that these alloys have greatly excess Si content. However, the exact corrosion mechanism in these materials remains unknown. TEM studies of the precipitates and grain boundary structure are required to obtain a better understanding of the corrosion properties of pre-baked and pre-deformed 6016 alloys.

Although pre-deformation after pre-baking had advantageous influence on the hardness values after paint baking, it is not recommended to implement this process in the automotive industry for AlMgSi alloys requiring good corrosion properties, based on the results herein. An alternative could be to pre-deform the materials before both pre-baking and paint baking, as then the problems with initial clustering and formation of precipitates on these clusters would vanish. Based on the results obtained in this work, it is reason to believe that the mentioned thermomechanical process could be beneficial for both mechanical and corrosion properties, especially for 6016 alloys containing Cu. Serizawa et al. [109] studied the effect of 5% pre-rolling before pre-baking of an AlMgSi alloy and found that this improved the age hardening response during paint baking. The hardness after pre-baking did not increase as a consequence of pre-deformation, hence optimum paint bake response was achieved. This is advantageous considering that it provides good formability during forming procedures. Moreover, precipitation of solute atoms occurred on dislocations in the pre-rolled material [109], which has been shown herein to presumably reduce IGC susceptibility. Improvement of IGC resistance due to pre-deformation is most effective for Cu containing AlMgSi alloys, but it was shown in the specialization project [28] that the IGC resistance of an essentially Cu free alloy was improved as well. Pre-deformation before pre-baking was not performed in this work due to time constraints and because the pre-baking procedure was performed at Hydro in Bonn.

Another alternative is to pre-deform the material instead of pre-baking it. Pre-deformation has the same effect as pre-ageing on suppressing natural ageing during storage, as dislocations act as vacancy sinks and hence prevent clustering of solute atoms on vacancies during natural ageing [60]. However, this process causes higher hardness before paint baking due to strain hardening, which may deteriorate the formability.

5.5 Effect of post-deformation on IGC susceptibility

The effect of post-deformation on IGC susceptibility of AlMgSi alloys was studied in this work. Post-deformation by rolling or stretching was performed on T6 tempered 6005.40 and C28, and the results were rather varying. Figure 5.9 and 5.10 reveal the different effects

of post-deformation on IGC of 6005.40 and C28, respectively. Shortly summarized, post-rolling of 6005.40 resulted in large areas without corrosion on the sample surface, whereas post-stretching had little effect on the IGC susceptibility, except that more grains detached from the surface. The susceptible areas in post-rolled 6005.40 exhibited profound IGC. Moreover, the IGC attacks occurred in vicinity of the edges of the samples and the edges were significantly corroded as well. Post-rolling of C28 caused very shallow and narrow, uniform IGC. Post-stretching had similar effects, although considerably more corrosion was observed in the post-stretched sample compared to the post-rolled sample, as can be seen in Figure 5.10.

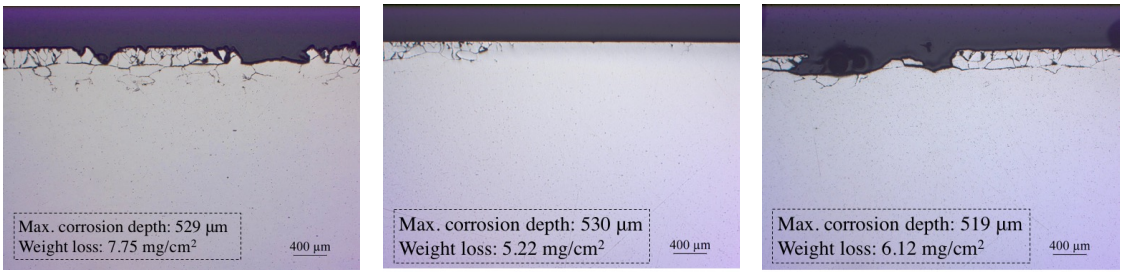

(a) Undeformed. **(b)** 10% post-rolled. **(c)** 10% post-stretched.

Figure 5.9: Comparison of optical micrographs of corrosion attacks in T6 tempered 6005.40 in undeformed and post-deformed condition.

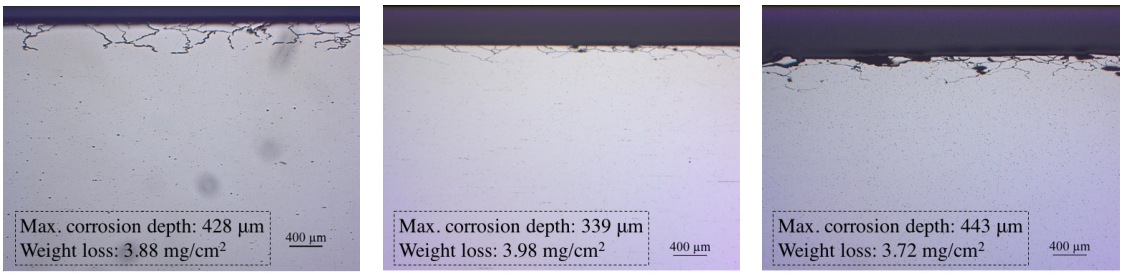

(a) Undeformed. **(b)** 10% post-rolled. **(c)** 10% post-stretched.

Figure 5.10: Comparison of optical micrographs of corrosion attacks in T6 tempered C28 in undeformed and post-deformed condition.

The beneficial effect of pre-deformation on IGC susceptibility was mostly attributed to a change in how precipitation occurs during ageing. In post-deformed materials, however, all precipitates are formed prior to the deformation. The precipitate distribution in post-deformed materials is therefore likely to be equal to that in an undeformed material. Hence, for the Cu containing 6005.40 and C28 alloys, a continuous, Cu rich film and an accompanying PFZ are expected along the grain boundaries after ageing. During post-deformation, dislocations are introduced in the material. Since there exist no strengthening precipitates in the PFZ, this zone is much weaker than the rest of the material. Thus, the deformation is concentrated in these zones. Although the general deformation of the material is low, the deformation of the PFZ along the grain boundaries becomes very large and microcracking may start to occur as dislocations pile up against the grain boundaries

[24]. These microcracks can serve as initiation sites for IGC during subsequent IGC testing, and grain detachment can take place as the weak PFZ is anodically dissolved. This theory may explain the corrosion mechanism in post-stretched 6005.40 and C28. It was evident from the micrographs that a lot of grains had detached from the post-stretched samples, particularly in 1 and 5% post-stretched 6005.40 seen in section 4.3.2, in which a 200 μm thick surface layer was nearly completely removed.

Nevertheless, it is apparent that post-rolling affects the microstructure of 6005.40 such that large areas on the sample surfaces become resistant to IGC. Furthermore, the microstructure of C28 is changed due to post-rolling, causing altered IGC morphology. It is possible that the electrochemical potential of the surface of the materials is affected by post-rolling. Afseth et al. [110] found that the corrosion potential of a cold rolled AlMn alloy was less negative compared to the corrosion potential of annealed samples in acidified, 5 wt% NaCl solution. It is therefore a possibility that the rolled surface of 6005.40 and C28 becomes more cathodic compared to the edges of the samples during IGC testing. Hence, the edges may act as some form of sacrificial anodes and be preferentially corroded, thus reducing the extent of corrosion on the surface of 6005.40 and C28. By comparing the edges in the undeformed and the 10% post-rolled 6005.40 sample, it was possible to observe a difference in extent of corrosion, in which the edges in the post-rolled sample were more heavily corroded. This was displayed in Figure 4.16 in section 4.3.2. Lam et al. [111] found that corrosion of edges in fibrous AlMgSi alloys significantly improved the IGC resistance of the surface of the samples. However, the surface became susceptible to corrosion when the edges were covered during IGC testing.

Another effect of post-rolling might be that the precipitate structure on the surface of the materials changes due to the large strains introduced on the surface during rolling. Research [112, 113] has shown that ultrafine-grained microstructures of AlCu and AlMgSi alloys, produced by severe plastic deformation, improved the IGC resistance of the alloys. The improved corrosion resistance of the AlCu alloy was attributed to desensitization of the grain boundaries through redistribution of Cu from the grain boundaries to other areas of the microstructure [112]. It is possible that a similar process occurs during post-rolling of 6005.40 and C28. However, it is questionable if 10% deformation can cause such great strains. Moreover, it was not possible to detect any differences in particle distribution on the surface of undeformed and post-deformed 6005.40 during backscatter imaging, displayed in section 4.4.1. The large, primary α particles were not even visibly broken into smaller pieces. Redistribution of Cu from grain boundaries to more favorable areas of the microstructure is therefore not very likely. On the other hand, the hardness after 10% post-rolling was more than 9 HV lower than the hardness after 10% post-stretching for 6005.40. The hardness contribution from age hardening is among others dependent on size and distribution of precipitates [24, 53, 70]. Hence, a change in precipitate properties might have occurred during post-rolling and not during post-stretching, considering the better mechanical response in the 10% post-stretched samples, but lower IGC resistance.

Formation of a subgrain structure with LAGBs also occurred in the post-deformed 6005.40 samples. The result from EBSD of 6005.40 in section 4.4.2 revealed that the grain structure of both post-rolled and post-stretched samples consisted of subgrains with LAGBs. It is however difficult to assess if this grain structure has affected the corrosion properties,

considering that the effect of post-stretching was rather different from the effect of post-rolling of particularly 6005.40.

5.6 The 6016 alloys

Large variations in corrosion properties were observed for 6016 A and 6016 B, subjected to different heat treatments. However, it was not within the scope of this master thesis to discuss these differences. Hence, all discussion concerning aspects other than the effect of deformation on mechanical and corrosion properties is omitted. Nevertheless, it should be noted that these alloys had significantly different corrosion properties although the chemistry of the alloys is quite similar.

5.7 Further work

The work performed in this master thesis has provided a better understanding of the corrosion mechanism in cold worked AlMgSi alloys, particularly pre-deformed materials. However, a lot of research remains to examine different aspects of deformation, for instance deformation of materials subjected to the special ageing treatment in the automotive industry and post-deformation.

Lack of EDS mapping of the undeformed 6005.40 sample in TEM makes it hard to evaluate the significance of the slightly discernible Cu rich film on the grain boundary in the 10% pre-rolled 6005.40 sample. EDS mapping of grain boundaries in the undeformed sample should therefore be performed and attempts should be made to quantify the amount of Cu on the grain boundaries in both samples.

As shown in this work, thermomechanical treatment is of highly importance for mechanical and corrosion properties. It is recommended that focus is directed towards optimizing the thermomechanical treatment of a given alloy, by for instance exploring different combinations of degree of pre-deformation, ageing temperature and ageing time, to achieve most favorable mechanical properties combined with highest corrosion resistance. Crash performance testing should also be performed along with corrosion testing to ensure that the pre-deformed alloys are suitable for use in automotive applications. Examination of the effect of pre-deformation of 6016 before pre-baking on mechanical and corrosion properties, is of particular interest. It is believed that this could be highly advantageous for corrosion properties and paint bake response. AA6016 is the primary choice of aluminum sheets among automotive manufacturers in Europe [41], and since the investments in aluminum for car body applications are increasing [6], efforts should be made to improve both mechanical and corrosion properties of these alloys. Corrosion testing, mechanical testing and TEM studies, to assess precipitate structure details and grain boundary composition, should be performed on 6016. Examinations of Cu containing 6016 alloys would also be interesting.

The effect of post-deformation on corrosion properties is still not understood. Potentiodynamic polarization and open circuit potential measurements could be performed on

post-rolled samples, especially 6005.40, to achieve clarity in whether post-rolling affects the corrosion potential of the surface. IGC testing of post-rolled samples with covered edges could also be performed to examine whether the surface becomes more susceptible to IGC when the edges are not corroded. TEM studies of the microstructure of post-deformed samples are required to better understand the corrosion mechanism in these alloys. It should be noted that post-deformation not is a common procedure in fabrication of aluminum alloys. Hence, further investigations of the effect of post-deformation on IGC susceptibility are of scientific value more than commercial value.

Finally, since corrosion mechanisms are hard to understand considering that important evidence is lost during corrosion, it would be interesting to perform in-situ experiments of for instance pre-deformed 6005.40 in TEM, to simultaneously study the microstructure and corrosion.

Chapter 6

Conclusion

The main objective of this study was to examine the effect of cold deformation on the IGC susceptibility of AlMgSi alloys with different chemistry. Pre- or post-deformation by rolling or stretching was performed on 6005.40, 6016 A, 6016 B and C28, subjected to thoroughly described heat treatments. Results from IGC testing revealed that it was possible with the appropriate thermomechanical treatment to achieve highly improved IGC resistance and satisfying mechanical properties for pre-deformed, Cu containing AlMgSi alloys. The favorable effect of pre-deformation on corrosion properties was attributed to that more Cu is incorporated into the precipitates in dislocation rich materials due to dislocation pipe diffusion, causing less Cu to be available for formation of the frequently reported continuous, Cu rich film along the grain boundaries. For the same reason a transition to pitting-like corrosion was observed in the pre-deformed materials.

However, the results also indicated that pre-deformation after pre-baking of materials used in the automotive industry had adverse influence on the corrosion properties, presumably due to formation of precipitates both on dislocations and on clusters formed during pre-baking. Based on results obtained in this work and other research [109], it is believed that pre-deformation prior to pre-baking may be advantageous for achieving optimum paint bake response combined with good corrosion properties, especially for Cu containing alloys.

Post-deformation had somewhat ambiguous effect on both mechanical and corrosion properties. Post-rolling reduced the IGC susceptibility of 6005.40 and altered the IGC morphology of C28, but did not noticeably increase the hardness of the alloys. Post-stretching, on the other hand, did not improve corrosion properties, but increased the hardness. Further examinations in electron microscope or electrochemical testing may contribute to a better understanding of corrosion properties of post-deformed alloys. However, post-deformation is not common in manufacturing of commercial aluminum alloys. Hence, further studies are of primarily scientific value.

Bibliography

[1] T. A. Boden, G. Marland, and R. J. Andres. *Global, Regional, and National Fossil-Fuel CO2 Emissions*. 2011. URL: http://cdiac.ornl.gov/trends/emis/tre_glob.html (Cited 03/30/2017).

[2] European Commission. *A European Strategy for low-emission mobility*. 2016. URL: http://ec.europa.eu/clima/policies/transport/index%7B%5C_%7Den.htm (Cited 10/10/2016).

[3] H. Helms, U. Lambrecht, and U. Höpfner. *Energy savings by light-weighting - Final report*. Tech. rep. Heidelberg, Germany: Institute for Energy- and Environmental Research, 2003.

[4] G. Aylward and T. Findlay. *SI Chemical Data*. 6th ed. Australia: John Wiley and Sons, 2008.

[5] J. Hirsch. "Recent development in aluminium for automotive applications." In: *Transactions of Nonferrous Metals Society of China* 24.7 (2014), pp. 1995–2002.

[6] Hydro Aluminium. *Hydro's new automotive line*. 2017. URL: http://www.hydro.com/en/press-room/hydros-new-automotive-line/ (Cited 05/13/2017).

[7] W. S. Miller et al. "Recent development in aluminium alloys for the automotive industry." In: *Materials Science and Engineering: A* 280.1 (2000), pp. 37–49.

[8] T. Sakurai. "The latest Trends in Aluminum Alloy Sheets for Automotive Body Panels." In: *Kobelco Technology Review* 28 (2008), pp. 22–28.

[9] J. Hirsch. "Aluminium in Innovative Light-Weight Car Design." In: *Materials Transactions* 52.5 (2011), pp. 818–824.

[10] R. Braun. "Investigation on Microstructure and Corrosion Behaviour of 6XXX Series Aluminium Alloys." In: *Aluminium Alloys 2006 - ICAA10*. Vol. 519. Vancouver, Canada: Trans Tech Publications, 2006, pp. 735–740.

[11] T. Minoda and H. Yoshida. "Effect of grain boundary characteristics on intergranular corrosion resistance of 6061 aluminum alloy extrusion." In: *Metallurgical and Materials Transactions A* 33.9 (2002), pp. 2891–2898.

[12] W. J. Liang et al. "General aspects related to the corrosion of 6xxx series aluminium alloys: Exploring the influence of Mg/Si ratio and Cu." In: *Corrosion Science* 76 (2013), pp. 119–128.

[13] G. Svenningsen et al. "Effect of artificial aging on intergranular corrosion of extruded AlMgSi alloy with small Cu content." In: *Corrosion Science* 48.6 (2006), pp. 1528–1543.

[14] G. Svenningsen et al. "Effect of low copper content and heat treatment on intergranular corrosion of model AlMgSi alloys." In: *Corrosion Science* 48.1 (2006), pp. 226–242.

[15] M. H. Larsen et al. "Intergranular Corrosion of Copper-Containing AA6xxx AlMgSi Aluminium Alloys." In: *Journal of The Electrochemical Society* 155.11 (2008), pp. C550–C556.

[16] K. Nisancioglu. “Corrosion Caused by Grain Boundary Segregation.” In: *Corrosion and Corrosion Protection (compendium)*. Norwegian University of Science and Technology, Trondheim, Norway, 2014. Chap. 12, pp. 1–9.

[17] J. R. Davis, ed. *Corrosion of Aluminum and Aluminum Alloys*. Ohio, United States: ASM International, 1999.

[18] S. K. Kairy et al. “Understanding the Origins of Intergranular Corrosion in Copper-Containing Al-Mg-Si Alloys.” In: *Metallurgical and Materials Transactions A* 47.3 (2016), pp. 985–989.

[19] K. Shimizu and K. Nisancioglu. “High Resolution SEM Investigation of Intercrystalline Corrosion on 6000-Series Aluminum Alloy with Low Copper Content.” In: *ECS Electrochemistry Letters* 3.9 (2014), pp. C29–C31.

[20] M. H. Larsen et al. *Effect of composition and thermomechanical history on intergranular corrosion of AlMgSi(Cu) alloys*. Tech. rep. Trondheim, Norway: Norwegian University of Science and Technology, 2010.

[21] G. Svenningsen et al. “Effect of high temperature heat treatment on intergranular corrosion of AlMgSi(Cu) model alloy.” In: *Corrosion Science* 48.1 (2006), pp. 258–272.

[22] G. Svenningsen et al. “Effect of thermomechanical history on intergranular corrosion of extruded AlMgSi(Cu) model alloy.” In: *Corrosion Science* 48.12 (2006), pp. 3969–3987.

[23] M. H. Larsen et al. “Effect of Excess Silicon and Small Copper Content on Intergranular Corrosion og 6000-Series Aluminium Alloys.” In: *Journal of The Electrochemical Society* 157.2 (2010), pp. C61–C68.

[24] J. K. Solberg. *Teknologiske metaller og legeringer*. Trondheim, Norway: Norwegian University of Science and Technology, 2014.

[25] L. Zhen and S. B. Kang. “Effect of predeformation on microstructure and tensile properties of Al-Mg-Si alloys with high silicon content.” In: *Materials Science and Technology* 14.4 (1998), pp. 317–321.

[26] K. Teichmann et al. “The Effect of Preaging Deformation on the Precipitation Behavior of an Al-Mg-Si Alloy.” In: *Metallurgical and Materials Transactions A* 43.11 (2012), pp. 4006–4014.

[27] W. Yang et al. “Grain boundary precipitation induced by grain crystallographic misorientations in an extruded Al–Mg–Si–Cu alloy.” In: *Journal of Alloys and Compounds* 624 (2015), pp. 27–30.

[28] J. Grønvold, T. Furu, and O. Lunder. “The Effect of Pre-deformation on Intergranular Corrosion of AlMgSi Alloys.” Project thesis. Norwegian University of Science and Technology, 2016.

[29] A. Deschamps, F. Livet, and Y. Brechet. “Influence of predeformation on ageing in an Al–Zn–Mg alloy — I. Microstructure evolution and mechanical properties.” In: *Acta Materialia* 47.1 (1998), pp. 281–292.

[30] G. E. Totten and D. S. MacKenzie, eds. *Handbook of Aluminum - Volume 1: Physical Metallurgy and Processes*. New York, United States: CRC Press, 2003.

[31] J. T. M. de Hosson, M. de Haas, and S. M. van Scherpenzeel. “Grain Boundary Segregation and Precipitation in Aluminium Alloy AA6061.” In: *Aluminium Alloys*

2006 - ICAA10. Vol. 519. Vancouver, Canada: Trans Tech Publications, 2006, pp. 467–472.

[32] J. R. Davis, ed. *Metals Handbook*. 2nd ed. Ohio, United States: ASM International, 1998.

[33] C. Kammer, ed. *Aluminium Handbook - Fundamentals and Materials*. 1st ed. Düsseldorf, Germany: Aluminium-Verlag Marketing & Kommunikation GmbH, 1999.

[34] J. G. Kaufman. *Introduction to Aluminum Alloys and Tempers*. Ohio, United States: ASM International, 2000.

[35] I. Polmear, D. St. John, and V. Ravi. *Light Alloys: From Traditional Alloys to Nanocrystals*. 4th ed. Oxford, England: Butterworth-Heinemann, 2006.

[36] J. E. Hatch, ed. *Aluminium: Properties and Physical Metallurgy*. Ohio, United States: ASM International, 1984.

[37] Sapa Group. *Extruded Aluminum, Alloy 6005/6105*. URL: https://www.sapagroup.com/contentassets/7a0f14a8e10a42d0b2ad96f818fe1c25/data_sheet_6005_6105_new_metric_02_22_2017.pdf (Cited 01/29/2017).

[38] Sapa Group. *Extruded Aluminum, Alloy 6082*. URL: https://www.sapagroup.com/contentassets/7a0f14a8e10a42d0b2ad96f818fe1c25/data_sheet_6082_new_metric_02_22_2017_rev.pdf (Cited 01/29/2017).

[39] K. Widlic. *New alloy for safer cars*. 2014. URL: http://www.sapagroup.com/en/newswall/shape/2014/shape2/technology/learn-and-create/ (Cited 09/28/2016).

[40] U. Tundal et al. *Al-Mg-Si aluminium alloy with improved properties*. 2013. URL: http://www.google.com/patents/WO2013162374A1?cl=en (Cited 09/28/2016).

[41] J. Bottema et al. "Developments in AA6016 Aluminium Type Body Sheet Product." In: *International Congress and Exposition*. Detroit, USA: SAE International, 1998.

[42] Hydro Aluminum. *Strip and sheet for body*. 2016. URL: http://www.hydro.com/en/products/Rolled-products/Strip-and-sheet-for-automotive/Aluminium-strip-and-sheet-for-Body/ (Cited 03/13/2017).

[43] D. R. Askeland and P. P. Phulé. *The Science and Engineering of Materials*. 4th ed. Pacific Grove, California: Thomson Brooks/Cole, 2003.

[44] G. Gottstein. "Physical Metallurgy - Fundamentals of Through-Process Modelling." In: *Virtual Fabrication of Aluminium Products. Microstructural Modeling in Industrial Aluminium Fabrication Processes*. Ed. by J. Hirsch. WILEY-VCH Verlag GmbH & Co, 2006, pp. 85–110.

[45] S. K. Fjeldbo et al. "Through-process sensitivity analysis on the effect of process variables on strength in extruded Al–Mg–Si alloys." In: *Journal of Materials Processing Technology* 212.1 (2012), pp. 171–180.

[46] The Aluminum Association. *Rolling Aluminum: From the Mine Through the Mill*. Arlington, United States: The Aluminum Association, 1990.

[47] P. K. Saha. *Aluminium Extrusion Technology*. Ohio, United States: ASM International, 2000.

[48] W. Z. Misiolek, S. R. Claves, and D. L. Elias. "Analysis of the Intermetallic Phase Transformation Occurring during Homogenization of 6xxx Aluminum Alloys." In: *8th International Conference on Aluminium Alloys*. Vol. 396. Oxford, England: Trans Tech Publications, 2002, pp. 667–674.

[49] S. Zajac et al. “Microstructure control and extrudability of Al-Mg-Si alloys microalloyed with manganese.” In: *Journal de Physique IV Colloque* (1993), pp. C7–251–C7–254.

[50] The International Aluminium Institute. *Aluminium for Future Generations - Rolling*. 2017. URL: `http://primary.world-aluminium.org/processes/rolling/` (Cited 03/13/2017).

[51] K. Siegert, G. Sauer, and M. Bauser. *Extrusion*. 2nd ed. Ohio, United States: ASM International, 2006.

[52] K. Lee and K. Woo. “Effect of the hot-rolling microstructure on texture and surface roughening of Al-Mg-Si series aluminum alloy sheets.” In: *Metals and Materials International* 17.4 (2011), p. 689.

[53] W. D. Callister and D. G. Rethwisch. *Materials Science and Engineering*. 8th ed. John Wiley and Sons, 2011.

[54] C. D. Marioara et al. “Improving thermal stability in Cu-containing Al-Mg-Si alloys by precipitate optimization.” In: *Metallurgical and Materials Transactions A* 45.7 (2014), pp. 2938–2949.

[55] C. D. Marioara et al. “The influence of alloy composition on precipitates of the Al-Mg-Si system.” In: *Metallurgical and Materials Transactions A* 36.3 (2005), pp. 691–702.

[56] K. Strobel et al. “Relating Quench Sensitivity to Microstructure in 6000 Series Aluminium Alloys.” In: *Materials Transactions* 52.5 (2011), pp. 914–919.

[57] L. Cao, P. A Rometsch, and M. J Couper. “Clustering behaviour in an Al–Mg–Si–Cu alloy during natural ageing and subsequent under-ageing.” In: *Materials Science and Engineering: A* 559 (2013), pp. 257–261.

[58] J. Asensio-Lozano, B. Suárez-Peña, and G. V. Voort. “Effect of Processing Steps on the Mechanical Properties and Surface Appearance of 6063 Aluminium Extruded Products.” In: *Materials* 7.6 (2014), pp. 4224–4242.

[59] J. Zhang et al. “Equilibrium pseudobinary Al–Mg2Si phase diagram.” In: *Materials Science and Technology* 17.5 (2001), pp. 494–496.

[60] M. Kolar. “The Effect of Pre-deformation on Precipitation and Mechanical Properties during Ageing of Al-Mg-Si Alloys.” Doctoral dissertation. Norwegian University of Science and Technology, 2011.

[61] Y. Birol. “Pre-aging to improve bake hardening in a twin-roll cast Al–Mg–Si alloy.” In: *Materials Science and Engineering: A* 391.1–2 (2005), pp. 175–180.

[62] M. H. Larsen. “Effect of Composition and Thermomechanical Processing on The Intergranular Corrosion of AA6000 Aluminium Alloys.” Doctoral dissertation. Norwegian University of Science and Technology, 2010.

[63] Y. Ji, F. Guo, and Y. Pan. “Microstructural characteristics and paint-bake response of Al-Mg-Si-Cu alloy.” In: *Transactions of Nonferrous Metals Society of China* 18.1 (2008), pp. 126–131.

[64] M. Murayama et al. “The effect of Cu additions on the precipitation kinetics in an Al-Mg-Si alloy with excess Si.” In: *Metallurgical and Materials Transactions A* 32.2 (2001), pp. 239–246.

[65] C. D. Marioara et al. “The effect of Cu on precipitation in Al–Mg–Si alloys.” In: *Philosophical Magazine* 87.23 (2007), pp. 3385–3413.

[66] G. A. Edwards et al. “The precipitation sequence in Al–Mg–Si alloys.” In: *Acta Materialia* 46.11 (1998), pp. 3893–3904.

[67] K. Marthinsen et al. “Work Hardening Behaviour of Heat-Treatable Al-Mg-Si-Alloys.” In: *Aluminium Alloys 2006 - ICAA10*. Vol. 519. Vancouver, Canada: Trans Tech Publications, 2006, pp. 1901–1906.

[68] L. Ding et al. “The natural aging and precipitation hardening behaviour of Al-Mg-Si-Cu alloys with different Mg/Si ratios and Cu additions.” In: *Materials Science and Engineering: A* 627 (2015), pp. 119–126.

[69] S. P. Ringer and K. Hono. “Microstructural Evolution and Age Hardening in Aluminium Alloys: Atom Probe Field-Ion Microscopy and Transmission Electron Microscopy Studies.” In: *Materials Characterization* 44.1–2 (2000), pp. 101–131.

[70] R. E. Smallman and A. H. W. Ngan. *Modern Physical Metallurgy*. 8th ed. Oxford, England: Butterworth-Heinemann, 2014.

[71] K. Matsuda et al. “Precipitation sequence of various kinds of metastable phases in Al-1.0mass% Mg2Si-0.4mass% Si alloy.” In: *Journal of Materials Science* 35.1 (2000), pp. 179–189.

[72] J. Holmestad et al. “Investigation of Grain Boundaries in an Al-Mg-Si-Cu Alloy.” In: *Aluminium Alloys 2014 - ICAA14*. Vol. 794. Trondheim, Norway: Trans Tech Publications, 2014, pp. 951–956.

[73] K. Matsuda et al. “Metastable phases in an Al-Mg-Si alloy containing copper.” In: *Metallurgical and Materials Transactions A* 32.6 (2001), pp. 1293–1299.

[74] D. J. Chakrabarti and D. E. Laughlin. “Phase relations and precipitation in Al–Mg–Si alloys with Cu additions.” In: *Progress in Materials Science* 49.3–4 (2004), pp. 389–410.

[75] Total Materia. *Strengthening Mechanisms of Metals: Part Two*. 2008. URL: `http://www.totalmateria.com/page.aspx?ID=CheckArticle%7B%5C&%7Dsite=ktn%7B%5C&%7DLN=DA%7B%5C&%7DNM=193` (Cited 03/13/2016).

[76] A. M. A. Mohamed and F. H. Samuel. “A Review on the Heat Treatment of Al-Si-Cu/Mg Casting Alloys.” In: *Heat Treatment - Conventional and Novel Applications*. Ed. by F. Czerwinski. InTech, 2012. Chap. 4.

[77] M. Kolar et al. “Effect of Pre-Deformation on Mechanical Response of an Artificially Aged Al-Mg-Si Alloy.” In: *Materials Transactions* 52.7 (2011), pp. 1356–1362.

[78] F. Humphreys and M. Hatherly. *Recrystallization and Related Annealing Phenomena*. 2nd ed. Oxford, England: Elsevier, 2004.

[79] T. Furu, Ø. Ryen, and O. R. Myhr. “Effect of pre-deformation on age hardening kinetics in commercial 6xxx alloys.” In: *11th International Conference on Aluminium Alloys*. Aachen, Germany: Wiley-VCH, 2008, 1626-1633.

[80] H. Mehrer. *Diffusion in Solids - Fundamentals, Methods, Materials, Diffusion-Controlled Processes*. Heidelberg, Germany: Springer Berlin Heidelberg, 2007.

[81] T. Saito et al. “The Effects of Low Cu Additions and Predeformation on the Precipitation in a 6060 Al-Mg-Si Alloy.” In: *Metallurgical and Materials Transactions A* 44.9 (2013), pp. 4124–4135.

[82] G. K. Quainoo and S. Yannacopoulos. “The effect of cold work on the precipitation kinetics of AA6111 aluminum.” In: *Journal of Materials Science* 39.21 (2004), pp. 6495–6502.

[83] R. S. Yassar, D. P. Field, and H. Weiland. “The effect of predeformation on the β" and β' precipitates and the role of Q´ phase in an Al–Mg–Si alloy; {AA6022}.” In: *Scripta Materialia* 53.3 (2005), pp. 299–303.

[84] J. Dutkiewicz and L. Litynska. “The effect of plastic deformation on structure and properties of chosen 6000 series aluminium alloys.” In: *Materials Science and Engineering: A* 324.1–2 (2002), pp. 239–243.

[85] C. Vargel. *Corrosion of Aluminium*. Amsterdam, Netherlands: Elsevier, 2004.

[86] K. Nisancioglu. “Corrosion of Aluminium and Aluminium Alloys.” In: *Corrosion and Corrosion Protection (compendium)*. Norwegian University of Science and Technology, Trondheim, Norway, 2014. Chap. 25, pp. 1–17.

[87] M. Bloeck and P. Furrer. “Vermeidung von Korrosionproblemen bei Aluminiumwerkstoffen.” In: *Materials and Corrosion* 46 (1995), pp. 622–627.

[88] International Standard. *ISO 11846:1995. Corrosion of metals and alloys - Determination of resistance to intergranular corrosion of solution heat-treatable aluminium alloys*. 1995.

[89] T. Minoda and H. Yoshida. “The Effect of Microstructure on Intergranular Corrosion Resistance of 6061 Alloy Extrusion.” In: *Aluminium Alloys - Their Physical and Mechanical Properties*. Vol. 331. Virginia, United States: Trans Tech Publications, 2000, pp. 1689–1694.

[90] F. Zeng et al. “Corrosion mechanism associated with Mg2Si and Si particles in Al–Mg–Si alloys.” In: *Transactions of Nonferrous Metals Society of China* 21.12 (2011), pp. 2559–2567.

[91] V. Guillaumin and G. Mankowski. “Influence of Overaging Treatment on Localized Corrosion of Al 6056.” In: *Corrosion* 56.1 (2000).

[92] J. Holmestad et al. *TEM studies of the effect of different Mg/Si-ratios on intergranular corrosion of Al-Mg-Si-Cu alloys*. Tech. rep. Trondheim, Norway: Norwegian University of Science and Technology, 2015.

[93] K. Yamaguchi and K. Tohma. “Effect of Zn addition on intergranular corrosion resistance of Al-Mg-Si-Cu.” In: *Proceeding of the 6th international Conference on Aluminium Alloys (ICAA6)*. Vol. 3. Toyohashi, Japan: The Japan Institute of Light Metals, 1998, pp. 1657–1662.

[94] R. Dif et al. “6056 T78: a corrosion resistant copper-rich 6XXX alloy for aerospace applications.” In: *Proceeding of the 6th international Conference on Aluminium Alloys (ICAA6)*. Vol. 3. Toyohashi, Japan: Japan Institute of Light Metals, 1998, pp. 1991–1996.

[95] K. El-Menshawy et al. “Effect of aging time at low aging temperatures on the corrosion of aluminum alloy 6061.” In: *Corrosion Science* 54 (2012), pp. 167–173.

[96] X. Sheng et al. “Effect of artificial ageing on intergranular corrosion of 6005A Al alloy.” In: *The Chinese Journal of Nonferrous Metals* 22.8 (2012).

[97] V. G. Davydov et al. “Influence of SSTT, Ageing Regime and Stretching on IGC, Complex of Properties and Precipitation Behavior of 6013 Alloy.” In: *Aluminium Alloys - Their Physical and Mechanical Properties*. Vol. 331. Materials Science Forum. Virginia, United States: Trans Tech Publications, 2000, pp. 1315–1320.

[98] K. Nisancioglu. “Pitting Corrosion.” In: *Corrosion and Corrosion Protection (compendium)*. Norwegian University of Science and Technology, Trondheim, Norway, 2014. Chap. 11, pp. 1–12.

[99] Z. Szklarska-Smialowska. “Pitting corrosion of aluminum.” In: *Corrosion Science* 41.9 (1999), pp. 1743–1767.

[100] J. Malina and J Radosevic. “Influence of NaCl concentration on pitting corrosion of extruded Al-Mg-Si alloy AA6060.” In: *Zastita Materijala* 56 (2015), pp. 47–51.

[101] Y. Birol. “Pre-straining to improve the bake hardening response of a twin-roll cast Al–Mg–Si alloy.” In: *Scripta Materialia* 52.3 (2005), pp. 169–173.

[102] X. Zhang et al. “Effect of pre-deformation of rolling combined with stretching on stress corrosion of aluminum alloy 2519A plate.” In: *Transactions of Nonferrous Metals Society of China* 22.1 (2012), pp. 8–15.

[103] C. Blanc and G. Mankowski. “Susceptibility to pitting corrosion of 6056 aluminium alloy.” In: *Corrosion Science* 39.5 (1997), pp. 949–959.

[104] V. Guillaumin and G. Mankowski. “Localized corrosion of 6056 {T6} aluminium alloy in chloride media.” In: *Corrosion Science* 42.1 (2000), pp. 105–125.

[105] T. Saito et al. “Aberration-corrected HAADF-STEM investigations of precipitate structures in Al–Mg–Si alloys with low Cu additions.” In: *Philosophical Magazine* 94.5 (2014), pp. 520–531.

[106] K. Teichmann et al. “HRTEM study of the effect of deformation on the early precipitation behaviour in an AA6060 Al–Mg–Si alloy.” In: *Philosophical Magazine* 91.28 (2011), pp. 3744–3754.

[107] S. K. Kairy et al. “Exploring the electrochemistry of 6xxx series aluminium alloys as a function of Si to Mg ratio, Cu content, ageing conditions and microstructure.” In: *Electrochimica Acta* 190 (2016), pp. 92–103.

[108] Y. Wu and H. Liao. “Corrosion Behavior of Extruded near Eutectic Al–Si–Mg and 6063 Alloys.” In: *Journal of Materials Science & Technology* 29.4 (2013), pp. 380–386.

[109] A. Serizawa, T. Sato, and M. K. Miller. “Effect of cold rolling on the formation and distribution of nanoclusters during pre-aging in an Al–Mg–Si alloy.” In: *Materials Science and Engineering: A* 561 (2013), pp. 492–497.

[110] A. Afseth et al. “Effect of thermo-mechanical processing on filiform corrosion of aluminium alloy {AA3005}.” In: *Corrosion Science* 44.11 (2002), pp. 2491–2506.

[111] P. V. T. Lam, T. Furu, and O. Lunder. “Intergranular Corrosion of Extruded AlMgSi(Cu,Zn) Alloys.” Master thesis. Norwegian University of Science and Technology, 2016.

[112] J. G. Brunner et al. “Impact of ultrafine-grained microstructure on the corrosion of aluminium alloy {AA2024}.” In: *Corrosion Science* 57 (2012), pp. 209–214.

[113] B. Wielage et al. “Corrosion Characteristics of an Ultrafine-Grained Al-Mg-Si Alloy (AA6082).” In: *Nanomaterials by Severe Plastic Deformation IV*. Vol. 584. Materials Science Forum. Goslar, Germany: Trans Tech Publications, 2008, pp. 988–993.

Appendix A

Microstructure and corrosion properties of C28

The microstructure and corrosion properties of C28 were investigated in the specialization project, conducted by the author during fall 2016 [28]. The results obtained are summarized in the following sections, as they are of importance for the work conducted in this master thesis.

A.1 Microstructure of C28

In Figure A.1a the microstructure of as-extruded C28 is displayed. The microstructure appears highly fibrous in the center region in the direction of the extrusion. A recrystallized layer with random texture and average depth of 300 µm is observed at the surface of the extrudate. However, as can be observed in Figure A.1b, the SHT and thereafter T6 tempered and IGC tested sample is fully recrystallized with large, elongated grains in the bulk region. This microstructure is more representative for the C28 samples which are IGC tested in this work.

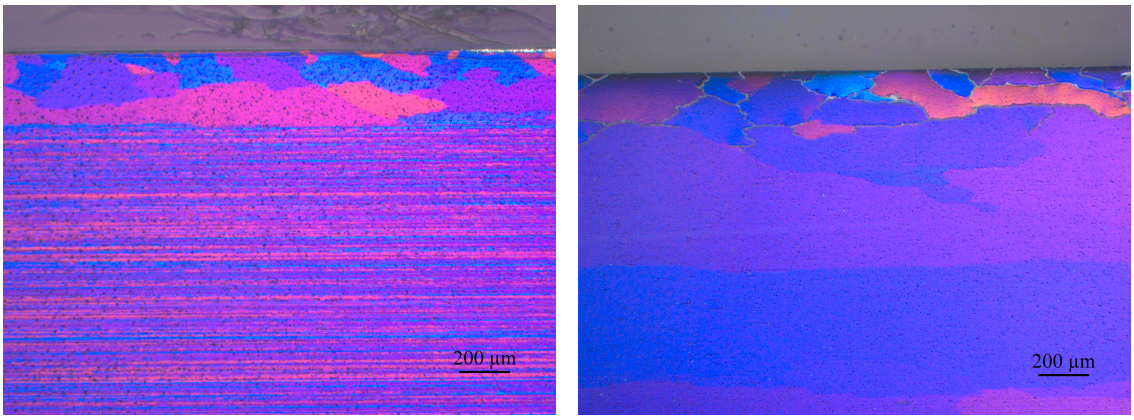

(a) As-extruded.

(b) Solution heat treated, T6 tempered and IGC tested.

Figure A.1: Optical micrographs showing microstructure in cross-sectional area of C28. The view plane is parallel to the extrusion direction. The scale bar is 200 µm on both micrographs.

A.2 Accelerated IGC testing

An accelerated IGC test was carried out according to ISO 11846 (method B) in the same manner as herein. The view plane during metallographic examinations in LM was equal to the view plane in this work, that is the cross-sectional area parallel to the extrusion direction.

A.2.1 Effect of pre-rolling of C28 on IGC

Micrographs of C28, pre-deformed to different levels by rolling and subsequently aged to T6 temper, are presented in Figure A.2. The corrosion parameters are summarized in Table A.1. The undeformed sample exhibits severe, uniform IGC. The corrosion attacks are confined to localized IGC and pitting at 1% pre-rolling, but with relatively many initiation sites.

Further reduction in corrosion attacks is observed in the 5% pre-rolled sample, as can be seen in Figure A.2e. The predominating corrosion mode is local pitting for this sample. At 10% pre-rolling the maximum corrosion depth is considerably reduced, but the corrosion attacks are rather wide with quite a few initiation sites. The weight losses measured for the 5 and 10% pre-rolled samples are relatively large.

Table A.1: Corrosion parameters after intergranular corrosion testing of pre-rolled and subsequently T6 tempered C28.

Deformation	**Corrosion mode**	**Max. corrosion depth [μm]**	**Weight loss [mg/cm^2]**
0%	Uniform IGC (360 μm)	428	3.88
1%	Local IGC and pitting (80-270 μm)	326	2.97
5%	Local pitting (70-150 μm)	268	3.79
10%	Local pitting (50-100 μm)	130	3.65

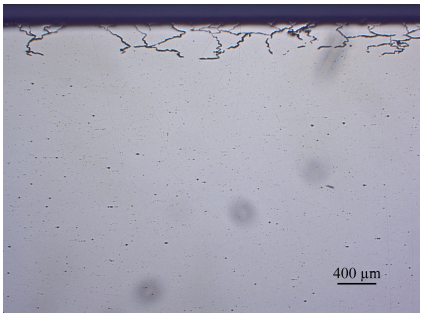

(a) Undeformed.

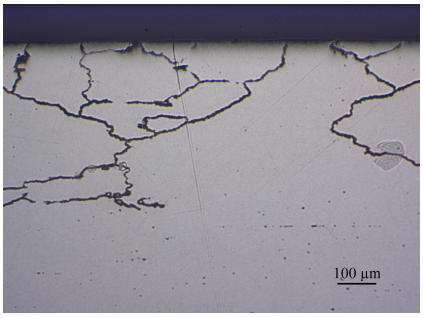

(b) Undeformed.

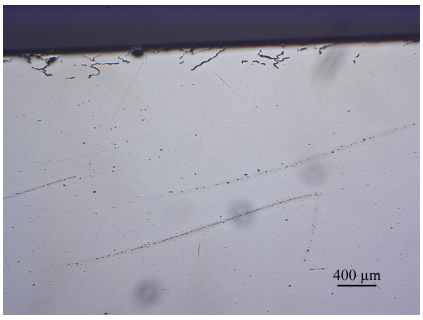

(c) 1% pre-rolled.

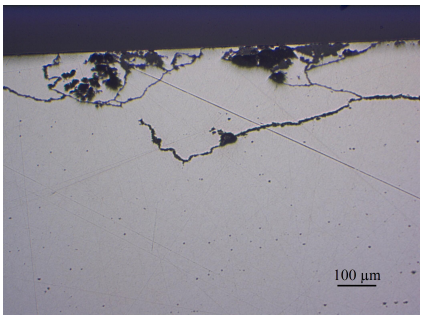

(d) 1% pre-rolled.

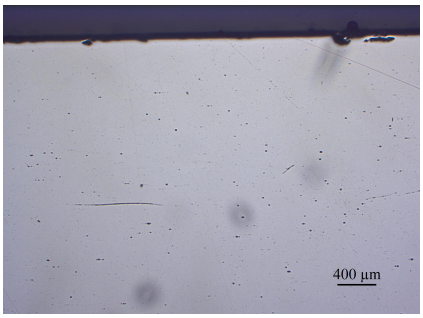

(e) 5% pre-rolled.

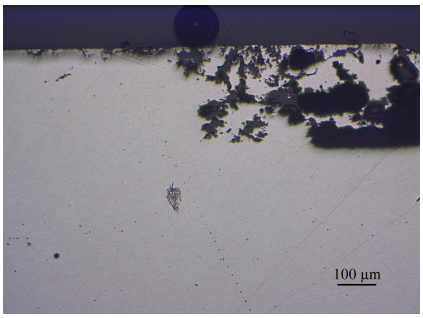

(f) 5% pre-rolled.

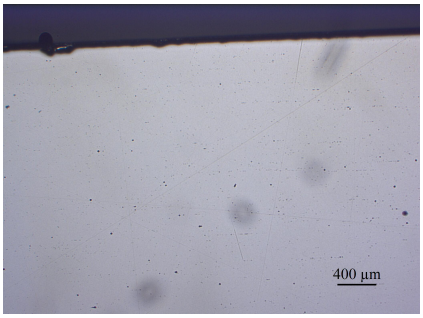

(g) 10% pre-rolled.

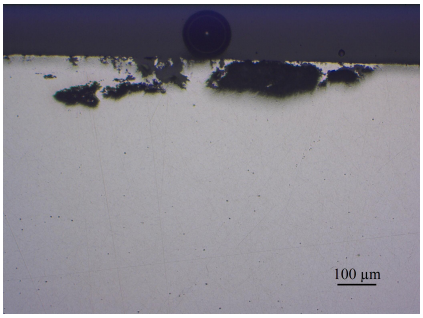

(h) 10% pre-rolled.

Figure A.2: Optical micrographs of cross section parallel to extrusion direction of pre-rolled, subsequently T6 tempered and corrosion tested C28. Figure (a), (c), (e) and (g) show corrosion attacks in representative areas. Figure (b), (d), (f) and (h) show the most severe attacks.

A.2.2 Effect of pre-stretching of C28 on IGC

Micrographs of C28, pre-deformed to different levels by stretching and subsequently aged to T6 temper, are presented in Figure A.3. The corrosion parameters are summarized in Table A.2. A slightly reduction in corrosion attacks is observed in the 1% pre-stretched sample in relation to the undeformed sample. At 5 and 10% pre-stretching, pitting becomes the predominating corrosion mode, as for the pre-rolled samples. The number of initiation sites is however higher for the pre-stretched samples and uniform pitting is observed in the 10% pre-stretched sample. Hence, in light of the optical micrographs, pre-rolling of C28 results in better corrosion resistance than stretching does. However, weight loss measurements indicate the opposite, as larger mass losses were measured for the pre-rolled samples.

Table A.2: Corrosion parameters after intergranular corrosion testing of pre-stretched and subsequently T6 tempered C28.

Deformation	**Corrosion mode**	**Max. corrosion depth [μm]**	**Weight loss [mg/cm^2]**
0%	Uniform IGC (360 μm)	428	3.88
1%	Uniform IGC and pitting (200-370 μm)	375	3.39
5%	Local pitting (100-250 μm)	272	2.04
10%	Uniform pitting (50-200 μm)	235	2.35

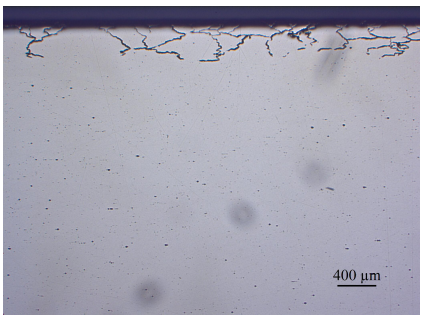

(a) Undeformed.

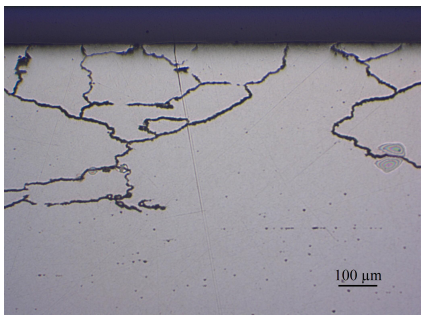

(b) Undeformed.

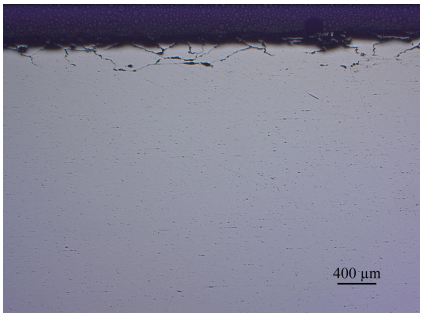

(c) 1% pre-stretched.

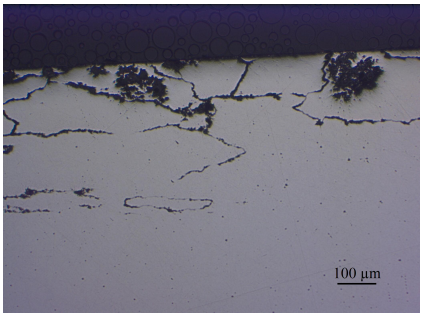

(d) 1% pre-stretched.

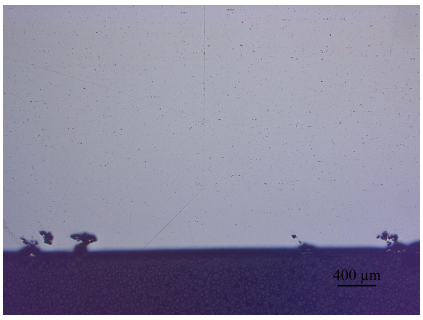

(e) 5% pre-stretched.

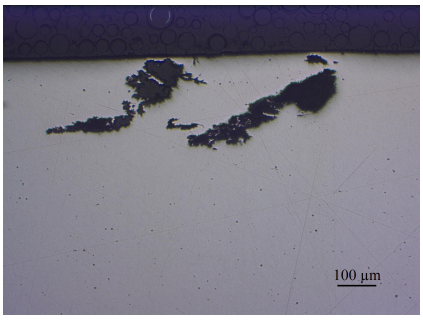

(f) 5% pre-stretched.

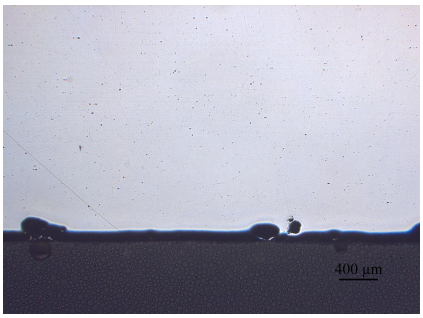

(g) 10% pre-stretched.

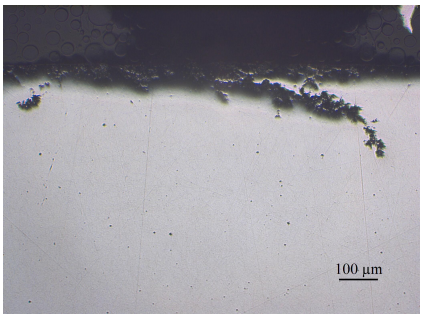

(h) 10% pre-stretched.

Figure A.3: Optical micrographs of cross section parallel to extrusion direction of pre-stretched, subsequently T6 tempered and corrosion tested C28. Figure (a), (c), (e) and (g) show corrosion attacks in representative areas. Figure (b), (d), (f) and (h) show the most severe attacks. The scale bar is 400 µm in Figure (a), (c), (e) and (g).

Appendix B

Formula for calculating amount of Si available for Mg_2Si

In equation B.1 the formula for calculating Si amount available for formation of Mg_2Si is displayed. The Si amount available is calculated by subtracting the amount of Si which is incorporated into particles and dispersoids containing Fe, Mn and Cr.

$$\text{Wt\% Si available for } Mg_2Si = \text{wt\% Si} - \frac{\text{wt\% Fe} + \text{wt\% Mn} + \text{wt\% Cr}}{3} \tag{B.1}$$

Appendix C

Stress-strain curves for stretched materials

The recorded stress-strain curves during pre- and post-stretching of 6005.40, 6016 A, 6016 B and C28 are displayed in Figure C.1 to C.4, respectively. Pre-stretching was performed before the final ageing treatments, whereas post-stretching was performed afterwards.

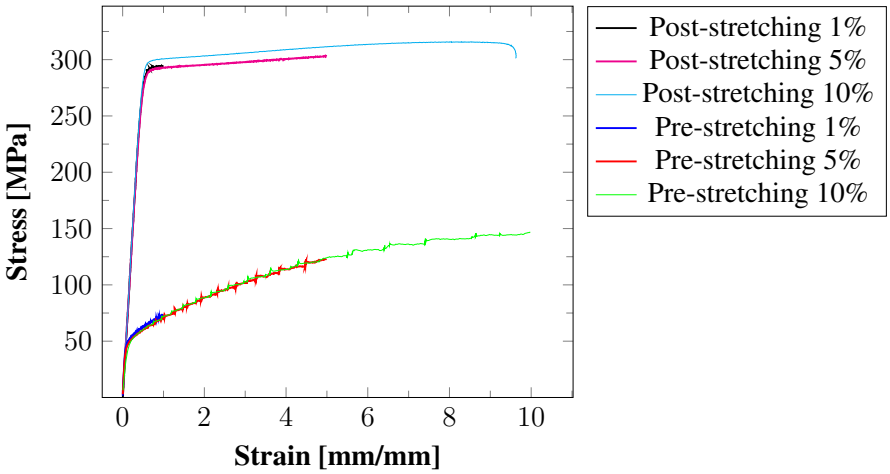

Figure C.1: Stress-strain curves for 6005.40, stretched 1, 5 and 10% before and after ageing.

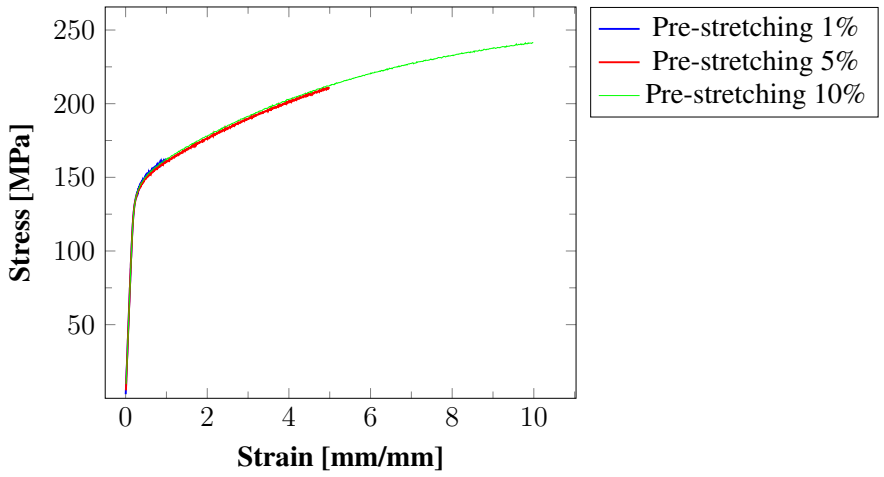

Figure C.2: Stress-strain curves for 6016 A, stretched 1, 5 and 10% before ageing.

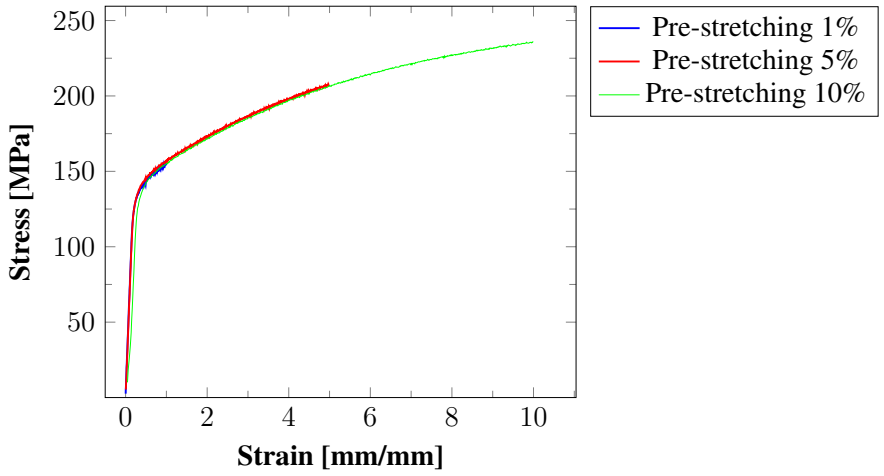

Figure C.3: Stress-strain curves for 6016 B, stretched 1, 5 and 10% before ageing.

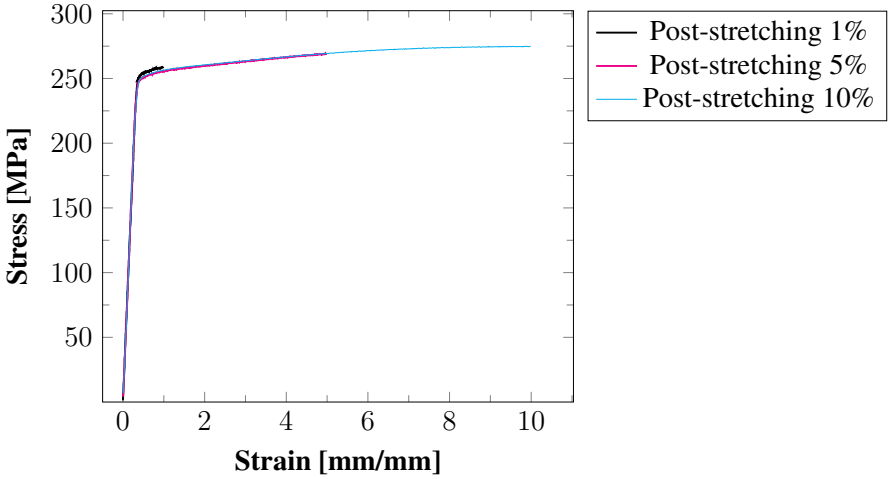

Figure C.4: Stress-strain curves for C28, stretched 1, 5 and 10% after ageing.

Appendix D

Vickers hardness measurements

In the following tables average values and standard deviations for hardness measurements on 6005.40, 6016 A, 6016 B and C28 are displayed. Five indentations were made on each sample. Table D.1 and D.2 present hardness measurements before and after ageing for pre-rolling and pre-stretching, respectively. Table D.3 and D.4 present hardness measurements after ageing for post-rolling and post-stretching, respectively.

Table D.1: Vickers hardness measurements (HV1) before and after ageing of different alloys deformed by pre-rolling. SHT = solution heat treated.

Alloy	**Degree of pre-rolling**	**Avg. hardness before ageing [HV1]**	**St. dev.**	**Avg. hardness after ageing [HV1]**	**St. dev**
6005.40	0%	45.0	1.58	101	2.55
	1%	48.0	1.22	101	3.03
	5%	60.2	1.30	98.6	2.19
	10%	66.0	3.16	98.6	2.88
6016 A, pre-baked, deformed, paint baked	0%	69.4	2.79	84.4	1.82
	1%	73.6	1.34	86.6	3.44
	5%	85.6	1.95	95.4	1.67
	10%	93.0	2.55	92.6	2.70
6016 A, SHT, deformed, T6 tempered	0%	45.8	0.84	96.6	2.07
	10%	67.2	0.84	88.2	1.48
6016 B, pre-baked, deformed, paint baked	0%	73.0	1.00	83.4	2.07
	1%	74.3	1.92	82.2	3.49
	5%	86.8	2.39	89.6	2.88
	10%	92.2	2.17	92.2	1.79
6016 B, SHT, deformed, T6 tempered	0%	40.8	1.79	82.2	1.30
	10%	57.4	1.34	78.4	2.70

Table D.2: Vickers hardness measurements (HV1) before and after ageing of different alloys deformed by pre-stretching.

Alloy	Degree of pre-stretching	Avg. hardness before ageing [HV1]	St. dev.	Avg. hardness after ageing [HV1]	St. dev
6005.40	0%	45.0	1.58	101	2.55
	1%	42.4	1.82	103	2.86
	5%	48.2	1.48	104	2.17
	10%	54.0	2.35	100	2.00
6016 A, pre-baked, deformed, paint baked	0%	69.4	2.79	84.4	1.82
	1%	71.0	1.58	87.2	2.39
	5%	86.2	1.79	90.2	1.64
	10%	85.6	1.95	91.4	1.67
6016 B, pre-baked, deformed, paint baked	0%	73.0	1.00	83.4	2.07
	1%	73.4	1.14	78.0	2.92
	5%	80.4	2.07	82.0	1.87
	10%	85.4	3.58	89.8	1.64

Table D.3: Vickers hardness measurements (HV1) after ageing of different alloys deformed by post-rolling.

Alloy	Degree of post-rolling	Avg. hardness [HV1]	St. dev.
6005.40	0%	101	2.55
	1%	105	2.05
	5%	100	3.65
	10%	99.8	4.21
C28	0%	107	2.41
	1%	104	2.79
	5%	106	1.87
	10%	109	2.51

Table D.4: Vickers hardness measurements (HV1) after ageing of different alloys deformed by post-stretching.

Alloy	Degree of post-stretching	Avg. hardness [HV1]	St. dev.
6005.40	0%	101	2.55
	1%	101	2.61
	5%	110	3.29
	10%	109	4.38
C28	0%	107	2.41
	1%	105	1.87
	5%	111	2.61
	10%	113	1.79

Appendix E

Grain boundary misorientation histograms of 6005.40

In Figure E.1 grain boundary misorientation histograms of T6 tempered 6005.40 are presented. Histogram of the undeformed, 10% pre-rolled, 10% post-rolled and 10% post-stretched sample is displayed in Figure E.1a to E.1d, respectively. It is apparent that the deformed samples exhibit significantly higher fractions of LABGs in relation to the undeformed sample.

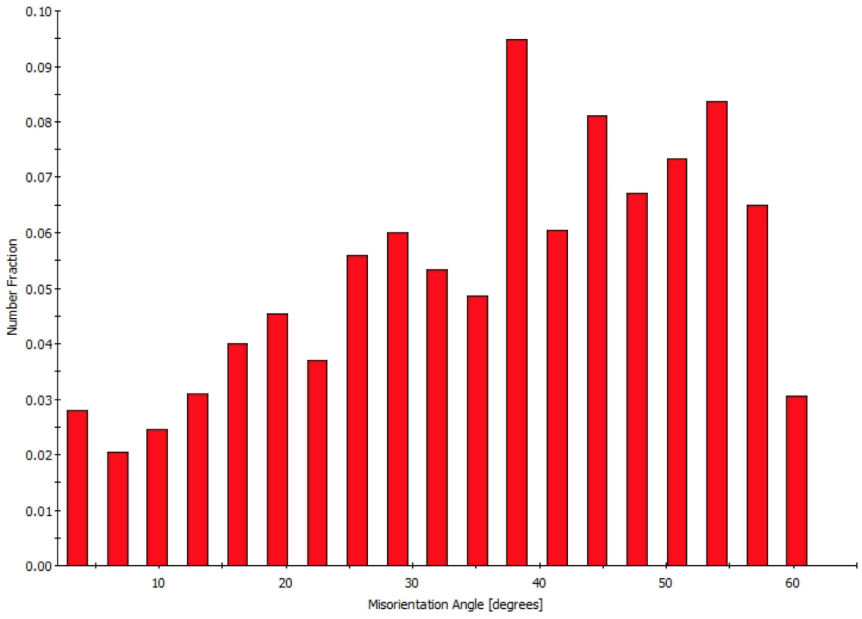

Angle [degrees]	Number Fraction
3.575	0.0280207
6.725	0.0204082
9.875	0.0244574
13.025	0.0309362
16.175	0.0400065
19.325	0.0453515
22.475	0.037091
25.625	0.0558795
28.775	0.0600907
31.925	0.053288
35.075	0.0485909
38.225	0.0947522
41.375	0.0604146
44.525	0.0811467
47.675	0.0670554
50.825	0.0733722
53.975	0.0837383
57.125	0.0649498
60.275	0.0304503
63.425	0
Average Number	36.5268

(a) Undeformed.

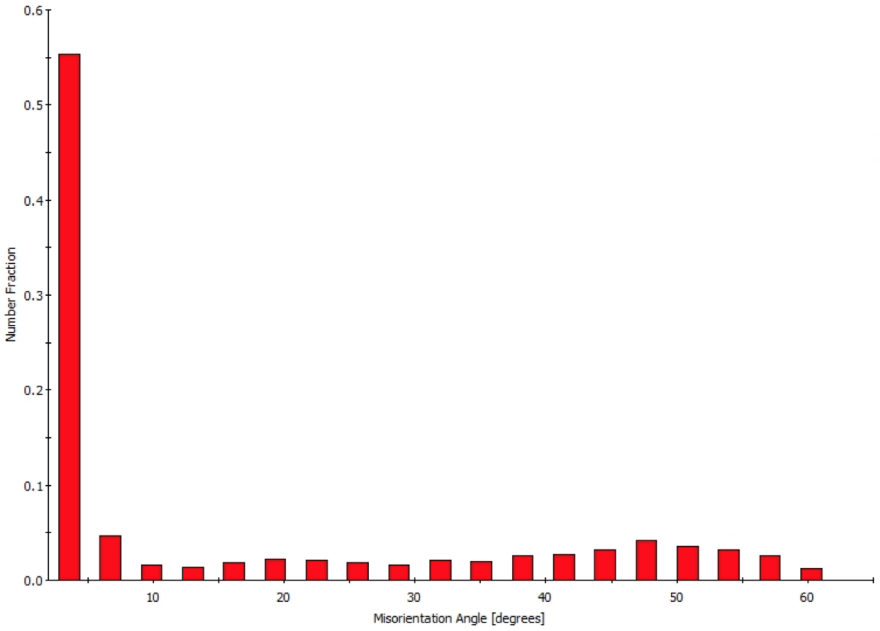

Angle [degrees]	Number Fraction
3.575	0.552998
6.725	0.046915
9.875	0.0156591
13.025	0.0137251
16.175	0.0179674
19.325	0.0226465
22.475	0.0207125
25.625	0.019028
28.775	0.0160958
31.925	0.0208372
35.075	0.020151
38.225	0.0252667
41.375	0.0273879
44.525	0.0316302
47.675	0.0423607
50.825	0.0359973
53.975	0.0323164
57.125	0.0260153
60.275	0.0121655
63.425	0.000124774
Average Number	17.05

(b) 10% pre-rolled.

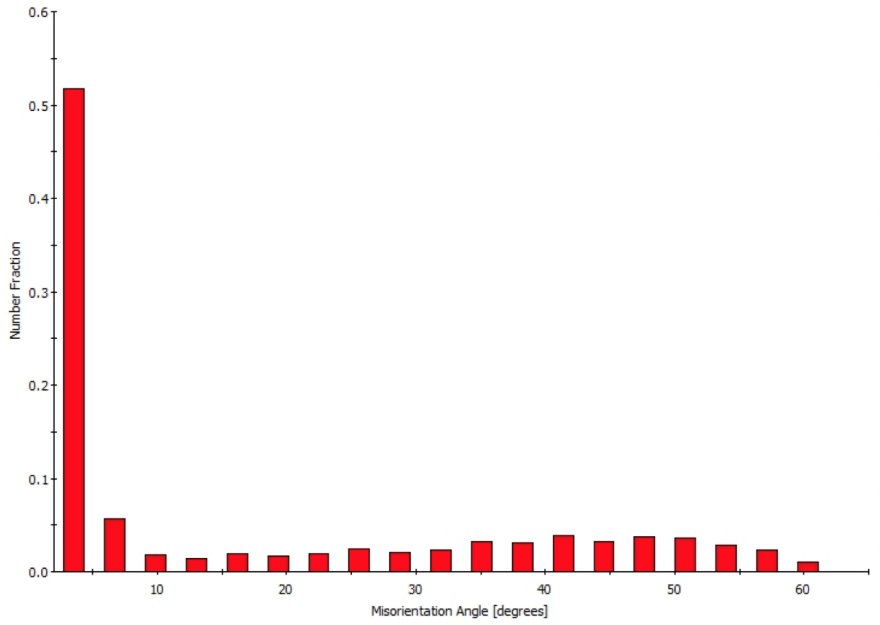

Angle [degrees]	Number Fraction
3.575	0.517906
6.725	0.0562305
9.875	0.0182558
13.025	0.0144393
16.175	0.0196552
19.325	0.0168564
22.475	0.0187647
25.625	0.0240443
28.775	0.0210546
31.925	0.0228993
35.075	0.0325043
38.225	0.0309777
41.375	0.0384199
44.525	0.0326951
47.675	0.0379111
50.825	0.0356848
53.975	0.0285605
57.125	0.0231537
60.275	0.00998664
63.425	0
Average Number	17.7158

(c) 10% post-rolled.

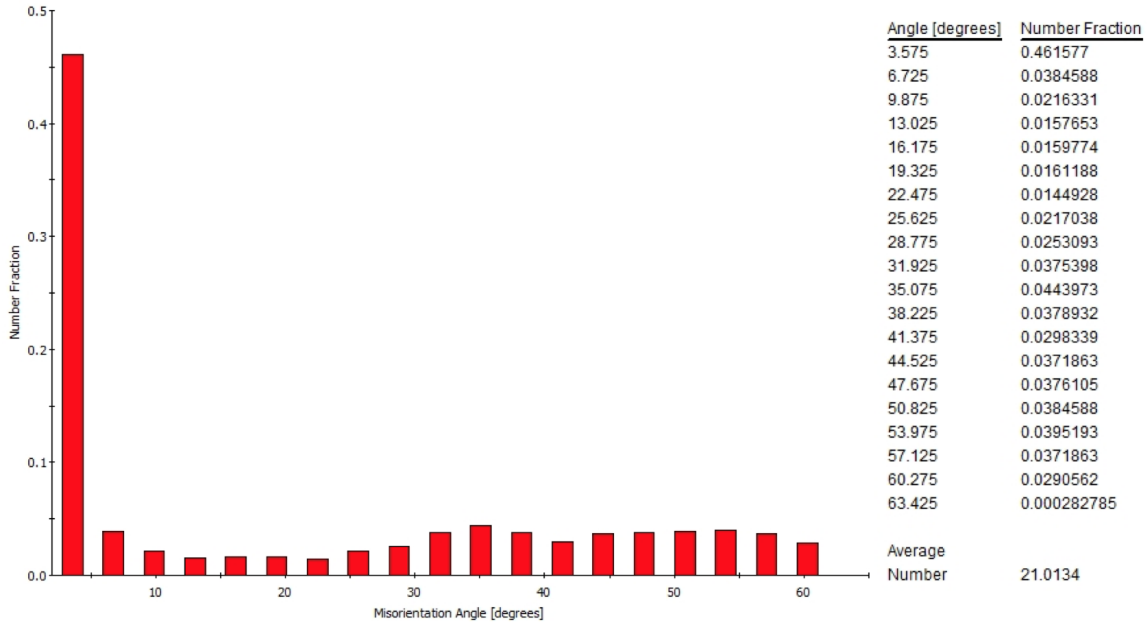

Angle [degrees]	Number Fraction
3.575	0.461577
6.725	0.0384588
9.875	0.0216331
13.025	0.0157653
16.175	0.0159774
19.325	0.0161188
22.475	0.0144928
25.625	0.0217038
28.775	0.0253093
31.925	0.0375398
35.075	0.0443973
38.225	0.0378932
41.375	0.0298339
44.525	0.0371863
47.675	0.0376105
50.825	0.0384588
53.975	0.0395193
57.125	0.0371863
60.275	0.0290562
63.425	0.000282785
Average Number	21.0134

(d) 10% post-stretched.

Figure E.1: Grain boundary misorientation histograms of T6 tempered 6005.40 acquired during electron backscatter diffraction in scanning electron microscope.

Appendix F

Pole figures of 6005.40

In Figure F.1 pole figures of T6 tempered 6005.40 are presented. Pole figure of the undeformed, 10% pre-rolled, 10% post-rolled and 10% post-stretched sample is displayed in Figure F.1a to F.1d, respectively.

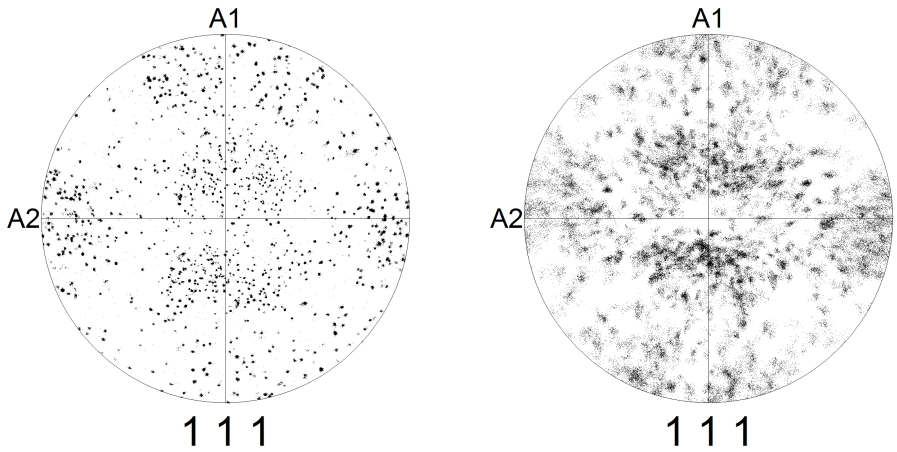

(a) Undeformed. **(b)** 10% pre-rolled.

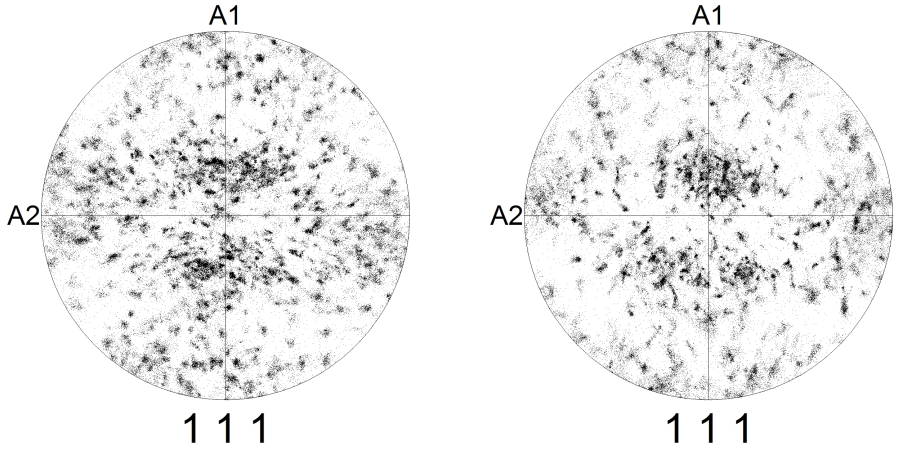

(c) 10% post-rolled. **(d)** 10% post-stretched.

Figure F.1: Pole figures of T6 tempered 6005.40 acquired during electron backscatter diffraction in scanning electron microscope.